Machine Learning-Assisted Design of Metasurface Radomes

BY

YI-HUAN CHEN

B.S., National Taiwan University, Taipei, Taiwan, 2010

M.S., National Taiwan University, Taipei, Taiwan, 2012

THESIS

Submitted as partial fulfillment of the requirements
for the degree of Doctor of Philosophy in Electrical and Computer Engineering
in the Graduate College of the
University of Illinois Chicago, 2023

Chicago, Illinois

Defense Committee:

Pai-Yen Chen, Chair and Advisor
Danilo Erricolo
Besma Smida
Zizwe Chase
Jie Xu, Mechanical and Industrial Engineering

ACKNOWLEDGMENTS

I would like to express my sincere gratitude and appreciation to everyone who played a role in my PhD journey and helped to make this dream achievable.

First, I would like to sincerely thank my PhD advisor, Dr. Pai-Yen Chen. His scholarly guidance was indispensable. Thanks for the encouragement, trust, and support, especially when the path of my PhD program grew dark. I will always appreciate the opportunities and new research challenges Dr. Chen helped me to discover. You are the type of mentor that I will strive to be in the future.

I would like to express my sincere gratitude to my beloved Mom and Dad, who have sacrificed so much so that I can achieve my dreams. I am so proud to be your son and I will always do my best to honor you. Thanks for believing in me. Both of you are the best role models imaginable. I would like to thank my sister Yi-Chen Chen. Her support has given me so much strength. I would like to dedicate my PhD to all my family members in my home country. I will never forget their endless love, kindness, and warm hospitality.

I would like to dedicate this PhD to my best friends, Tim, Jeff, and Henry, for all of their help and support, especially during the times that I felt so overwhelmed. Thanks for everything, including teaching me to play the badminton ball. I would also like to sincerely thank all the members I met in the badminton club. Their assistance made me adjust my life in Chicago quickly.

I would also like to dedicate this PhD to my manager, Victor Lu, in my internship period. I really appreciate his effort for improving my programming skill. I would also like to sincerely thank to all the colleague I met in the internship company. Their kindness helps me face the challenge and complete the project of the intern topic.

ACKNOWLEDGMENTS (Continued)

Finally, I would like to take this moment to thank my beloved, Ting-Yi Wu, for being with me through the good and bad times. Without her, I would never be able to insist until the last step of my PhD journey. There are no words that can express my gratitude. This PhD is as much hers as it is mine!

YC

CONTRIBUTION OF AUTHORS

Chapter 1 introduces the background and states the motivation of the purpose of this thesis. Chapter 2 presents a detailed explanation of the concepts and theories relative to the topic of this thesis. Chapter 3 represents a published manuscript as Lee, J.Y., Chen, YH. & Chen, PY. Degeneracy of light scattering and absorption by a single nanowire. Sci Rep 11, 18657 (2021) for which I was one of the primary authors. My contribution is mainly on the numerical simulations and the schematic diagrams. Chapter 4 and Chapter 5 represent my own unpublished result which are corresponding to the main motivation of this thesis. The work in Chapter 5 comes with the idea of the previous work of a lab member, Zhu, Liang, and represents a further study of the topic. Fig. **5-1** comes from Liang's previous work published as L. Zhu and P. -Y. Chen, "A Low-RCS and Low-ECC Transparent Meta-Radomes Based on a Conductive Nanocomposite," 2021 IEEE International Symposium on Antennas and Propagation and USNC-URSI Radio Science Meeting (APS/URSI), 2021, pp. 1859-1860, doi: 10.1109/APS/URSI47566.2021.9703729 of which directly and clearly states the problem. A brief summary is presented in the last page of each chapter. In addition, a conclusion and potential future works are mentioned in Chapter 6.

TABLE OF CONTENTS

TABLE OF CONTENTS (Continued)

CHAPTER **PAGE**

LIST OF TABLES

LIST OF FIGURES

LIST OF FIGURES (Continued)

FIGURE **PAGE**

LIST OF FIGURES (Continued)

FIGURE **PAGE**

LIST OF FIGURES (Continued)

FIGURE **PAGE**

LIST OF FIGURES (Continued)

FIGURE **PAGE**

LIST OF FIGURES (Continued)

FIGURE **PAGE**

LIST OF FIGURES (Continued)

LIST OF ABBREVIATIONS

5G	The Fifth-Generation communication protocol
UAV	Unmanned Aerial Vehicle
ML	Machine Learning
NN	Neural Network
CNN	Convolutional Neural Network
GAN	Generative Adversarial Network
AED	Auto Encoder Decoder
NLP	Natural Language Processing
Wi-Fi	Wireless Fidelity
LTE	Long Term Evolution
RF	Radio Frequency
NFC	Near Field Communication
MIMO	Multiple-Input and Multiple-Output
PCA	Principle Component Analysis

LIST OF ABBREVIATIONS (Continued)

SVM	Support Vector Machine
EM	Electromagnetism
FDTD	Finite-Difference Time-Domain
FEM	Finite Element Method
RCS	Radar Cross Section
IoTs	Internet of Things
FPC	Fabry-Perot Cavity
CP	Circular Polarization
PRS	Partially Reflecting Surface
STC	Space Time Coding
ECC	Envelop Correlation Coefficient
NF-FFT	Near-Field Far-Field Transformation
TE / TM	Transverse Electrical / Magnetic fields
PML	Perfect Matched Layer

LIST OF ABBREVIATIONS (Continued)

SBC	Scattering Boundary Condition
KNN	K-Nearest Neighbor
DNN	Deep Neural Network
RNN	Recurrent Neural Network
FEA	Finite Element Analysis
ANN	Artificial Neural Network
ResNet	Residual Network
mm-Wave	Millimeter Wave
GA	Genesis Algorithm
PSO	Particle Swarm Optimization
GbSA	Galaxy-based Search Algorithm
SRR	Split Ring Resonator
DoF	Degree of Freedom

SUMMARY

Antennas are indispensable to wireless communications. With high frequency band signals applying in 5G channels, the wireless transmission rate is significantly boosted. While 5G technologies are expected to be the foundation for the next generation's communication systems, the high frequency band leads 5G antennas be very sensitive to the environment. To set up the base stations efficiently, the demand for a fast and accurate measurement method of antenna radiation patterns is urgently needed. In addition, the development of multi-input-multi-output (MIMO) antenna systems also plays an essential role in 5G technologies. However, the mutual coupling effect significantly affects the performance of MIMO antenna systems which not only degrades the data diversity but also reduce the antenna gain.

This dissertation presents two machine learning-assisted applications in electromagnetics (EM) and antenna areas. The first model represents a neural network architecture that enable rapid and accurate retrieval of the three-dimensional (3-D) radiation pattern and radar cross-section (RCS) from the sparse measurement data. The proposed algorithm based on generative adversarial network (GAN), can rapidly and accurately retrieve the three-dimensional (3-D) radiation pattern and radar cross-section (RCS) from the sparse measurement data. The sparse antenna radiation patterns are randomly collected and pre-processed as space correlated two-dimensional arrays. The GAN model attempts to recover the entire radiation pattern in the angular space. The result shows the proposed GAN model can measure the 3-D radiation pattern of an antenna without tediously measuring the radiated power at all directions, thereby leading to a significant reduction of measurement time when compared to direction far-field measurements and near-field, spherical-scanning.

The second part of this thesis studies a machine learning-assisted inverse design for antenna radomes with broadband, wide-angle unidirectional or bidirectional absorption, aiming to reduce mutual coupling in multi-input-multi-output (MIMO) antenna arrays. MIMO antennas usually align in a limited space with narrow gaps between each other, resulting in high correlation and strong mutual coupling effects that reduce the antenna gain and increase the data transmission error. One of the solutions is to cover the antenna array with a radome that can mediate the electromagnetic mutual coupling between antennas. The proposed ML algorithm can automatically synthesize the metasurface radome to tailor reflection, transmission, and absorption of EM waves in a unidirectional or bidirectional manner. The metasurface is composed of a transparent conducting sheet and assembled by the pixel-based bricks. The data for training is generated by random numerical simulations. The inverse design model is then trained by the dataset loaded with EM information including reflection and transmission spectra and polarization dependencies, so as to produce the optimum metasurface geometry for the specific application. A set of metasurface configurations are inserted back to the numerical simulator to validate the performance of the ML-assisted design tool. Several constraints are made to limit the searching space. Three representative metasurface design examples, including an ultrathin, bidirectional metasurface-absorber (which exhibits high absorption in the entire X-band, and a wide-angle unidirectional metasurface-absorber, are presented to validate the the proposed ML-assisted design model.

1. INTRODUCTION

1.1. Motivation

Antennas are indispensable to wireless communications. From televisions to mobile phones, people receive information propagating using different type of antennas in their daily life. Recently, products using 5^{th} generation technology standard (5G) have been well-developed [1]–[9]. With high frequency band signals, the wireless transmission rate rapidly speeds up. While 5G are expected as the foundation of the next generation's technologies, there are several drawbacks needed to be improved [10], [11]. One of the most serious problems is the coverage rate. In exchange for the high speed, 5G signals are very sensitive to the environment due to the high frequency band, so that the coverage area of a 5G antenna is much smaller comparing to the antennas in previous generation. In order to make the coverage area as wide as possible in noisy environment, Unmanned Aerial Vehicles (UAVs) are used to measure the antenna radiation pattern and find the best place to set up 5G base stations recently [12]–[15]. The antenna radiation pattern plays an important role for deployment and configuration of antennas and their arrays. However, measuring an antenna's radiation pattern and gain is generally very time-consuming and is limited to specific planes or angles [12], [13]. Hence, it is an urgent task to develop new measurement and characterization techniques that enable fast and accurate evaluation of radiation patterns of antennas placed in realistic environments.

In this thesis, we proposed a series of machine learning (ML)-assisted models, such as the convolutional neural network (CNN), the ResNet, the generative adversarial network (GAN), and the auto-encoder-decoder (AED) architecture, that have a better performance compared to traditional electromagnetic (EM) methods like the numerical simulation. Among the ML architectures we used in this thesis, GAN is a popular neural network (NN) model and has been applied to many applications in computer vision area. GAN can learn how to generate new data with related features of the training set and can be particularly useful for generating images that look authentic to human observers. In the field of the computer vision, it has been proved that GAN has a strong ability to dehaze or recover the blank of images [16]–[18]. In the same vein, GAN may allow one to exploit the limited measurement data to evaluate the detailed radiation pattern with sidelobes and nulls, so that to extremely reduce the measuring time of UAVs. In addition, AED is also a powerful technique in data reconstruction. It can extract the key features from the input and construct the expected output based on these features. AED is not only applied to the applications of computer vision and object detection, but also the applications of natural language processing (NLP) due to its flexibility. As a result, we come with an idea that the ML-assisted models can also be a potential tool for solving EM problems.

Machine learning is so popular that even in the field of electromagnetics, many prior studies have used the techniques such as the inverse design model to substitute the numerical simulation for optimizing the configuration of the design of metamaterials and antennas [1], [2], [5], [19]–[29]. However, based on our literature review, none of prior works applied GAN to radiation pattern measurement as far as we know. We believe that the proposed method will be a great contribution to 5G infrastructure constructions.

1.2. Antenna in 5G Telecom

Antennas enable telecommunications. They can transfer the signals made of electrical current to electromagnetic waves and transmit the waves through the space or receive the radio waves in the opposite way. There are many types of antennas such as wire, loop, helix, horn, and microstrip antennas. Among all the antennas, Yagi-Uda antenna is one of the most popular type of antenna array [3], [7], [29]–[33]. It is composed of series of dipole antennas. All of the dipole antennas except for the last one are called the director and driven element, which receive radio waves with specific frequency from the desired direction and amplify the received energy. The lengthy antenna at the end of the structure is called the reflector, which reduces the signals propagating in its own direction and reflects the energy towards the driven element and director. Therefore, Yagi-Uda antenna is highly directional and wave selective. In early ages, Yagi-Uda antenna is well-known as the television antenna. Due to its high directivity and simplicity of the structure, it can also be made as microstrip antennas and apply to those fashion wireless technologies such as wireless fidelity (Wi-Fi) stations, Bluetooth, and radio frequency (RF) applications [3], [7], [30]–[33].

Recently, in consequence of lacking capacity in 4G frequency bandwidth, the development of 5G mobile networks become more significant. Comparing to 4G long term evolution (LTE) networks, 5G new radio (NR) uses the frequency band from 2.5 GHz to 44 GHz (or from 120 mm to 12.5 mm in wavelength) [10]. It is typically called sub-6 GHz bands for the frequency smaller than 6 GHz, which has been designed for mobile phones, hence the size of the antenna must be significantly reduced. There are several potential challenges for sub-6 GHz band antennas. First, in order to achieve high data transmission rate, massive multiple-input and multiple-output (M-MIMO) technology is required [1], [5], [8], [31], [34], [35]. Besides, not only 5G antennas, 4G LTE, 3G, Bluetooth, Wi-Fi antennas, or even the near field communication (NFC) coil need to be considered due to the compatibility, hence increasing the number of antennas integrated inside the mobile phone. It is critical to arrange these antennas within mobile phones since a few millimeters change would make the performance be very different. Furthermore, since users desire higher performance in 5G smart phones which requires, the size and weight of traditional batteries must be larger to satisfy the growing demand of power consumption [10]. Therefore, the breakthrough of battery technologies and power management becomes more and more important. These challenges restrict the performance of the 5G antenna and is urgently needed to be resolved. On the other hand, for the frequency band above 6 GHz, it is usually called mm-Wave bands. This type of antennas usually has high gain and supports multiple beams and can be designed as chip-integrated arrays due to its small physical size. Therefore, it becomes a solution for M-MIMO and can provide high quality data link in all directions around mobile phones.

The rapid growth of 5G wireless technology has also raised the demand of the base station antenna. With the high gain capabilities, M-MIMO antennas can significantly improve the quality of the connection to end users [34], [35]. However, due to the short wavelength, radio waves in 5G frequency bands attenuate rapidly through the space and are easily to be blocked by obstacles around the environment comparing to waves in 4G and LTE bands [10], [11], [13], [14]. To increase the coverage rate of 5G signals efficiently, optimizing the location of 5G base stations is one of the key challenges as well as increasing the number of the base station. In recent, UAV has been used to measure the antenna radiation pattern and search the optimal place to set up 5G base stations since it can move arbitrarily in 3D space without any confinement [12]–[14]. However, measuring an antenna's radiation pattern and gain is still very time-consuming even using UAVs. Therefore, it is an urgent task to develop new measurement and characterization techniques that enable fast and accurate evaluation of radiation patterns of antennas placed in realistic environments.

1.3. Machine Learning and Neural Network

Machine Learning (ML), the most popular Artificial Intelligence (AI) technology, has been widely used in many fields such as medical science [36]–[38], computer vision [16]–[18], [39], [40], signal processing [41], [42], and communications [43], [44]. It is a study regarding the algorithm that computers can learn things themselves and improve automatically through experience. In general, ML includes three categories: supervised learning, unsupervised learning, and reinforcement learning. In supervised learning, all the targets are known and the computer learns with questions (inputs) and desired answers (outputs). Classification and regression are two typical problems of supervised learning. So far, most of mature ML applications are based on supervised learning. For instance, in medicine, pre-trained AI is used to help doctors diagnose patients [36]. It is also useful in object detection area since the pattern of the object is specified. On the other hand, in unsupervised learning, the answer is unknown or cannot be limited within a range. Comparing to supervised learning, the data set in unsupervised learning area does not have the ground truth, hence the computer must organize itself using special techniques such as principal component analysis (PCA) or clustering. In fact, most of the problems in real life are belong to unsupervised learning area. For instance, the data mining researchers try to discover the association among each data in order to figure out the behavior of customs and improve the efficiency of the recommendation systems [44], [45]. In pattern recognition area, unsupervised learning models are also applied to anomaly detection [46], [47]. Different with the two models above, reinforcement learning trains the computer with reward and punishment mechanism. The computer is rewarded for the correct moves and punished for the incorrect ones. In sum, reinforcement learning is a type of optimization problems. Unlike supervised and unsupervised learning, the reinforcement learning models do not need to be well pre-trained. In contrast, it keeps training when practicing. Self-driving car is one of the most popular reinforcement learning applications recently. The AI collects data around the environment and give the commend to drive the car automatically. Although there are still several issues needed to be resolved, these ML applications, however, will play a crucial role in human society and certainly raise a new industrial revolution in the future.

Among all the ML method, Neural Network (NN) is one of the most popular models recently. In 1986, G. Hinton, et al. [45] proposed back-propagation algorithm, which becomes the main core of NN. Y. LeCun, et al. [48] then developed a NN model to recognize hand-writing numbers based on back-propagation algorithm, which is so-called Convolutional Neural network (CNN) later. As hardware advances, starting from 1993, more and more ML applications are developed in speech processing [49], [50] and pattern recognition [46], [47]. In 2006, G. Hinton, et al. [45] proposed Restricted Boltzmann Machines (RBMs) and Deep Belief Networks (DBNs), and successfully trained the multi-layers network, which becomes the prototype of deep learning. A year later, NVIDIA developed Computer Unified Device Architecture (CUDA). ML developers can calculate deep NN using GPU via CUDA easily, making the computational speed ten times faster than before. In 2010, ImageNet, a large image database for object recognition constructed by F. F. Li [51], began to hold an annual AI competition called ImageNet Large Scale Visual Recognition (ILSVR). Until 2017, Many novel NN algorithms proposed by ILSVR participants, such as AlexNet (2012) [52], GoogleNet (2014) [53], [54], ResNet (2015) [55], and SENet (2017) [56], [57], got outstanding performances and became the prototype of many later works. Comparing to traditional ML methods, such as Markov model or Support Vector Machine (SVM), NN has relatively simple calculation process and model architecture but better performance in most cases, hence is applied to more and more complicated applications such as natural language processing (NLP) [58], [59] or data mining [60], [61].

1.4. Applications of Neural Network models in Electromagnetics

The performance of NN models is so vigorous that the model has been used in many research areas. In the field of electromagnetic (EM), the NN models are constantly being substituted for the simulation models using numerical methods such as finite-difference time-domain (FDTD) and finite element method (FEM) since the numerical simulation models are usually very time-consuming. So far, the EM researchers mainly focus on two topics: the parameter prediction and the inverse design model [9], [10], [13], [19], [54]. Similar as those typical NN applications, the parameter prediction is to evaluate the parameters of the performance of the designed antenna or nanostructure. In these models, the shape of the designed structure is usually fixed. The model is then fed with the tunable configurations of the designed structure and predicts the optical properties, such as the central frequency of the working region, as the output. However, since the prediction is usually inaccurate when the number of the output is more than the number of the input in the NN model, these models are usually used to predict only the properties that can be described with a few parameters such as resonant frequency, antenna gain or directivity. Even though, it is a powerful substitution of numerical simulations especially when in the configuration swipe.

In contrast, the inverse design models are expected to help optimize the configurations of the designed structure based on the desired parameters [62], [63]. Like parameter prediction models, the shape of the designed structure has been decided in the beginning as well. However, the input of the model is now the performance properties while the output becomes the optimal configurations of the designed structures. It can be achieved from training parameter prediction model and then making it upside-down, which is so called the inverse design. The inverse design model can rapidly reduce the time and calculation resource comparing to the model using numerical simulation, since it can only evaluate the parameters from the configuration of the designed structure, hence is inevitable to repeat try-and-error tasks and consume vast time.

Despite many prior works in EM field have used NN models, none of them applied to evaluate the radiation pattern. Therefore, we envision that the proposed technique may be beneficial for practical experimental measurements of antenna radiation patterns, radar cross sections (RCS), wireless channel capacities, as well as various radiation and scattering parameters.

1.5. Research Contributions

The main contributions of this thesis are represented as follows:

1. We proposed a novel ML-assisted model based on conditional-generative adversarial networks (c-GANs) that can assist the measurement of antenna radiation patterns and hence enable a fast and accurate antenna pattern measurement method.

2. We proposed a novel ML-assisted inverse design model based on auto-encoder-decoders (AEDs) that can inversely design metasurfaces composed of pixel-level bricks from the spectra of s-parameters. Moreover, the proposed model can provide the design for multiple applications based on the given purpose.

3. We demonstrated that the proposed ML-assisted inverse design model has the state-of-art potential in the metasurface radome design by presenting three 10×10 design cases for different applications. In addition, the experiments also show that AED performs better than other common neural network structures such as ANN and CNN when applied into the proposed design cases.

1.6. Thesis Outline

The rest of this thesis is organized as follows. In Chapter 2, we provided a detail literature review for the related topics. In chapter 3, we first presented an EM scattering problem under specific constraints which is solved by a complex analytical solution. Then, in chapter 4 and 5, we represented the development of an efficient radiation pattern measurement method and a unique inverse design method for metasurface radomes, respectively, to demonstrate the feasibility of the ML-assisted model applied in EM applications. The conclusion and potential future work are presented in chapter 6.

2. REVIEWS OF RELATED WORKS

This chapter presents a detail literature review of the background knowledge and previous works related to the topic and contribution of this thesis.

2.1. Development of Antennas

Antenna is indispensable to wireless communication nowadays. From old-fashion wireless channels of televisions to the internet of things (IoTs) on smartphones, the demand for high quality antennas grows up quickly. Not only industry, but infrastructures that enable stable and high data rate transmission have also been desired for entertainment applications. In addition, the evolution of antenna size has gradually become smaller due to the demand of higher frequency band.

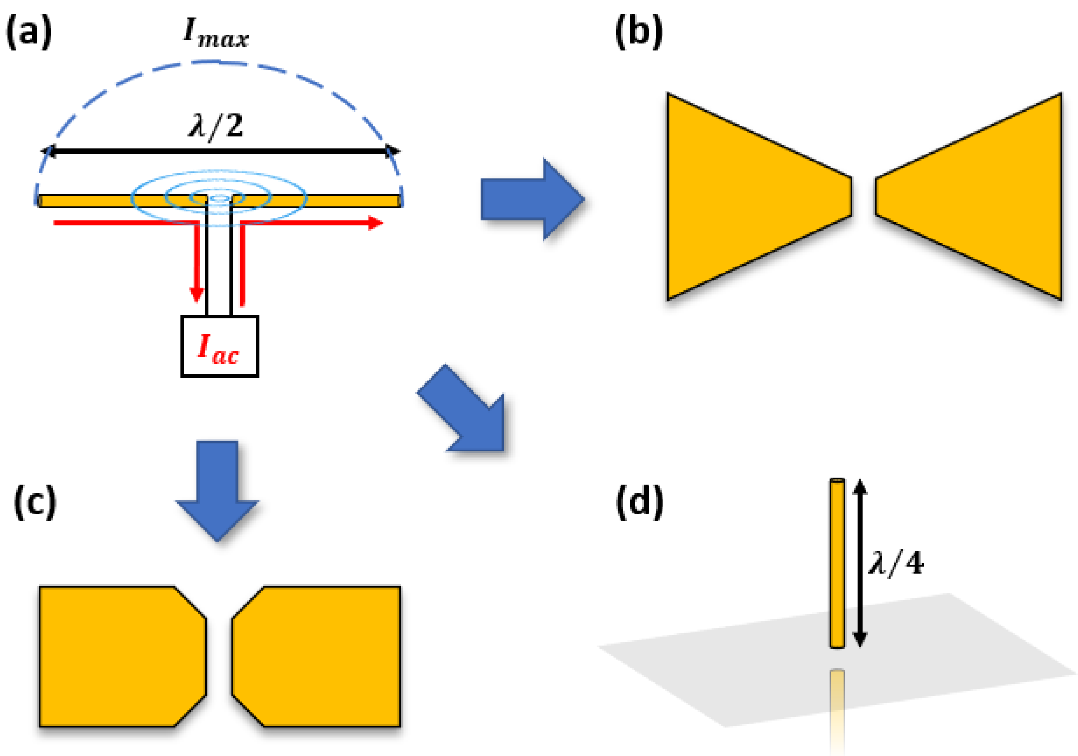

Figure 2-1 The schematic of (a) classical dipole antenna, (b) bow-tie antenna, (c) microstrip antenna, and (d) monopole antenna. The radiation efficiency becomes optimal when the length of dipole antenna equals to half wavelength.

The most classical antenna is probably the dipole antenna [64]–[66]. The schematic of a dipole antenna is presented as Fig. **2-1**. It consists of two equal-length rods made of conductive materials (e.g., copper) arranged with a small gap along the major (lengthy) axis. The high frequency AC current flow is fed from the middle gap and propagated to the edge of each rod. Due to open circuit, the current distributes as a standing wave which vanishes at the end of two sides, result in the radiation wave excited from the gap. In order to achieve the largest excitation, the optimal length of the entire dipole antenna is half of the resonant wavelength since the current distribution will have a maximum at the gap area, hence nearly all of the source power can be transferred to the radiation power. In addition, the input impedance of half-wavelength dipole antennas is approximately $73\,\Omega$ which is a suitable value for source impedance [65]. However, since the radiation wave propagates toward all direction perpendicular to the antenna structure, the directivity and gain of dipole antennas is low comparing to other types of antennas. Therefore, the dipole antenna is usually used as an excitation source of other antennas such as reflector antennas [67], [68] or the driven element of Yagi-Uda antennas [69]–[71].

Despite of the excitation source, there are still several applications of dipole antennas. One of the advantages of the dipole antenna is that the shape can be varied to match the usage and environment and hence can be easily applied for multi-purposes. For instance, Fig. **2-1**(b) shows a deformed dipole antenna called bow-tie antennas. The bow-tie antenna is a dipole antenna with triangle or trapezoid arms, which increases the frequency bandwidth so that it is widely used in ultra-high frequency (UHF) television antennas [72], [73]. The monopole antenna, which is shown in Fig. **2-1**(d), is another kind of dipole antennas which consists of one physical arm and an imaginary arm reflected by the ground plane based on the method of images [74]. Comparing to the ordinary dipole antenna, the monopole antenna has half input impedance but double gain and directivity since the wave radiated toward only upper hemisphere, hence it is suitable to be used in an inner space, such as Wi-Fi routers. Moreover, in modern age, the microstrip antenna shown in Fig. **2-1**(c) becomes popular due to the small size and thickness [64]. Developed from classical dipole antennas, the shape of the microstrip antenna changes from rods to thin planes, so that it can be placed in a small area, such as smart phone or even 5G MIMO antenna stations, which may contain only a few millimeters.

Except for dipole antennas, most of the antenna are usually highly directional so that the radiation wave can propagate far away with even feeding power. In late twentieth century, the Yagi-Uda antenna was widely used for public to receive the signal of television channels [75]. Invented by Shintaro Uda and Hidetsugu Yagi in 1926, the Yagi-Uda antenna consists of three parts: the director, the driven element, and the reflector, as shown in Fig. **2-2**(a). The director guides the radiation wave excited by the driven element toward the direction along the antenna's major axis. The reflector is placed in the rare to reflect the radiation wave propagating backward out of phase, so that all the excitation power can be concentrated on the forward direction, hence enable a high gain, high directivity propagation. The reflector antenna is another type of high directivity antennas [67], [68]. Similar as Yagi-Uda antennas, the reflector antenna is usually composed of an excitation source and one or more reflector(s), as shown in Fig. **2-2**(b). The excitation source is placed at the focal point of the reflector. The reflector reflects the radiation wave excited by the feeding source. According to the geometrical optics, the wave will defocus and become a plane wave and hence it enables the long-term signal propagation. As a result, the reflector antenna is widely used in radar, satellite communications, remote sensing, and astronomy searching.

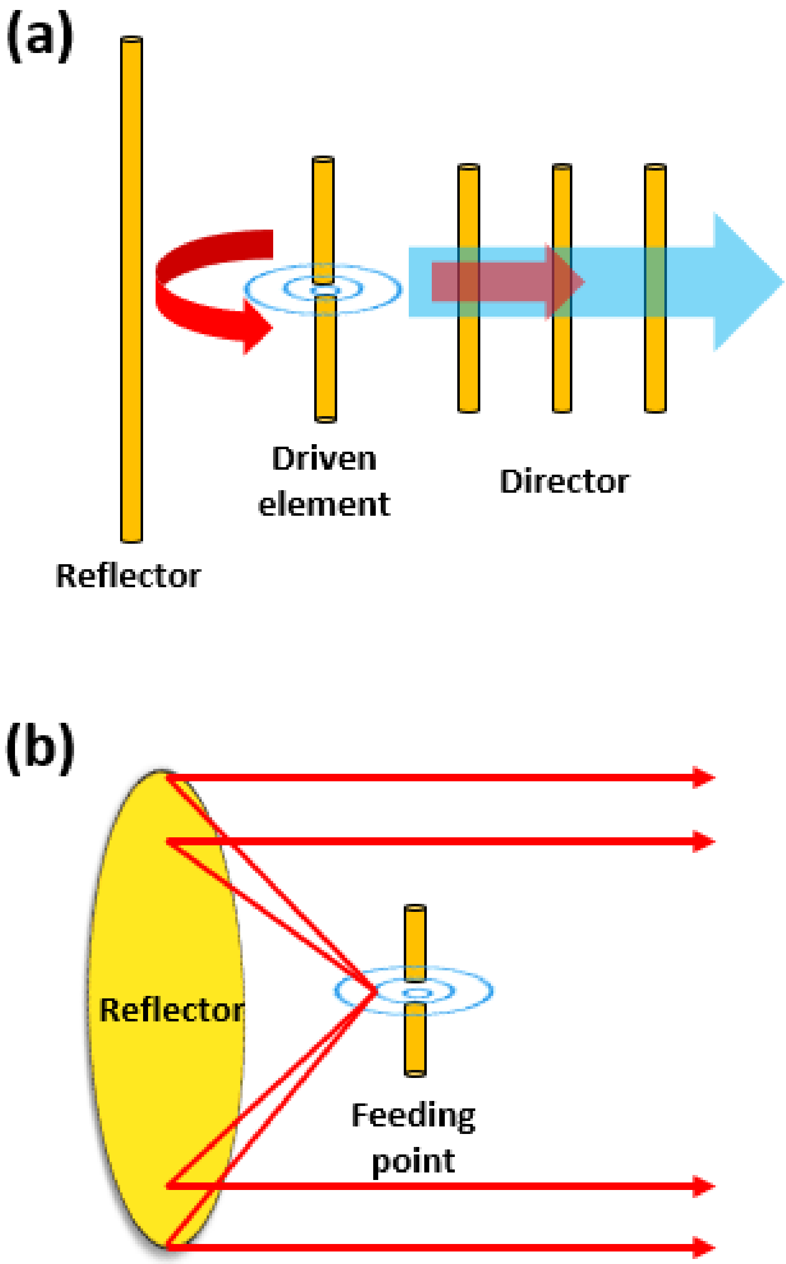

Figure 2-2 The schematic of high-directional antenna: (a) Yagi-Uda antenna and (b) reflector antenna. It is noticed that the reflector of the reflector antenna can be varied.

There are many kinds of reflectors, such as parabolic, hyperbolic, plane, or corner reflectors. The most popular shape is parabolic which is widely used in radio astronomy and telecommunication areas.

Horn antennas are also a common type of high gain and high direction antennas that are widely used as an efficient antenna measurement tool or a feeding source for

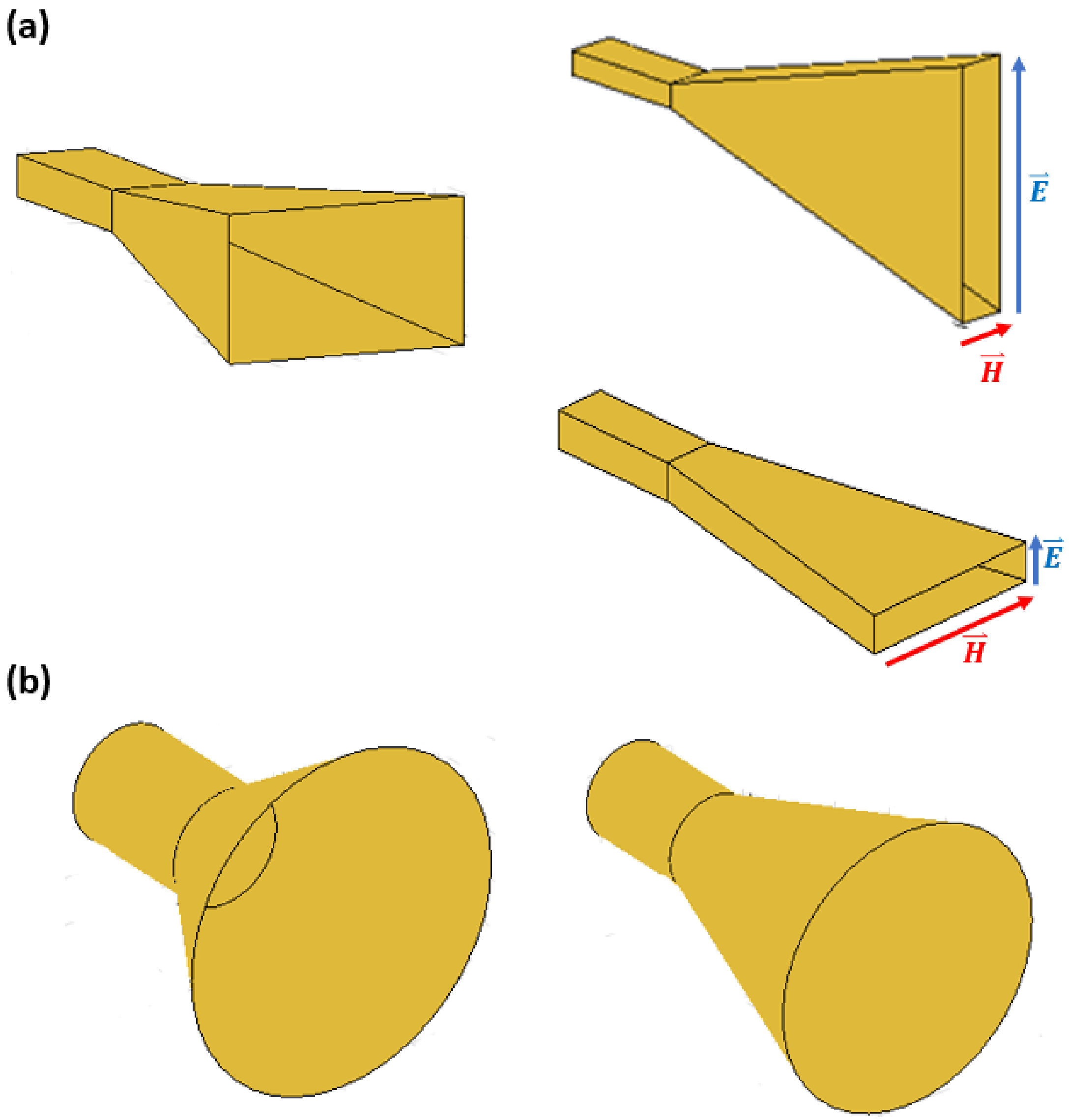

Figure 2-3 The schematic of different types of the horn antenna: (a) Pyramidal horn antenna (left) and two special types - E-plane (upper-right) and H-plane (bottom-right) sectoral antennas. (b) Conical antennas with different feeding length.

large antennas [76]–[78]. The horn antenna has a horn connected to a waveguide. The horn is used to compensate the impedance difference between the waveguide and the propagation media (i.e., air) and emit the electromagnetic wave from the waveguide toward the forward direction [78]. The beamwidth of an idea horn antenna with impedance match is usually narrow since nearly all the radio waves propagate along the major axis without dissipation, result in high directivity. In addition, since there is little loss from the waveguide to the horn, the gain of the horn antenna is nearly equal to the directivity. Therefore, it is also a suitable baseline for the measurement of s-parameters and radiation patterns in the anechoic room [79], [80]. Furthermore, the horn can have different shapes and flare angles to match different waveguides and polarizations. As represent in Fig. **2-3**(a), pyramidal horns [79], [80] are used to connect with rectangular waveguides and radiate linear polarization waves. With controlling different flare angles of each direction, the beamwidth can be moderated. Sectoral horns [81]–[83] are the special case of pyramidal horns. The shape is also rectangular which has flare edge along only one direction and a parallel edge pair on the other direction. This horn antenna is used to focus on the specific polarization, such as the E-plane horn (the horn flared along the direction of the electrical field) and the H-plane horn (the horn flared along the direction of the magnetic field), which the schematics are shown in the right side of Fig. **2-3**(a). Conical horns [84] and exponential horns [85] are used to fit the cylinder waveguide. The shape of the two horns is as a cone with the circular cross section, as shown in Fig. **2-3**(b).

Recently, as the operating frequency gradually move to gigahertz, which drops the wavelength from millimeter to even hundred micrometers. Hence, the size of antennas must be decreased to the same scale as the wavelength, too. Traditional high gain antennas such as horn antennas may not be suitable under this scale due to the fabrication limit of the materials and geometry. In addition, the gain becomes much weaker due to the small source power. To solve this issue, the Fabry-Perot Cavity (FPC) antenna is a simple but efficient option since it can be fabricated under micrometer scale and achieve high gain and high directivity radiation, which enable the applications requiring long-range wireless communications [86]–[88]. The FPC

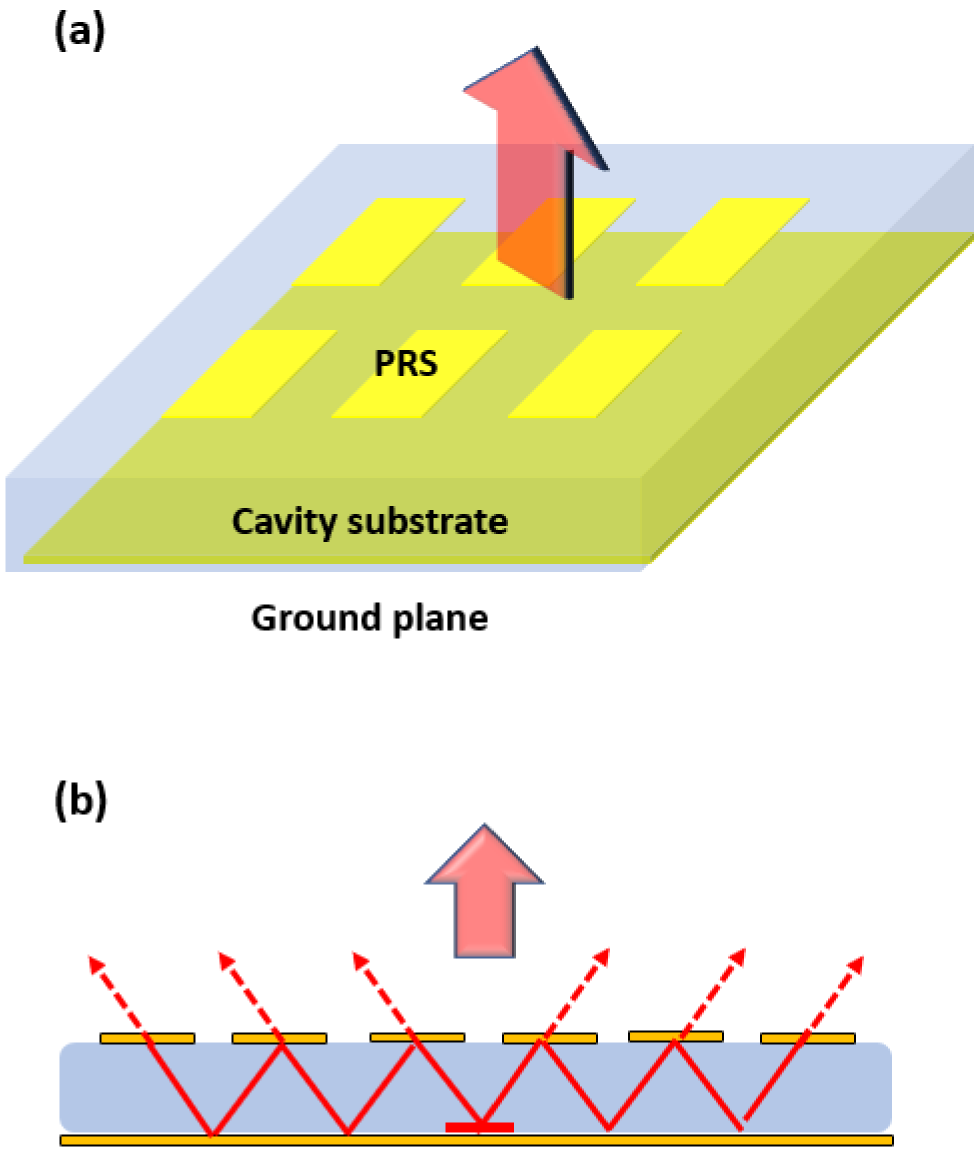

Figure 2-4 (a) The schematic of FPC antenna. The PRS and ground plane are made of conductive materials like metals. The Cavity is usually filled with dielectric substrate. (b) The schematic of how the FPC antenna functions.

antenna consists of a partially reflective surface (PRS) and a metal ground on the top and bottom surface respectively to form a resonant cavity, as shown in Fig. **2-4**. A source antenna feeds a radio wave to the cavity. The wave propagates back and forth insider the cavity, and eventually emits a signal generated by the superposition of all in-phase radiation waves reflected inside the cavity toward PRS's direction, resulting in high gain and high directivity [86]. Due to the cavity structure, FPC antennas is not a suitable option for millimeter wave (mmWave) application. The size and weight of the cavity must be large compared to horn antennas or Yagi-Uda antennas. However, when in the frequency band of 5G communication, the cavity structure becomes a valuable advantage since it can induce high gain radio waves by Fabry-Perot resonant while is easy to be fabricated.

Nowadays, bunches of advantage technologies, such as internet of things (IoTs) [89], autonomous driving [90], healthcare and medical applications [91], or smart home technologies [92], required tremendous data transmission simultaneously in the city. As a result, the growing demand for high data transmission rate and broad channel bandwidth has become an essential topic in modern wireless communication systems [92]. The development of the multi-input and multi-output (MIMO) antenna array becomes an extremely popular topic recently since it can achieve high capacities and high-speed wireless communication at the same time. Unlike the single-input and single-output (SISO) antenna system (as shown in Fig. **2-5**(a)) that the transmitter and the receiver are one to one, the MIMO antenna consists of multiple antennas that can transmit or receive the same data simultaneously, as Fig. **2-5**(b) shows. Several techniques can be achieved by MIMO antenna systems. The first one is called spatial multiplexing [93]. The data is split to multiple parts and sent to the corresponding antenna elements in the receiver. The receiver reconstructs the data based on the information collected by each antenna element. Therefore, the data transmission rate sharply increases since it only takes $1/n$ the time to download the entire data where n is the number of the antennas in the MIMO array. The second technique is related to the diversity [94], [95]. When transferring the data through the environment, the signal may be corrupted by noises or obstacles. The MIMO antenna array can "observe"

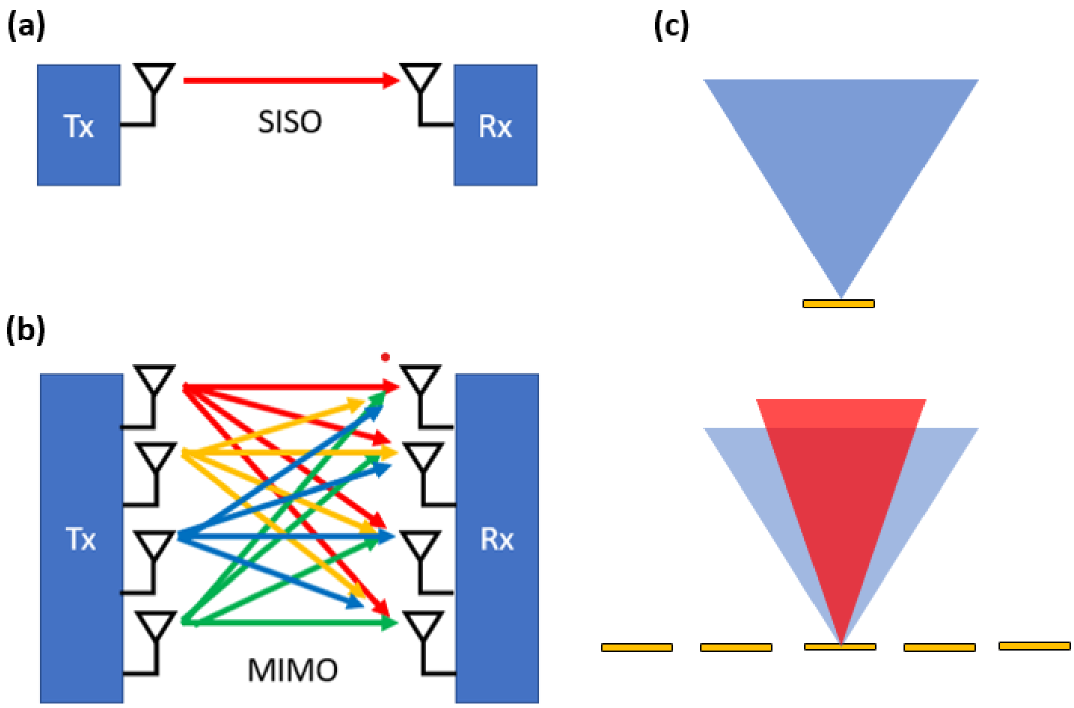

Figure 2-5 The schematic of (a) SISO antenna, (b) MIMO antenna, and (c) the beamforming technique, the blue and red cone present the beamwidth of the radiation waves excited by single antenna and an antenna array, respectively.

the same data in different views of its antenna elements. By comparing and combining the signals from each element, the data can be well reconstructed without losing the information. It is noticed that the corruption issue can also be solved by using signal processing coding methods such as space time coding (STC) [96]. However, the MIMO system can achieve the diversity and multiplexing at once, which is outperformed comparing to traditional signal processing and communication encoding techniques. Furthermore, since the MIMO antenna system is an antenna array, the beam will be more concentrated on the major direction than that from a single unit cell, as shown in Fig. **2-5**(c), which is so called the beamforming technique [96]. As a result, the MIMO system is undoubtedly a core technology for the revolution of next generation communications.

2.2. Antenna Characteristics

It is required to validate the performance of an antenna before implementing it to a wireless system. Therefore, the antenna under test (AUT) is used to measure the characteristics of the antenna. Common characteristics are listed as follows:

1. Radiation pattern

The radiation pattern shows the function of an antenna. It represents the distribution of the intensity emitted from or received by the antenna in the entire angular space. The radiation pattern of a functional antenna usually consists of a main lobe with the largest intensity and several side lobes. The main lobe presents how the antenna operates (e.g., directivity, bandwidth, gain, etc.). For instance, the radiation pattern of a high directional antenna, such as horn or Yagi-Uda antennas, would have a narrow main lobe with the largest intensity along the operation direction, while

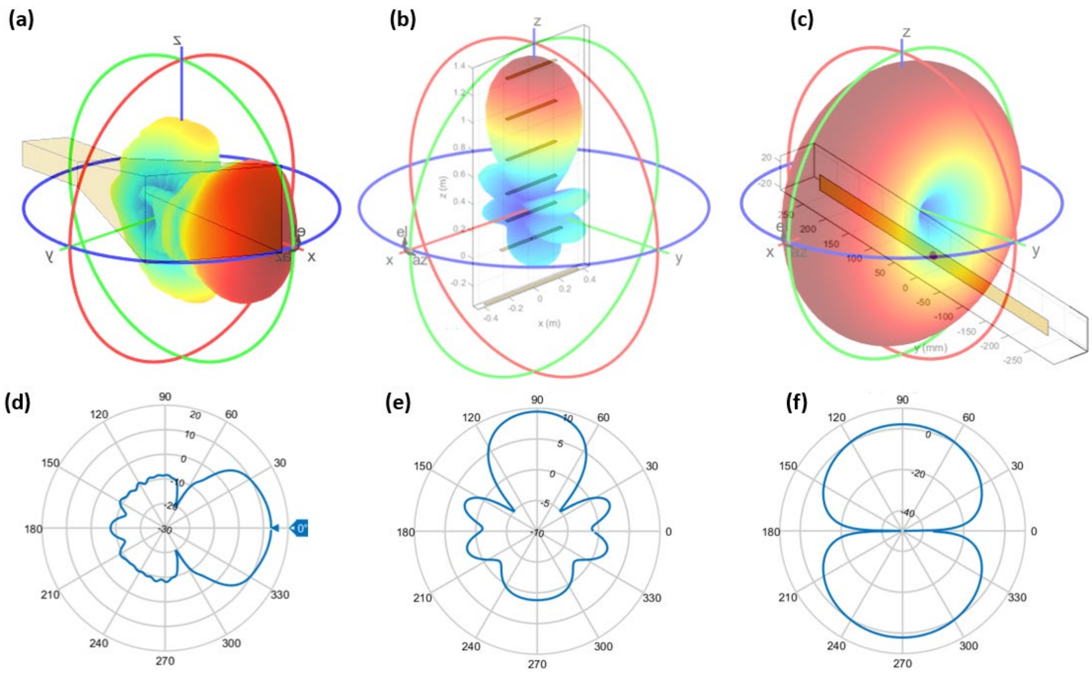

Figure 2-6 Examples of antenna radiation patterns. (a)(b)(c) show the 3-D radiation pattern plot, while (d)(e)(f) show the 2-D radiation patterns. The type of antennas are: (a)(d) Horn antenna, (b)(e) Yagi-Uda antenna, and (c)(f) Dipole antenna, respectively.

several side lobes with relatively small intensity toward other directions in the angular space, as the example shown in Fig. **2-6**(a)(b)(d)(e). On the other hand, for a wide band antenna, such as dipole antennas, the main lobe will occupy wide angle, so that the radiation pattern looks like an apple, as shown in Fig. **2-6**(c)(f). The intensity is usually smaller than high directional antennas due to the distraction, hence it is mainly used to as a feeding source for those high directional antennas.

2. Polarization

Polarization is one of the essential characteristics of antennas that cannot be seen in the radiation pattern plot. It represents the orientation of the oscillation of the radiation waves. An antenna with the polarization along one direction cannot receive the radiation wave with the linear polarization orthogonal to the original polarization. Hence, it is important to make the polarization of both the transmitter and the receiver antennas consistent. On the other hand, the polarization can also be a kind of filters for channel selection. For an antenna array, each antenna can receive their corresponding signal independently if they have independent polarization. This can be done from the design of the antenna or by rearranging the antennas in the array.

In general, there are two types of polarizations for most of antennas: Linear and circular polarizations. A radio wave with the electrical field oscillating along a fixed direction is called the linear polarization wave. In the same vein, an antenna that can transmit or receive the signals with linear polarization is called the linear polarization antenna. For antennas, the linear polarization is defined as vertical or horizontal polarized if the electric field is vertical or parallel to the ground. For instance, the antenna for AM radio broadcast channels is vertical polarized. On the other hand, the antenna for television channels (e.g., Yagi-Uda antennas) is horizontal polarized.

The second type is called circular polarization. It is the polarization when the polarized direction rotates with time. The circular polarization is a special case of elliptical polarizations with constant magnitude of the oscillation. It is called right-hand circular polarization (RHCP) if the rotation is clockwise looking in the direction of propagation and left-hand circular polarization (LHCP) if the rotation is counterclockwise. An advantage of circular polarized antennas is the stability of propagation. For instance, when communicating with an orbital satellite from the earth surface. The relative position and the rotation of the satellite will seriously affect the receiver with linear polarized antennas. However, if the antenna is circular polarized, the propagation will be independent to the angle. In the same vein, the circular polarized antenna can receive signals stably even on the moving object. Therefore, it becomes popular in wireless communications nowadays.

3. Directivity and Gain

The directivity of an antenna is defined as the ratio of the maximum power density to the average power density over the observed surface (i.e., the sphere in the far field). The directivity is always larger than one or equal to one if the maximum power density is equal to the average power density, which implies that the radiation wave propagates to all over the direction averagely and hence the antenna is non-directional. Large directivity implies that the radiation wave of the antenna is highly directional.

The gain is defined as the ratio of input and output power of the antenna. For a transmitting antenna, the gain describes how efficient the antenna converts the source power to the radiation wave toward a specific direction. On the other hand, for a receiving antenna, the gain represents how efficient the antenna can convert the radio wave incident from a specific direction to the electrical signal. In other words, the gain can be seen as the peak on the radiation pattern plot. We usually only consider the gain of the main lobe when measuring the radiation pattern of an antenna since it directly refers to the efficiency of the antenna.

It is noticed that for an antenna, the gain is related to the directivity as:

$$G = \eta D$$

where G is the gain, D is the directivity, and η is the antenna efficiency factor, respectively. For a lossless antenna, $\eta = 1$ and the power is fully converted between the electrical signal and the radio wave. In practice, η is always smaller than 1 due to the loss induced by unperfect impedance match or energy dissipation during the transmission.

4. Beamwidth

The beamwidth of an antenna describes how wide the main lobe is. It is usually represented as the angle between the specific points on the two sides of the main lobe. When measuring the radiation pattern of an antenna, the beamwidth usually refers to

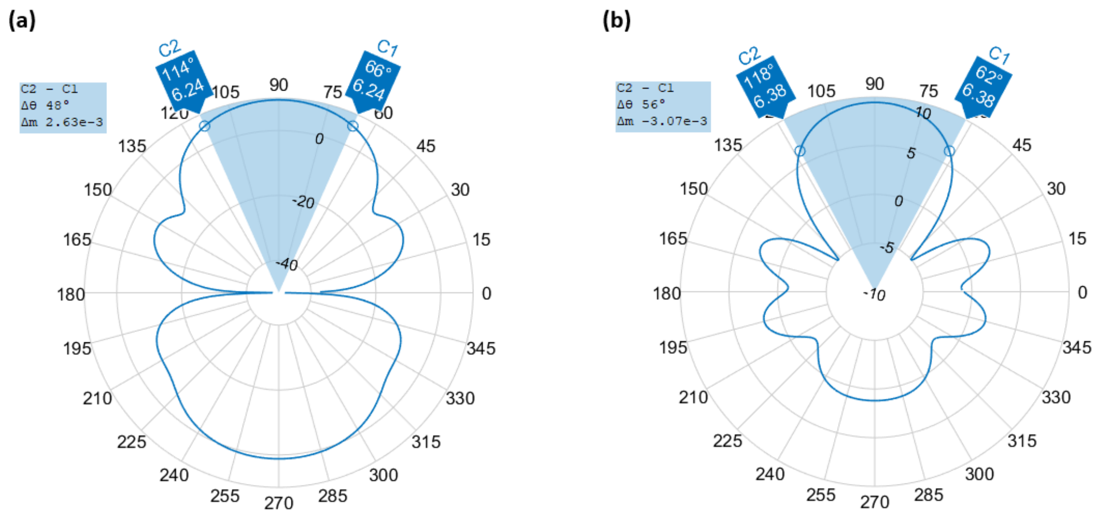

Figure 2-7 The HPBW for the radiation pattern of the Yagi-Uda antenna mentioned in Fig. **2-6**(b) on (a) E-plane and (b) H-plane.

the half power beam width (HPBW). HPBW is an angle between the half power ($-3\ \mathrm{dB}$) points on the two sides of the main lobe. An example of the HPBW for the radiation pattern of the Yagi-Uda antenna mentioned in Fig. **2-6**(b) is presented in Fig. **2-7**. The beamwidth is usually evaluated on 2-D radiation patterns due to the convenience and visualization. As shown in Fig. **2-7**, the HPBW is measurement on the radiation pattern on E-plane (i.e., the azimuth angle is equal to 0^o) and H-plane (i.e., the azimuth angle is equal to 90^o). Except for HPBW, the first null beam width (FNBW) is also a common parameter of the beamwidth. Unlike HPBW, the FNBW uses the null points ($0\ \mathrm{dB}$) as the reference points. It presents the actual angular separation of the main lobe. In general, narrower beamwidth implies higher directivity and higher gain, since more power is converted to the radiation wave toward a particular direction. In addition, the signal to noise ratio (SNR) also increases when the beamwidth decreases.

5. Others

There are still several important factors which can present the performance of an antenna which are not shown in the radiation pattern plot. For instance, the input impedance is defined as the ratio of the voltage to the current from the input source according to Ohm's law. The radiation impedance and the loss impedance present the efficiency of the input power converted to the radiation wave and the heat, respectively.

The operating frequency and the frequency bandwidth also play an important role in antenna measurement. They represent the center frequency and the frequency band of where the antenna operates. When measuring an antenna, it is required to pick a suitable baseline antenna that has the operating frequency band the same or wider than the antenna needed to be measured. Numerical simulation software is a convenient tool to validate the design operating frequency band before the real measurement. The simulation enables the broad frequency band scan of an object structure and evaluates the configures such as s-parameters, electric and magnetic field distribution, surface charges and current flows, or radiation patterns within a short time compared to the measurement process.

2.3. Antenna Measurement Methods

The measurement of an antenna is usually in the anechoic room. The anechoic room is a chamber covered with broad band, high absorption materials. The radio waves will be absorbed when propagating to the edges of the chamber, so that the measuring environment can be considered as an infinite open space without any scattering or reflection waves. A schematic of the general measurement setup in the anechoic room is represented in Fig **2-8**. Typically, the measurement setup consists of

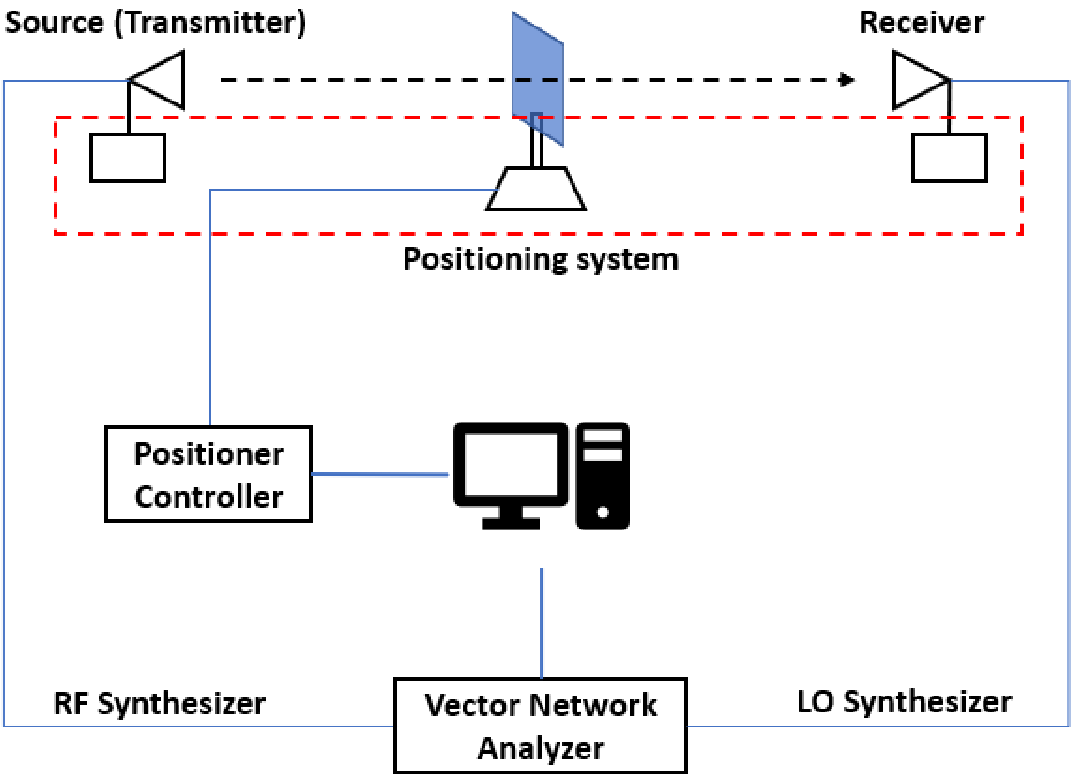

Figure 2-8 The schematic of the antenna measurement setup.

two or more reference antennas as the source (transmitter) and the receiver system. In addition, several stages or racks compose of a positioning system which is used to fasten or rotate the object. The reference antenna is the antenna which has high gain, high directivity, and wide and steady frequency band when tuning the operating frequency for measurement in order to offer a baseline of the measurement process. For instance, the horn antenna is one of the common reference antennas. The source and received signals are controlled by an analysis device such as vector network analyzers (VNA) or spectrum analyzers (SA). The analyzer is used to analyze the received signal and measure the characteristics, such as the impedance, s-parameters, and the radiation pattern, of the object.

For s-parameters measurement, two reference antennas are placed in the corresponding position and toward the object as the source and receiver, respectively. When measuring the reflection (S_{11}), the two reference antennas are placed next to each other with a slight tile angle toward the object. The object is fastened by the stage or rack on the positioner. The receiver receives the radio wave emitted by the transmitter and reflected by the object. Therefore, the tilt angle of the two reference antennas is essential to get the accurate measurement result. In addition, the interference from each other also raises the difficulty of the reflection measurement. On the other hand, when measuring the transmission (S_{21}), the reference antennas are placed on the two sides of the object. The receiver receives the radio wave emitted by the source antenna on the other side and transmitting to the object. Comparing to the reflection measurement, the transmission measurement is simpler to set up since there is no tilt angle or near field interference between the two reference antennas. A schematic describing the s-parameters measurement is presented in Fig. **2-9**.

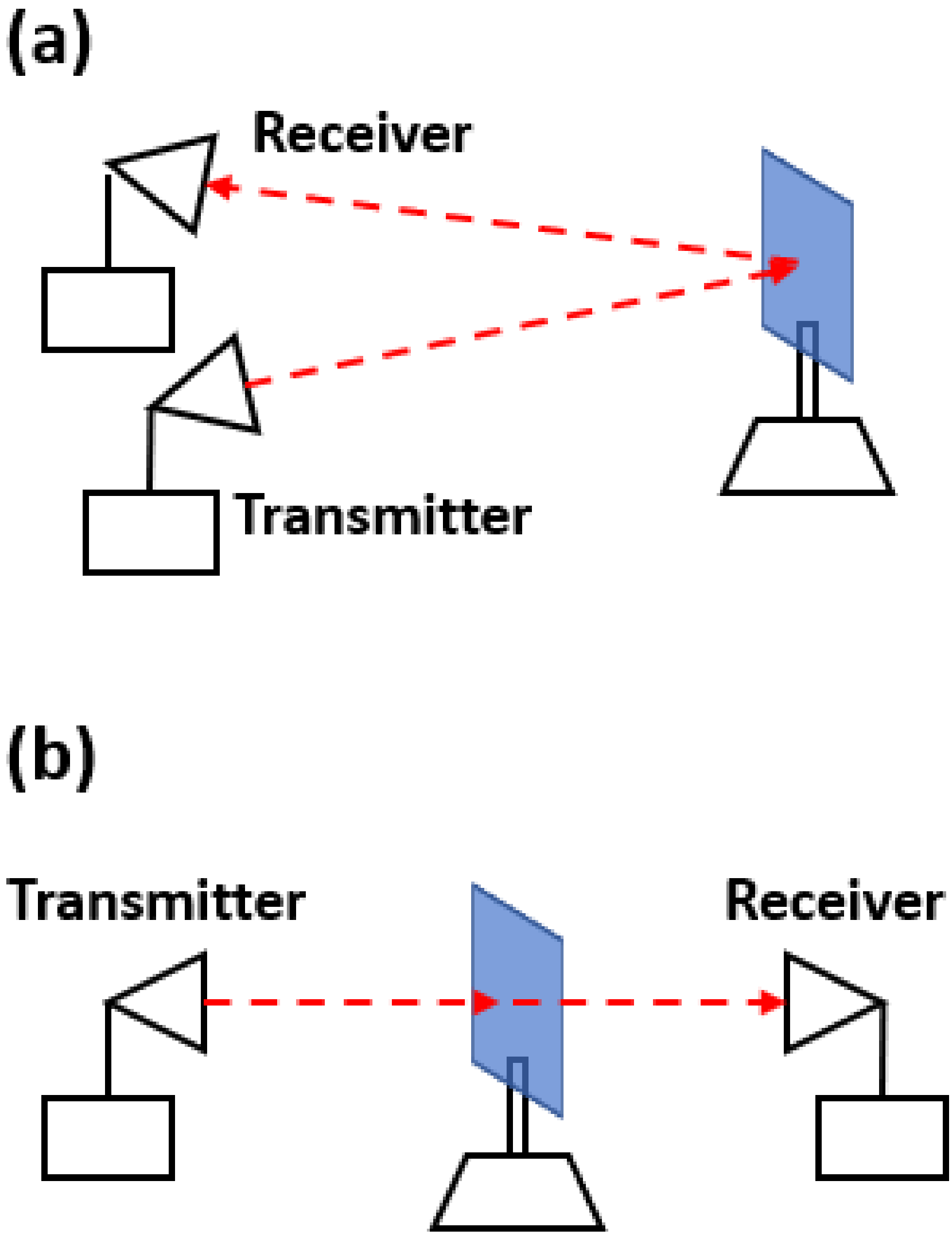

Figure 2-9 The schematic of the measurement setup of (a) the reflection rate (S_{11}) and (b) the transmission rate (S_{21}).

When measuring the radiation pattern of an antenna or radar cross section (RCS) of an object, the target antenna or the object is fasten on the positioner which enable the rotation along both azimuth and elevation angle, hence the measurement process is to spin the object instead of moving the transmitter and receiver antennas around the object, as Fig. **2-10** shows. In addition, there may be only one antenna with simultaneous transmit and receive (STAR) function for the radiation pattern measurement. The STAR antenna can emit radio waves as well as receive the reflective signals from the object, hence it can reduce the interference and the inconsistent issue between the transmitting and receiving waves. The radiation pattern measurement is very time-consuming since it requires to measure all sets of (θ, ϕ) in the angular

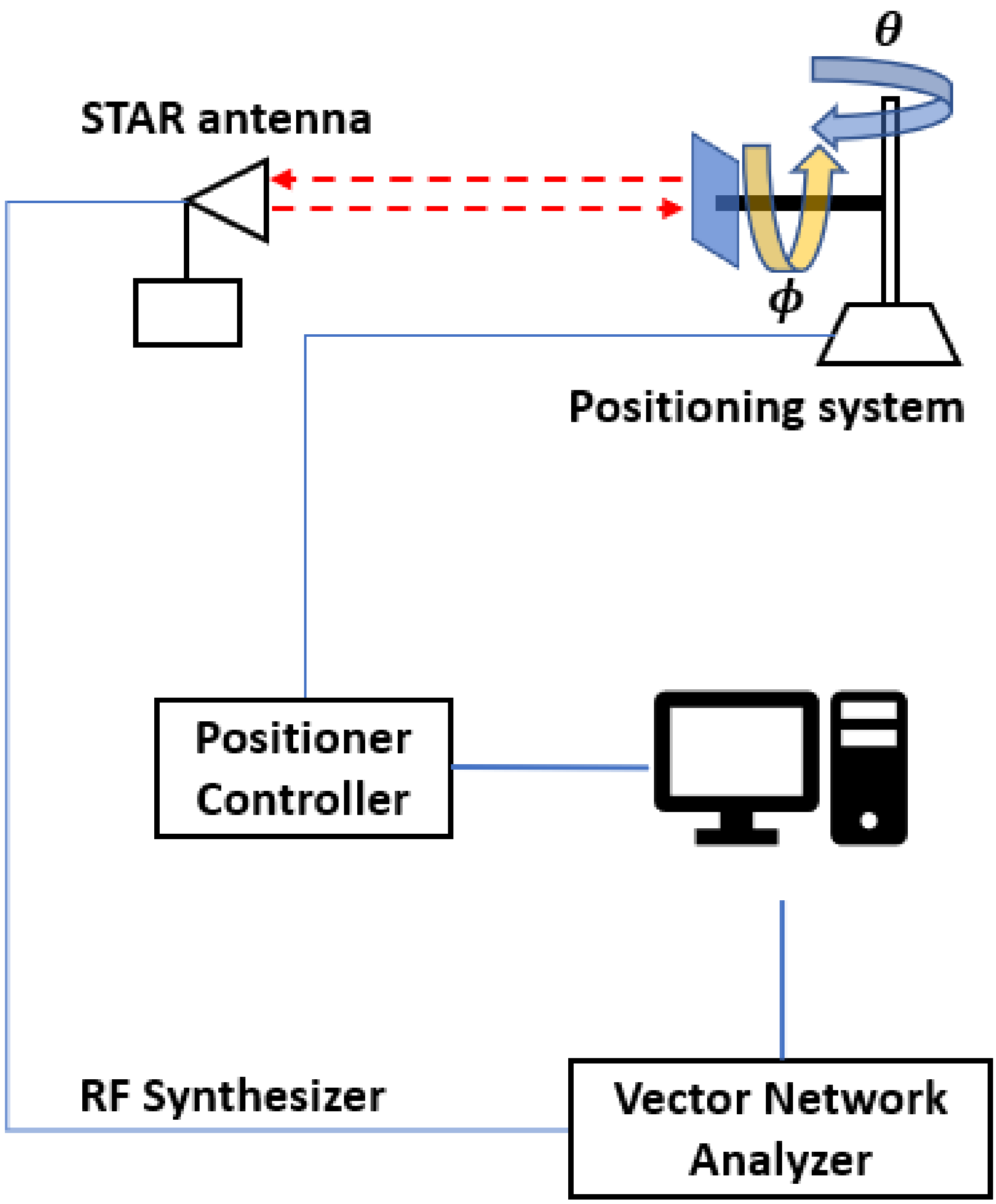

Figure 2-10 The schematic of the radiation pattern measurement. The positioner enable the rotation along θ (polar angle) and ϕ (azimuth angle) and is controlled on the work station for a steady rotation.

space. Therefore, the demand for an efficient measurement method has growing up quickly recently.

A straightforward thinking is to reduce the required measurement times. Since the radiation pattern has to be measured from the far field distance, the angle interval between each measuring point cannot be large. For instance, if doing the measurement every 5^o, the measurement will require $72 \times 36 = 2{,}092$ times to evaluate the entire spherical surface. To reduce the measurement times, an idea is to measure the pattern at the near field distance and predict the far field pattern based on the near field result. A schematic of the idea is as represented in Fig. **2-11**. Basically, the radiation pattern at far field distance does not change. However, when in the near field region, the shape of the radiation pattern is unstable and may change with the distance. The technique that transforms the measured near-field to the radiated far field pattern is called the near-field to far-field transformation (NF-FFT) [97], [98]. The prototype of NF-FFT is developed by Barrett and Barnes [99] around 1950. Barrett and Barnes are the researchers of the Air Force Cambridge Research Center. In the beginning, they built a near-field antenna scanner called "automatic antenna wave front plotter" to support the flight object scanning of radar. With this invention, they obtained a series of the phase and amplitude contour plots measured in front of a 10-wavelength reflector antenna [99]. In the next ten years, many researchers observed that there is a relationship between the near field plot and the corresponding far field pattern and tried to build the mathematical model. In 1953, Woonton [100] assumed that the voltage induced in the near field scanning probe comes from the measured electric field. In 1955, Richmond and Tice [99] made a series of experiments to calculate the far field radiation pattern from the measured near field of microwave antennas and compared to the measured far field pattern. In 1958, Kyle [101] tried to

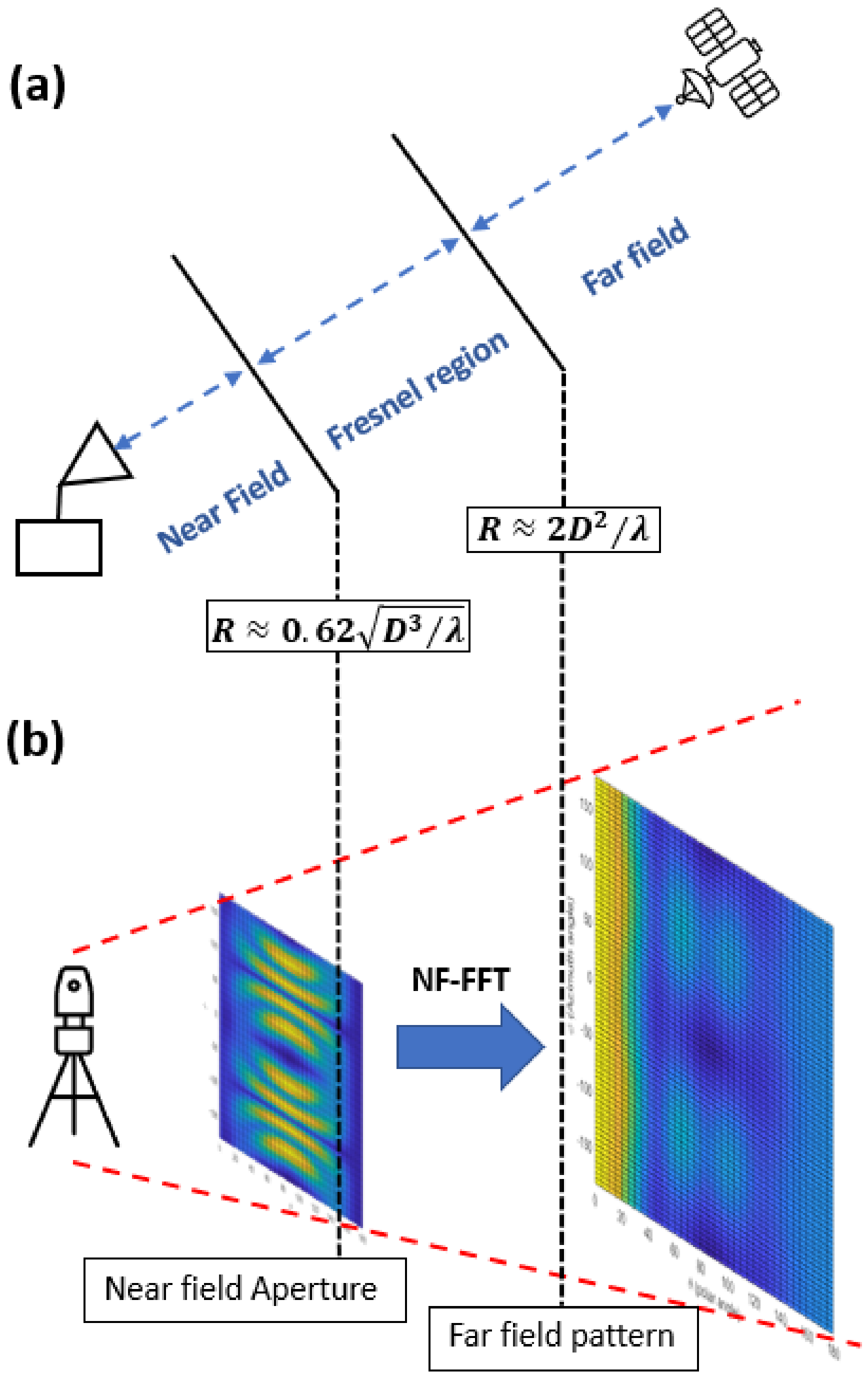

Figure 2-11 (a) The schematic of the explanation of near field, Fresnel region, and far field area. R, D, and λ are the distance from the object, the dimension of the object, and the wavelength of the radiation wave, respectively. (b) The schematic of the radiation pattern measurement using NF-FFT.

compare the far field radiation at antenna X-band (i.e., $8\ \mathrm{GHz}$ to $12\ \mathrm{GHz}$) pattern evaluated from the theoretical calculations using the amplitude and phase of the near field measurement and the direct measurements by a circular waveguide probe at the far field distance. In 1960 and 1961, Gamara and Clayton, et al. [99] did several experiments similar to Kyle's and successfully obtained the main lobe and couple side lobes that are consistent with the measurement result using the theoretical model.

In general, the transformation model in 1960 was based on the amplitude and phase of the measurement result using probe scanning which converts electrical fields to electrical voltage and current due to the technology limit. Therefore, the accuracy and consistency were not high. In 1963, Kerns [102] proposed a solution for the probe correction issue using the plane wave analysis. The modification terms by Kerns raised the accuracy of the transformation, which proved that the plane wave representation for the probe is a better choice compared to the amplitude and phase plot from the voltage change on the probe. In 1975, Wacker [103] proposed a novel transformation method using fast Fourier transformation (FFT) and several signal processing techniques. In 1977, Wood [104] developed an alternative spherical scanning technique using the Huygens probe. Then Yaghjian and Wittmann [105] derived an alternative formula with spherical transmission instead of traditional canonical form. This formula excludes the rotation and translation terms, and hance enable the direct computation of the integration in angular space under spherical coordinate.

Nowadays, the algorithms of NF-FFT for AUT are usually based on the near field measurement over a selected canonical surface [97], [98]. That is, measuring the radiation waves at near field distance using a waveguide probe or probe antenna with the aperture of specific shape. Though NF-FFT can achieve a fast evaluation of far field patterns, it is easy to be interfered with the environment. In addition, different probes also affect the transformation result. For instance, for the spherical near-field measurement, the probe antenna is required to be rotationally symmetric in its radiation pattern in order to obtain an accurate transformation [98]. Therefore, the problem is how to design a sensor that matches a specific measurement environment. To overcome the task, many optimal methods based on convex optimization algorithm have been developed [106]–[110].

Another technique is called modal expansion [98]. It is the technique that the near field is expanded in a set of orthogonal basis functions and can be transformed to the far field pattern directly. However, it still requires a strict requirement of the measurement surface due to the orthogonal basis functions. Therefore, it may not be a suitable technique for some applications, such as portable and aerial measurement systems that require a flexible measurement surface. In 2017, Y. Alvarez et al. [111] proposed a complementary technique that adds the equivalent surface currents over the measurement surface into account. With the surface current, the surface can be more arbitrary. In 2019, M. G. Fernandez et al. [112], [113] proposed a technique that reconstruct the far field pattern by combining the on-site antenna measurement using UAVs and NF measurement at spherical range in anechoic room. F. R. Varela et al. [114], [115] also proposed a multi-level spherical wave expansion for NF-FFT in 2020. Those previous works widely expand the usage of NF-FFT and make the far field radiation pattern measurement more efficient.

2.4. Mutual Coupling Effect of MIMO Systems and Reduction Methods

Though the MIMO antenna technology satisfies the demand of high data transmission rate without sacrificing the bandwidth or gain, it still encounters several challenges such as in-situ performance [116], [117], antenna size [118], [119], and mutual coupling effect [120], [121]. Among the challenges, the mutual coupling effect is one of the main reasons that affects the performance of MIMO systems. Mutual

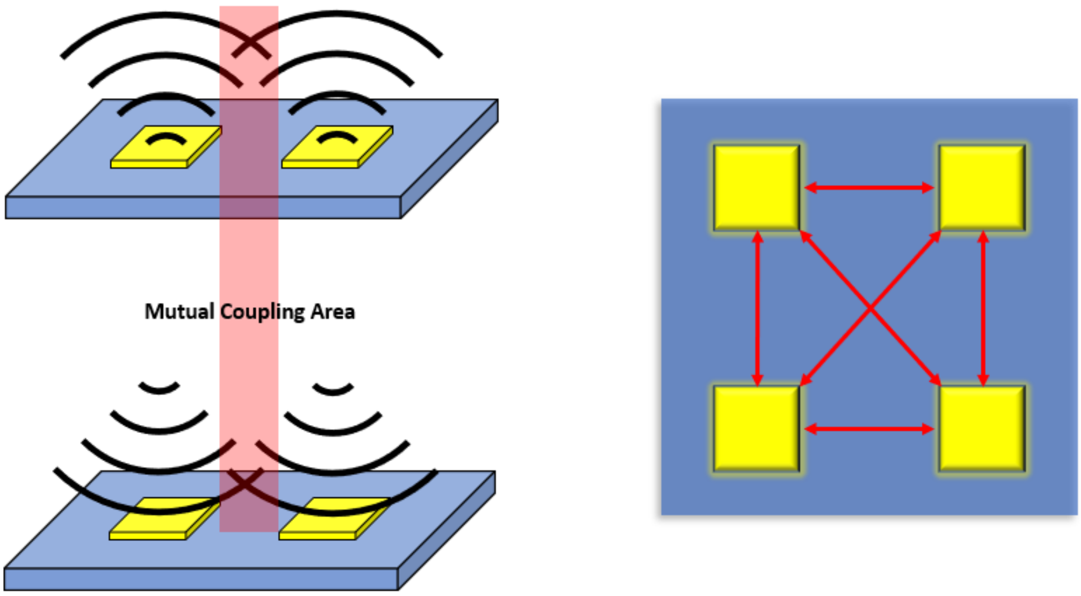

Figure 2-12 The schematic of Mutual coupling effect among the antennas. The red box and arrows mark the region the phenomenon occurs. It occurs no matter the antennas are transmitting or receiving waves (left). In addition, there may be multiple mutual couplings among the antenna elements in antenna arrays (right).

coupling refers to the electromagnetic interaction of two or multiple antennas. When two antennas are closed, the radiation wave emitting from or propagating to one antenna may affect the wave that is from or to the other antenna, result in a correlation of the wave. The mutual coupling effect not only degrades the data diversity but also reduce the gain of both antennas. Therefore, it is significant to find a way to reduce the mutual coupling effect.

A schematic diagram of mutual coupling effect in antenna arrays is represented in Fig. **2-12**. It is noticed that an antenna array may occur multiple mutual coupling between every two antennas. In addition, except for the radio wave interference, the surface wave and current flows through the substrate of the antenna array may also induce the mutual coupling effect. As shown in Fig. **2-13**, the radiation not only towards upper direction but through the substrate due to the permittivity difference between

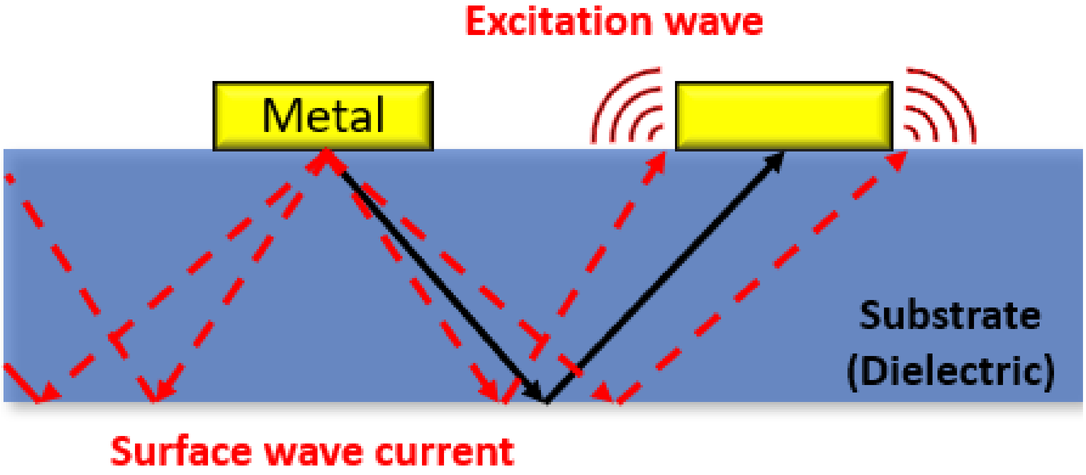

Figure 2-13 The schematic for the mutual coupling effect induced by surface waves and current flows propagating through the dielectric substrate.

the air and the dielectric material. The surface wave will dissipate after a distance depending on the attenuate coefficient of the material. However, when in antenna arrays, the surface wave may not fully disappear before propagating to other antennas, resulting in the radiation excited from the edge of the antenna and the substrate. Therefore, the proper isolation of each antenna element is essential for improving the radiation efficiency and increasing the diversity.

There are many isolation techniques for antenna arrays. A simple idea is to rearrange the antennas' alignment in the antenna array. For the antennas with specific linear polarization or narrow beamwidth of each, rearranging the alignment of the antennas can be considered as a natural isolation and enable high polarization diversity. For instance, H. Huang et al. [122], [123] proposed an orthogonal alignment technique in 2015 for the ultrawideband (UWB) MIMI antenna. The realignment benefits the antenna system $-20\ \mathrm{dB}$ more isolation without adding any complex structure. Coming out with similar ideas, W. J. Liao et al. [124] placed four inverted-F antennas orthogonally at four corners and got approximately $15\ \mathrm{dB}$ isolation compared to the

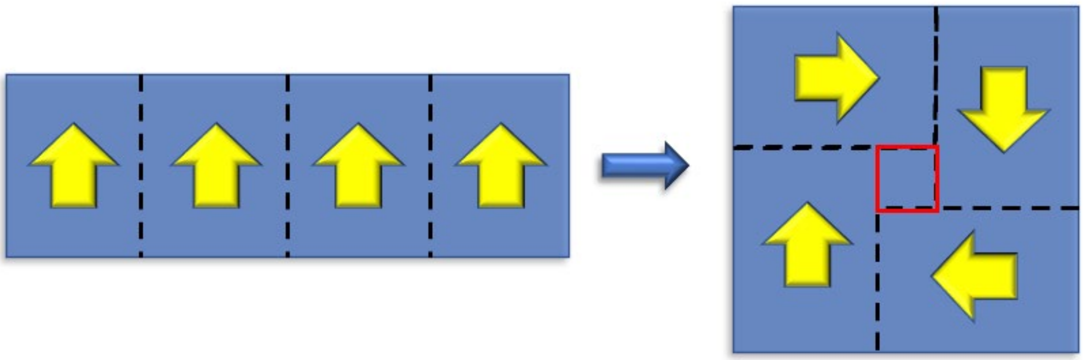

Figure 2-14 The schematic of realignment technique for mutual coupling reduction. With the rearrangement, all antenna elements are orthogonal and hence reduce the interference from others. The trade-off is a slight size increment (red box area in the middle).

antenna array with ordinary alignment in the same year. Nirdosh et al. [125] in 2018 enhanced the radiation efficiency of the T-shaped MIMO antenna operating in X-band and Ku-band by realigning the antenna elements. A schematic diagram of the realignment technique is as shown as Fig. **2-14**. It can simply achieve antenna isolation without adding any extra structures. The only trade-off is that the size of antenna arrays may become increase due to the larger alignment area. However, the condition is very limited and is case by case.

Except for the realignment, digging a trench or adding an extra structure between the antennas are also effective ideas. Though it wastes more materials and sometimes also reduces the antenna gain of each element, it enables a relatively stronger isolation since it physically blocks the radiation or surface waves propagating from one element to another. Therefore, it is powerful even for wideband or UWB antenna arrays. Among all the extra structure technique, the defected ground structures (DGSs) are the most popular one for mutual coupling reduction. Instead of modifying the geometry of the antenna array, The DGS technique digs defects on the ground plane that disturbs the propagation of surface current flows. The advantage of DGSs is that the geometry of

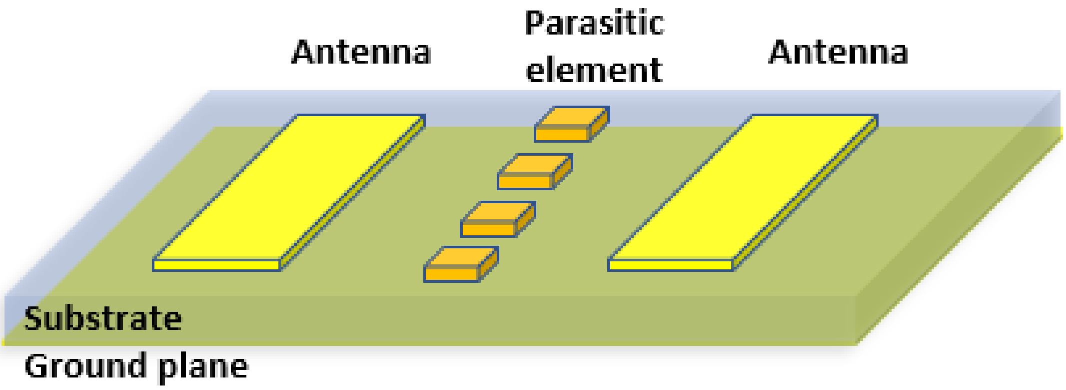

Figure 2-15 The schematic of the parasitic element implemented for mutual coupling reduction. The structure can be on the top or bottom of the antenna surface and can be used to block the surface wave as well as the radiation wave excited by the antennas.

the defect can be freely modified since it is in the different layer with the antenna structure. In addition, it can block the surface wave while not disturb the radiation wave. There are many different shapes of DGS. In 2014, MoradiKordalivand et al. [126] made a rectangular slot on the ground plane of a four elements antenna array and got $15\ \mathrm{dB}$ better than ordinary design. J. Y. Deng et al. [127] in 2017 proposed a T-shape slot DGS for a dual-band inverted-F MIMO antenna system. In 2018, D. Lu et al. [128] proposed a multi-objective optimization method for a fragment type DGS and achieve more than $30\ dB$ isolation for a bow-tie MIMO antenna array. There are still many different shape DGSs, such as H-shape [129], split ring resonator (SRR) [130], annular slots [131], meandering lines [132], and π-shape [133].

Adding parasitic structures (shown in Fig. **2-15**) between the antennas in the antenna array is another common and popular method. For a single antenna, the parasitic structure is used to enhance the resonance of the antenna without making a large antenna array. In MIMO antenna systems, the parasitic structure can be a reflector or absorber that enable the antenna isolation. In addition, with an optimal design, the parasitic structure may also enhance the radiation of the antenna elements.

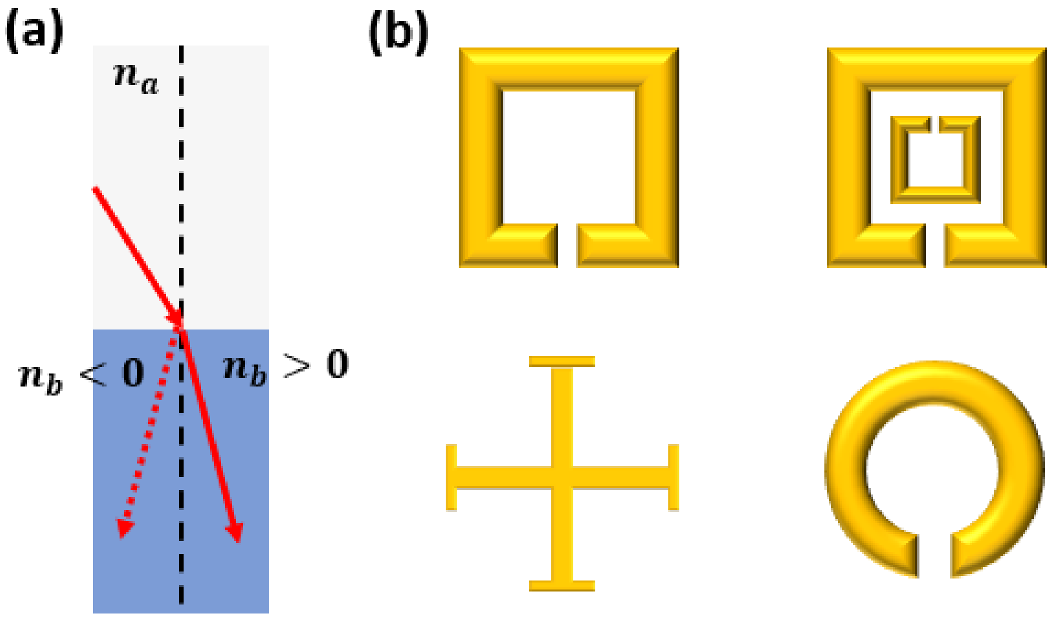

Figure 2-16 (a) The concept of negative refractive index of metamaterials. (b) The example of different types of the metamaterial structure: SRR (upper-left), CSRR (upper-right), Cross (bottom-left), and C-shape SRR (bottom-right). The FSS can be composed of either structure with the size matched the operating frequency.

Unlike other resonator, the parasitic structure does not have to connect to the ground and can construct an out-of-phase resonance that can compensate the mutual coupling effect. Moreover, a design of parasitic structures can be applied to multiple types of antennas. It is an independent element in the antenna array. For instance, H. Arun et al. [134] proposed a serpentine structure for at most $34\ \mathrm{dB}$ mutual coupling reduction of MIMO antennas in 2014. M. S. Sharawi et al. [135] applied a central metallic reflector into two kinds of dielectric resonator antennas (DRA) in 2017. Other design like L-shape [136], H-shape [137], $\times$-shape [138], or C-shape resonators [139] have been proposed and applied as the parasitic structure. Generally, parasitic structures can adjust to most of the cases while achieving high isolation no matter for narrow or wide band antennas, hence it is the most popular technique among the traditional methods.

Recently, metamaterials have also got a great concern for mutual coupling reduction. Metamaterials are an artificial material made by specific structures that enable negative permittivity and negative permeability to the materials. A schematic diagram of the concept of metamaterials is presented in Fig. **2-16**(a). Though the theory has been proposed in late twentieth century by V. G. Veselago [140], a real sample are made physically by D. R. Smith et al. [141] in 2006. Typically, matters in nature have positive permeability and permittivity larger than one. Negative properties of these two parameters lead negative refractive index, result in the opposite phenomenon of the light passing through the material. By combining metamaterials with materials in natural, the direction of light, or radiation waves can be controlled. Hence, it has a huge potential in mutual coupling reduction applications. In fact, metamaterial technique can be considered as a special case of parasitic structures. It is also implemented to the center of gap among the elements of antenna arrays. Many classical metamaterial structures have been implemented, like the split ring resonator (SRR) [142], complementary SRR (CSRR) [143], and frequency selective surface (FSS) [144]. Some examples of different types of metamaterials are shown in Fig. **2-16**(b).

In addition to metamaterials, metasurfaces are also a potential tool for mutual coupling reduction. The metasurface is a kind of metamaterials with extremely thin thickness compared to the scale of the structure so that can be considered as a 2-D surface. It is especially significant for reducing the mutual coupling from the radiation wave due to the size and weight. A famous case, proposed by H. M. Bernety et al. [145] in 2015, is to cover the strip dipole antennas in the antenna array using confocal elliptical metasurface cloaks. In the same year, Z. H. Jiang et al. [146] also proposed a similar idea with two layers quasi 2-D metasurface clocks covering two monopole antennas operating at $2.4\ \mathrm{GHz}$ and $5.2\ \mathrm{GHz}$ respectively. A schematic diagram of

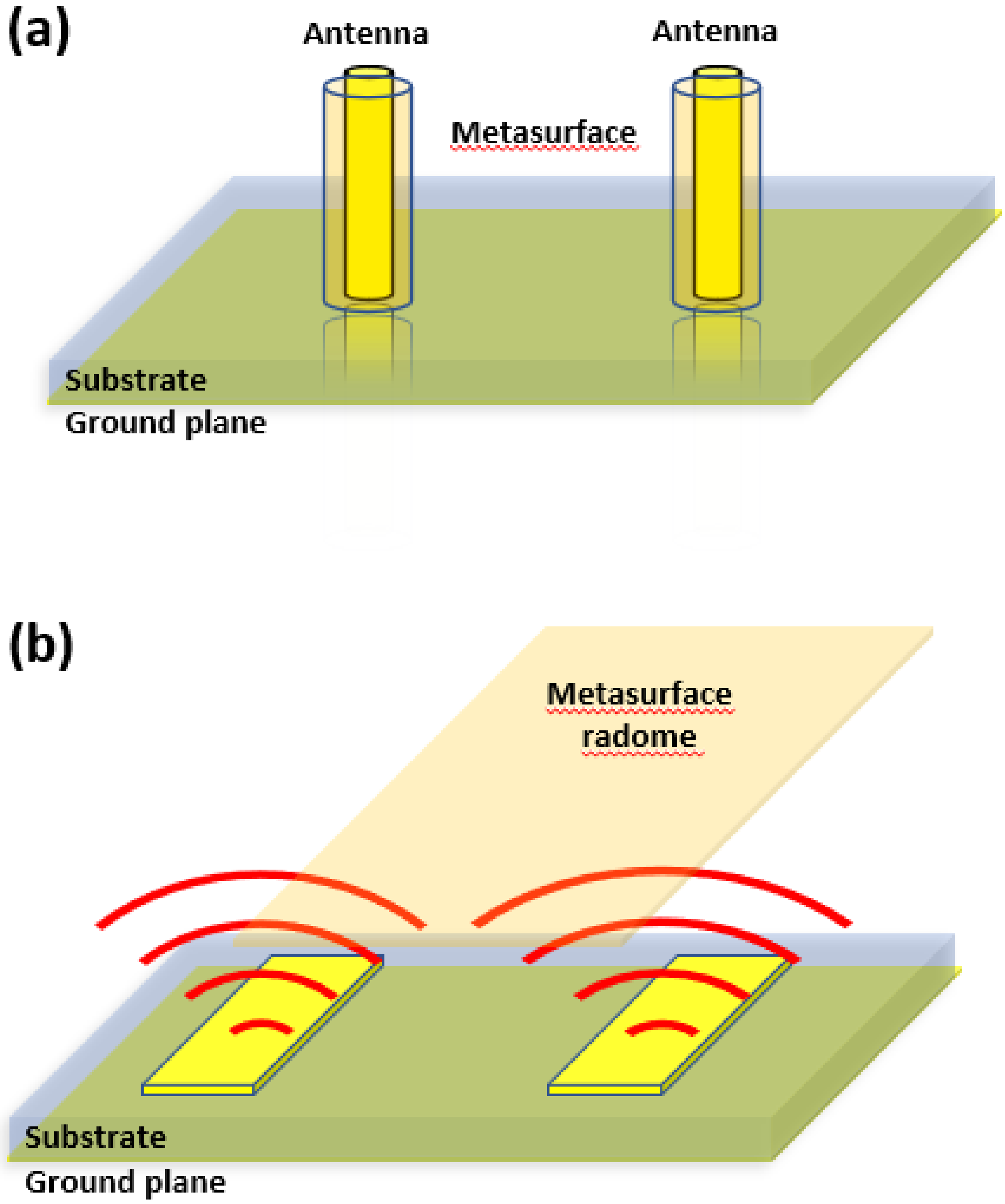

Figure 2-17 The schematic of the metasurface in different mutual coupling reduction applications: (a) Metasurface cloaks. (b) Antenna metasurface radome.

metasurface cloaks is presented in Fig. **2-17**(a). Moreover, metasurfaces can be applied to build the antenna radome covered on the top of the antenna array and achieve the mutual coupling reduction induced by radiation waves, which is shown in Fig. **2-17**(b). So far, the previous work mentioned above only focus on 2×2 or 4×4 antenna arrays due to the implement difficulty and other complex mutual coupling effect of massive MIMO systems. The metasurface radome can be placed outside of the antenna array so that it is working for even massive MIMO antenna array. As a result, metasurface radomes play a significant role in the next generation communication systems.

To quantize the mutual coupling effect, the envelope correlation coefficient (ECC) and the diversity gain (DG) are evaluated as the characteristic factors of antenna arrays. The ECC is a kind of correlation coefficient that describes the correlation among the antennas and $0 \leq ECC \leq 1$. As the schematic diagram shown in Fig. **2-18**, when two antennas placed far away from each other, $ECC = 0$, which implies that the two antennas are completely independent. When they are entering the operating area of each other, $ECC > 0$ and the mutual coupling occurs. If the two antennas are totally the same, $ECC = 1$. However, it is impossible to get an ECC exactly be 1 from two antennas since it implies not only the radiation pattern, but also the location is the same, which means that the two antennas are overlapped spatially.

Typically, the radius of the interference area is approximately half operating wavelength. ECC is proposed by Kumar et al. [147] and can be described as:

$$ECC_{i,j} = \frac{\left|\sum_{n=1}^{N} S_{i,n}^{*} S_{n,j}\right|^2}{\prod_{k=(i,j)}[1 - \sum_{n=1}^{N} S_{i,n}^{*} S_{n,j}]}$$

where S is the s-parameter of an antenna element, i and j denote the index of the element in the antenna array, and N demotes the total number of the antenna elements in the antenna array, respectively. ECC can also be evaluated by the radiation pattern from the far field. It implies the isolation level and can also be described as:

$$ECC_{i,j} = \frac{\left|\iint F_i \cdot F_j \, d\Omega\right|^2}{\iint |F_i|^2 d\Omega \cdot \iint \left|F_j\right|^2 d\Omega}$$

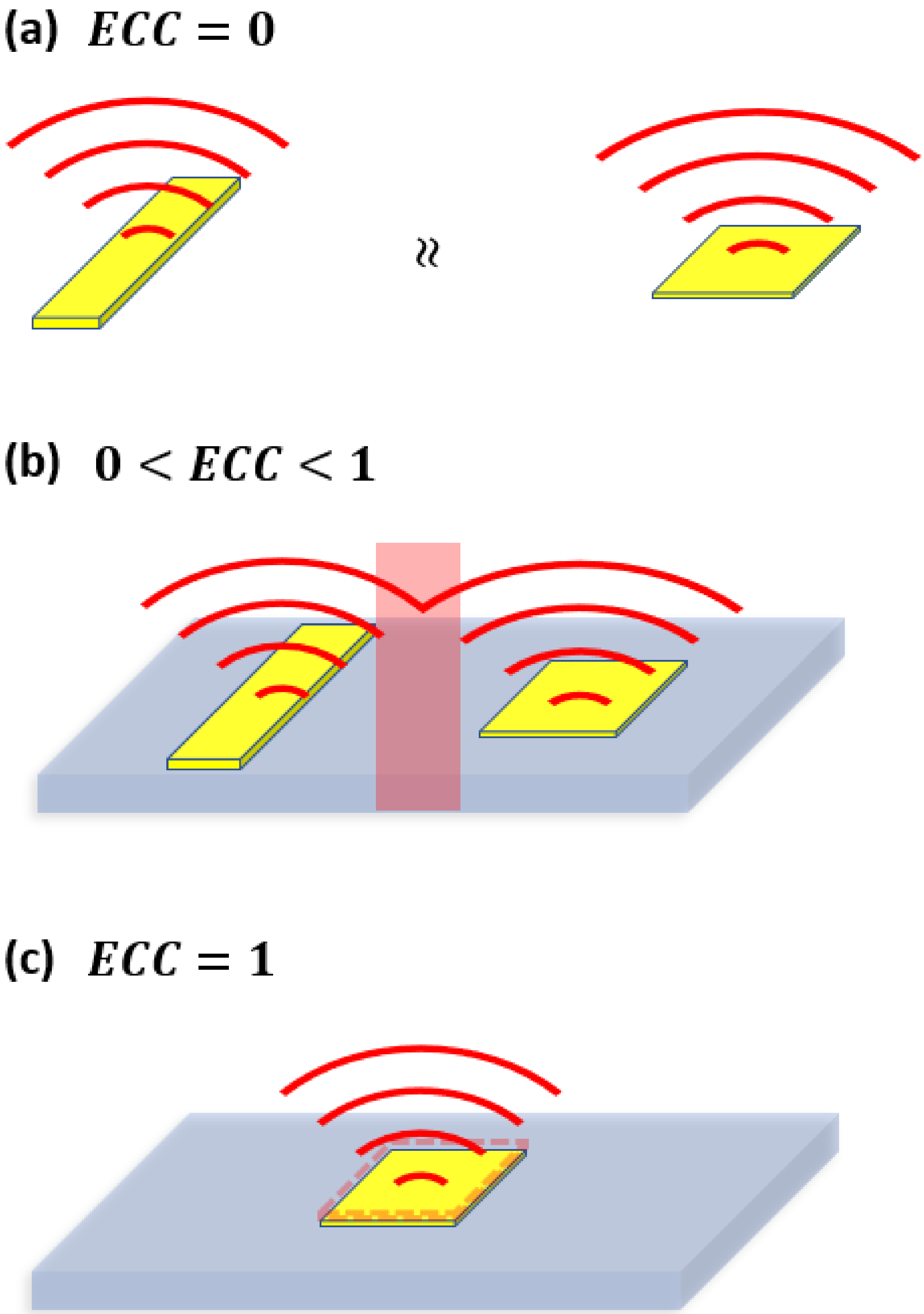

Figure 2-18 The schematic of the concept of ECC when the two antennas are (a) far away, $ECC = 0$. (b) close, $0 < ECC < 1$. (c) completely the same and overlapped, $ECC = 1$.

where $F_i(\theta, \phi)$ and $F_j(\theta, \phi)$ are the far field radiation patterns of the antenna elements taken into account. It is worthy to mention that the equation can be considered as a correlation coefficient between the two far field radiation patterns of the considered antenna elements.

$$ECC_{i,j} = \sqrt{1 - \frac{\eta_{max}}{\eta_i \eta_j}}$$

where η_{max} is the maximum efficiency, η_i and η_j are the efficiencies of the antenna elements taken into account.

On the other hand, DG represents how the MIMO antenna array improves the efficiency (gain) of the antenna compared to the single SISO antenna system. It is not built for quantizing the mutual coupling reduction originally. However, by comparing the difference of DG of the MIMO system with and without the mutual coupling reduction mechanic, it can clearly evaluate how efficient the mechanic can achieve. Followed by Kumar et al. [120], [147], DG can also be described by ECC as:

$$DG = 10 \times \sqrt{\left(1 - \left|0.99 \times ECC_{i,j}\right|\right)^2}$$

2.5. Summary

In this chapter, we present a detail explanation of the concept related to this thesis. In addition, a literature review of the related previous works is also presented. Start from the development history of antennas, the dipole antenna, monopole antenna, bow-tie and microstrip antenna, Yagi-Uda antenna, reflector antenna, horn antenna, FPC antenna, and MIMO antenna array system are introduced in Sect. 2.1. Then, a detail explanation of the performance characteristics of antennas and the measurement methods of the antenna radiation pattern and s-parameters are well described in Sect. 2.2 and 2.3. These two sections play an important role in Chapter 4. Lastly, a introduction of mutual coupling effect in MIMO antenna array systems as well as a review of the techniques for mutual coupling reduction are presented in Sect. 2.4. The mutual coupling reduction techniques include some traditional methods such as rearrangement and reorientation of the antenna elements in the MIMO system, making defects, or adding some extra parasitic structures between the antenna elements. In addition, some modern techniques, such as metamaterials and metasurface cloaks and radomes are also mentioned in the later part of Sect 2.4. This section is related to Chapter 5 which we proposed a method for metasurface radome design that can effectively reduce the mutual coupling effect from the radiation waves using deep learning models. Next, from the next chapter, we will present the work and contribution of this thesis.

3. DEGENERACY OF LIGHT SCATTERING AND ABSORPTION BY A SINGLE NANOWIRE

The content of this chapter was published as Lee, JY., Chen, YH. & Chen, PY. Degeneracy of light scattering and absorption by a single nanowire. Sci Rep 11, 18657 (2021). https://doi.org/10.1038/s41598-021-98011-x [148].

3.1. Introduction

Scattering is a fundamental problem in classical EM field. Starting from John William Strutt, also known as Lord Rayleigh, who proposed a famous theory regarding light scattering through the atmosphere called Rayleigh scattering [149], [150] in 1900, many numerous researchers have been fascinated by these optical phenomena. In 1909, German physicist Gustav Mie and Danish physicist Ludvig Lorenz [150] developed the analytical solution for the scattering of light incident into a homogeneous dielectric ball, which is called Mie theory after. Comparing to Rayleigh scattering describe the light incident into particles which size is much smaller than the wavelength (i.e., $< 0.1\lambda$), Mie theory involves all scattering phenomenon with different particle-wavelength ratio, hence including Rayleigh scattering as well. It should be noticed that when the particle size is close or equal to the wavelength, the light will be scattered nearly along its incident direction and absorbed by particle's electrons at the same time. The interest in the interaction among the radiation, scattering, and absorption keeps increasing incrementally recently since it can be applied to a vast variety of applications such as solar energy harvesting [151], [152], high directivity antenna [153]–[155], metamaterials [156], bio-sensors [157], and bio-images like magnetic resonance imaging (MRI) or computer tomography (CT) [158].

However, there are still several problems require careful inspection. For instance, scattering and absorption of an isotropic scatterer in extremely subwavelength dimension would have a single partial mode limit [159], [160]. To overcome this limit, the multi-resonant system is necessary. A composite subwavelength system with proper configurations of the multi-layer structure can induce multiple resonances at a specific frequency (i.e., degenerate resonances). It has also demonstrated that in the whispering gallery framework, excitation of a confined polariton can result in superscatterer [161]–[163]. Analogous to degenerate resonant mechanism, minimum-scattering superabsorbers, that can retain not only minimum scattering power but also arbitrarily strengthen absorption, was also demonstrated in previous works [164].

Benefit from the phase diagram for scattering coefficients, the scatterer system of each partial mode can be analyzed since the scattering, absorption, and extinction of the partial mode are bounded due to the constraint imposed by passivity and causality [165], [166]. This can provide a complete information of light scattering process in power distribution which enable the development for nano-photonics devices. However, the interferences from reality environments make the scattering situations ambiguously. It is urgent to develop a new way to completely figure out all power distributions of every scattering situation.

In this chapter, we derived an energy function related to scattering and absorption using calculus of variations and applied it to address power distribution of scatterer systems. According to the power distribution, the relation between scattering and absorption in a scatterer system can be displayed clearly. In addition, the power diagram also indicates each mode and figures out the most dominated mode in the system. In the following section, we will theoretically and numerically prove that for a linear polarized plane wave incident normally into a single nanowire, there exists a power diagram indicating all possible contributions from any arbitrary scattering situations.

3.2. General Power Diagram

Consider a cylindrical scatterer that is impinged normally by a plane wave with transverse electrical field (TE) mode, as shown in Fig. **3-1**, the power of scattering, absorption, and extinction can be expressed as:

$$P_{ext} = P_{sca} + P_{abs} = -\frac{2}{k_0}\sqrt{\frac{\varepsilon_0}{\mu_0}}|E_0|^2 \sum_{-\infty}^{\infty} Re(a_n^s)$$

$$P_{abs} = -\frac{2}{k_0}\sqrt{\frac{\varepsilon_0}{\mu_0}}|E_0|^2 \sum_{-\infty}^{\infty} [Re(a_n^s) + |a_n^s|^2]$$

where E_0 is the amplitude of incident electric field (assume $E_0 = 1$), a_n^s is complex-valued scattering coefficient, k_0 is environmental wave number, and ε_0, μ_0 are permittivity and permeability, respectively. Due to cylindrical symmetry, the scattering coefficient a_n^s is also symmetric with n, i.e., $a_n^s = a_{-n}^s$, where $n = \{0, 1, 2\}$ denotes the electric dipole, magnetic dipole, and magnetic quadrupole. As the definition, the extinction power is the summation of the scattering and absorption power. A system with non-zero absorption power must possess a scattering electric field along the forward direction. Under a no-loss condition, due to the conservation law, P_{ext} should be a constant. Hence, enhancing the absorption would reduce the scattering and lower the scattering intensity toward all directions except the scattering along forward scattering which is remain a constant.

In addition, due to the energy conservation in such a passive system, the partial absorption cross sections for each partial mode should be restricted to $-[Re(a_n^s) + |a_n^s|^2] \geq 0$, where $-[Re(a_n^s) + |a_n^s|^2]$ is defined as normalized partial absorption power. According the inequality, a physical bound of scattering coefficients for each

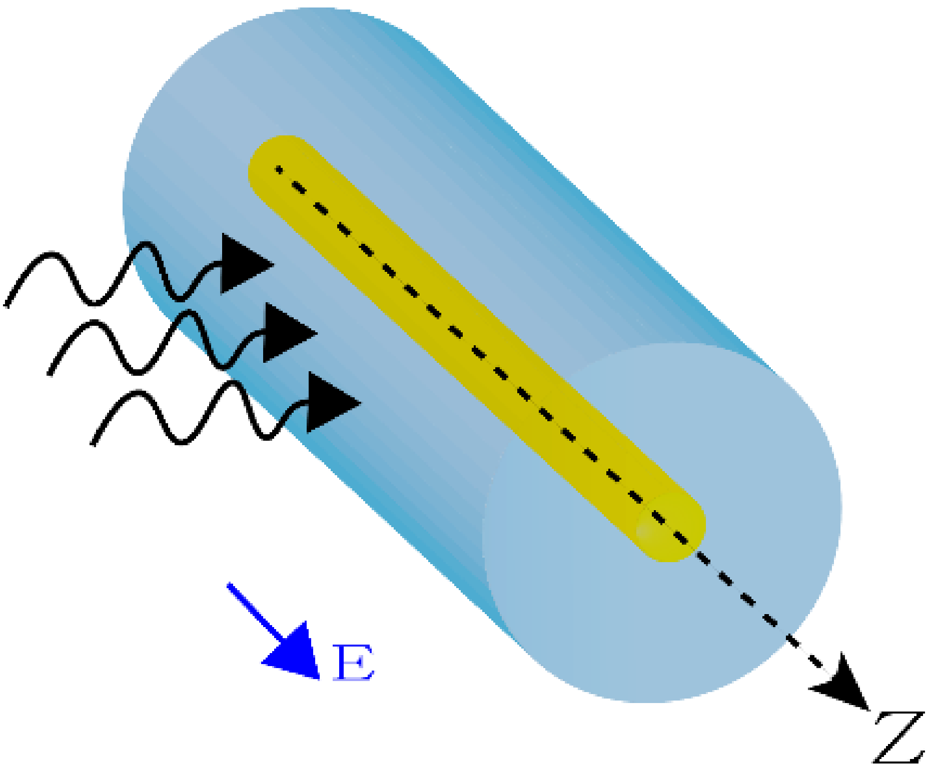

Figure 3-1 The schematic of the cylinder core-shell nanorod scatterer. A plane wave with TE mode (i.e., The electric field is always along Z-axis) impinges normally into the side of the cylinder.

partial modes, i.e. $|a_n^s| \in [0,1]$ and $Arg|a_n^s| \in [\frac{\pi}{2}, \frac{3\pi}{2}]$, is obtained. The normalized partial absorption power at each partial mode can not go beyond 0.25, while the upper limit for normalized partial scattering power, defined as $|a_n^s|^2$, is 1 for each partial mode. If a system has a N partial modes excitation, the maximum absorption power cannot over $(2N+1)\times\frac{1}{2k_0}\sqrt{\frac{\varepsilon_0}{\mu_0}}$ while the corresponding scattering power would be $(2N+1)\times\frac{1}{2k_0}\sqrt{\frac{\varepsilon_0}{\mu_0}}$ which is corresponding to multi-channel coherent perfect absorption[167], [168]. Moreover, in an extreme situation, the maximum scattering power in N partial modes can reach $(2N+1)\times\frac{2}{k_0}\sqrt{\frac{\varepsilon_0}{\mu_0}}$ while its absorption is zero.

3.3. Numerical Simulation Environment Setup

In this work, the full-wave simulation was performed using the commercially available software COMSOL Multiphysics based on the frequency-domain finite-element method (FD-FEM). Since structures studied here are infinite cylindrical nanowires, the numerical problem can be further reduced to two-dimension (2-D) scheme. Hence, we used the 2-D FEM in cylindrical coordinates to solve light scattering from such infinite uncoated and core-shell nanowires under the illumination of transverse electric (TE)-polarized plane wave (i.e., the electrical field is polarized parallel to the wire axis). The simulation space is surrounded by scattering boundary conditions (SBC) with perfect matched layers (PML) at side walls, acting as artificial absorbing layers to eliminate multipath reflection. In our simulation setups, we used approximately 200,000 triangular mesh with the size from 0.4 nm to 40 nm and a growth rate of 1.3 for each case in the adaptive mesh refinement.

3.4. Power Diagram for Multi-partial Modes

When a system is excited by multi-partial modes with arbitrary scattering coefficients, the answer for the power distribution in absorption, scattering, and extinction becomes ambiguous. Suppose a system has an absorption power $P_{abs} = Constant \equiv \eta$ contributed from N partial modes, the corresponding extreme scattering power P_{sca} and the absorption power P_{abs} can be expressed as follows:

$$P_{sca}(a_{-N}^{s}, \dots, 0, \dots, a_{N}^{s}) = \frac{2}{k_0}\sqrt{\frac{\varepsilon_0}{\mu_0}}\sum_{n=-N}^{N}|a_n^s|^2$$

$$P_{abs}(a_{-N}^{s}, \dots, 0, \dots, a_{N}^{s}) = -\frac{2}{k_0}\sqrt{\frac{\varepsilon_0}{\mu_0}}\sum_{n=-N}^{N}[Re(a_n^s) + |a_n^s|^2] \equiv \eta$$

with a constraint:

$$0 \le \eta \le (2N+1) \times \frac{1}{2k_0}\sqrt{\frac{\varepsilon_0}{\mu_0}}$$

Then, we can define an energy function L related to scattering and absorption powers as follows:

$$
\begin{aligned}
& L(a_{-N}^{s}, \ldots, 0, \ldots, a_{N}^{s}) = P_{sca} + \lambda P_{abs} \\
& = \frac{2}{k_0}\sqrt{\frac{\varepsilon_0}{\mu_0}} \sum_{n=-N}^{N} [|a_n^s|^2 - \lambda |a_n^s| \cos\theta_n - \lambda |a_n^s|^2] \\
& = \frac{2}{k_0}\sqrt{\frac{\varepsilon_0}{\mu_0}} \sum_{n=-N}^{N} [(1-\lambda)|a_n^s|^2 - \lambda |a_n^s| \cos\theta_n]
\end{aligned}
$$

where λ is the Lagrange multiplier and θ_n is the argument of a_n^s. In order to find the corresponding extreme minimum or maximum of scattering powers, the energy function L should satisfy the conditions:

$$
\frac{\partial L}{\partial |a_n^s|} = \frac{2}{k_0}\sqrt{\frac{\varepsilon_0}{\mu_0}} [2(1-\lambda)|a_n^s| - \lambda \cos\theta_n] = 0
$$

$$
\frac{\partial L}{\partial |\theta_n|} = \frac{2}{k_0}\sqrt{\frac{\varepsilon_0}{\mu_0}} [\lambda |a_n^s| \sin\theta_n] = 0
$$

where $n = -N, \ldots, 0, \ldots, N$. The second expression implies that, to obtain non-trivial solutions for λ and a_n^s, the solutions should be $\theta_n = 0$ or $\theta_n = \pi$. However, due to non-gain materials embedded, the applicable solution would be $\theta_n = \pi$. By using this outcome and the first expression, we can get $|a_n^s| = \frac{1}{2}\frac{\lambda}{\lambda-1} \equiv s$. Furthermore, $a_n^s = -s$ represents that at the extreme scattering with constant absorption, the magnitude of scattering coefficients is identical and the corresponding phases for each partial mode are π. Consequently, we can express the corresponding scattering coefficients as

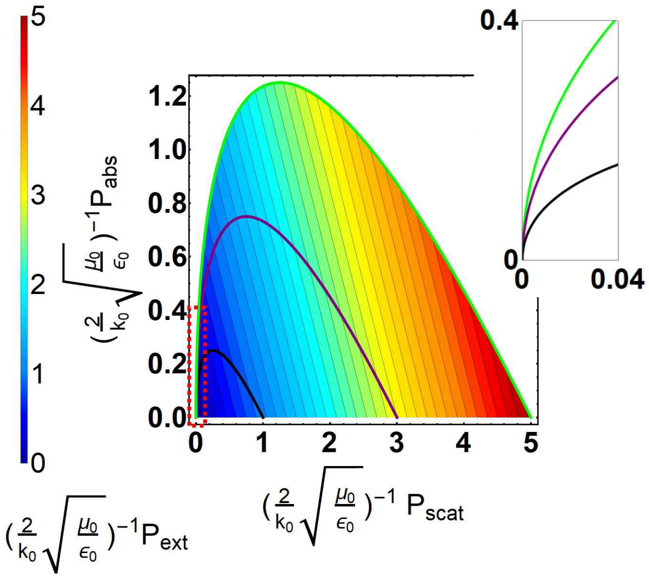

Figure 3-2 Power contour diagram for normalized absorption, scattering, and extinction powers. The black line indicates the boundary for a system with $N = 0$ mode dominant, the purple line is for $N = 1$ (i.e., $n = [-1, 0, 1]$) mode, and green line is for $N = 2$ (i.e., $n = [-2, -1, 0, 1, 2]$) mode. The red dash box highlights a region with a lower scattering but a overwhelming absorption. Inset shows the detailed power distribution among absorption and scattering for the corresponding red dashed box.

$$a_n^s = \frac{-1 \pm \sqrt{1 - \frac{2\eta k_0}{2N+1}\sqrt{\frac{\mu_0}{\varepsilon_0}}}}{2}$$

Because of the constraint $0 \leq \eta \leq (2N+1) \times \frac{1}{2k_0}\sqrt{\frac{\varepsilon_0}{\mu_0}}$, it can be guarantee that the term inside the square root is non-negative. As a result, the ultimate absorption corresponds to multi-channel coherent perfect absorptions. More appealingly, the results also imply that under a constant absorption, there can have two extreme scattering powers:

$$MAX[P_{sca}] = \frac{1}{k_0}\sqrt{\frac{\varepsilon_0}{\mu_0}}(2N+1)\left[1 + \sqrt{1 - \frac{2\eta k_0}{2N+1}\sqrt{\frac{\mu_0}{\varepsilon_0}}} - \frac{\eta k_0}{2N+1}\sqrt{\frac{\mu_0}{\varepsilon_0}}\right]$$

$$MIN[P_{sca}] = \frac{1}{k_0}\sqrt{\frac{\varepsilon_0}{\mu_0}}(2N+1)\left[1-\sqrt{1-\frac{2\eta k_0}{2N+1}\sqrt{\frac{\mu_0}{\varepsilon_0}}}-\frac{\eta k_0}{2N+1}\sqrt{\frac{\mu_0}{\varepsilon_0}}\right]$$

According to the equations, by tuning η, we can depict a clear boundary for scattering and absorption as N partial nodes are excited, as shown in Fig. **3-2**, Inside the boundary, by $P_{ext} = P_{sca} + P_{abs}$, we can make a contour plot to indicate extinction. Here $N = 0$ represents a system with only electric dipole mode supported, $N = 1$ has electric and magnetic dipole modes, and $N = 2$ has not only electric and magnetic dipole modes, but also magnetic quadrupole mode. Therefore, we can see that for a system supported by N partial modes, the occurrence of maximum normalized extinction accompanies with maximum of normalized scattering, while the corresponding normalized absorption is zero, which is corresponding to superscattering [161], [162]. Additionally, along with a constant extinction, increasing absorption would reduce scattering. The analysis of this anomalous scatterer will be discussed in the next section.

Note that for a system with N partial modes dominant, the corresponding region in the power diagram is just a sub-region of a system with higher modes. As a result, the scattering system can display the same energy performance, but its inherent scattering coefficients can be completely different.

3.5. Quasi-minimum Scattering Superabsorber and Quasi-superscatter

To verify our findings, we first discussed systems with realistic materials embedded. We designed two types of systems with different geometrical sizes, materials, and inherent configurations that are operated at the wavelength of 500 nm. According to Fig. **3-3**(a), the red line represents a core-shell nanowire system constituted by silicon in shell and gold in core, while the blue line is a homogeneous

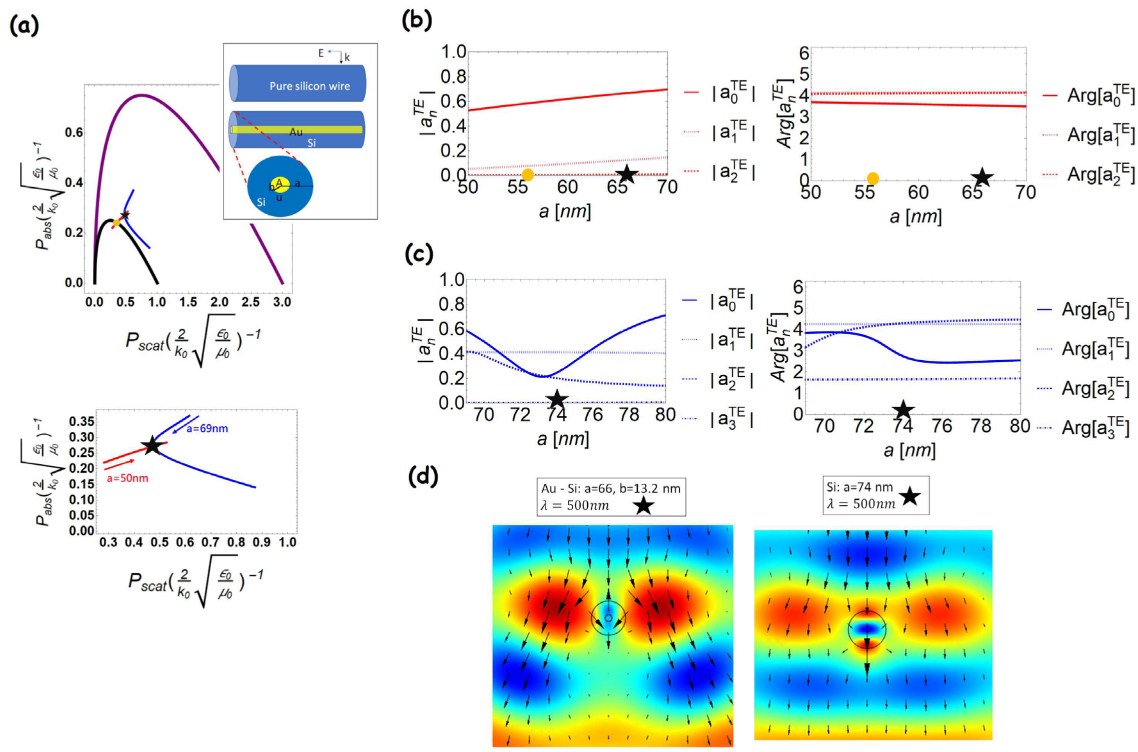

Figure 3-3 (a) Normalized scattering and absorption power diagram of two kind of systems. The red and blue lines depict the power distribution of a core-shell nanorod with silicon in shell and gold in core and a homogeneous silicon nanorod, respectively. The black and purple curves indicate the boundary of the $N=0$ and $N=1$ modes, respectively. The two systems have the same power distribution at the intersection marked by a black star. The inset shows the schematic of the core-shell nanorod. (b) The magnitude and phase of the core-shell nanorod (red line in (a)) when tuning the outer radius a from $50\,\mathrm{nm}$ to $70\,\mathrm{nm}$. The orange dot ($a=55\,\mathrm{nm}$) and black star ($a=66\,\mathrm{nm}$) indicate the intersection with the $N=0$ boundary and the homogeneous silicon nanorod system at $a=74\,\mathrm{nm}$ as the same symbol marked in (c). (c) The magnitude and phase of the homogeneous silicon nanorod (blue line in (a)) when tuning the radius a from $69\,\mathrm{nm}$ to $80\,\mathrm{nm}$. (d) Numerical simulations of the electrical field $|E_z|$ (color bar) and propagation constant k (arrows) of the two systems at the black star's location. Here the operating wavelength is $500\,nm$ and the relative permittivity ε_r of the gold and silicon are $-2.81+i3.19$ and $18.5+i0.63$, respectively.

silicon nanowire. For the core-shell system, the outer radius a is tuned from $50\,\mathrm{nm}$ to $70\,\mathrm{nm}$ with the fixed core-shell ratio of 0.2. For the homogeneous silicon nanowire, the radius is varying from $69\,\mathrm{nm}$ to $80\,\mathrm{nm}$. According to the figure, the red line is inside the $N=0$ region when a is smaller than $55\,\mathrm{nm}$, then goes through the $N=1$ region when a is larger than $55\,\mathrm{nm}$. To deeply understand its underlying mechanism, the magnitudes and phases of the dominant scattering coefficients is displayed in Fig. **3-3**(b). According to Fig. **3-3**(b), we can observe that the dominant mode in gold-silicon core-shell system is $N = 0$ (electric dipole) when $a = 50\,\mathrm{nm}$. However, with increasing a, the $N = 1$ mode (magnetic dipole) would gradually become another primary contribution. Moreover, the phase of the electric dipole mode is nearly π (out of phase) at $a = 55\,\mathrm{nm}$ when approach to the boundary of the $N = 0$ region, as expected in Fig. **3-3**(b).

In the silicon nanowire system, we depicted a blue line in Fig. **3-3**(a) by tuning the radius from $69\,\mathrm{nm}$ to $80\,\mathrm{nm}$. We also performed the mode analysis with $n = [0, 1, 2, 3]$ in Fig. **3-3**(c), which the system obviously belongs to the $N = 2$ region. This outcome reveals that although the domain of the silicon system performs as the $N = 2$ mode, it is surprisingly located at the $N = 1$ region, which reflects the degeneracy of light scattering. Furthermore, when the radius of the silicon system is $74\,\mathrm{nm}$ (as the mark of black star), the absorption, scattering, and extinction are identical to that of the gold-silicon core-shell system with the outer radius $a = 66\,\mathrm{nm}$, which can be readily understood by comparing the electric field distributions as shown in Fig. **3-3**(d). In short, the gold-silicon core-shell and homogeneous silicon nanowires can provide the same power performances in light scattering.

Next, we discussed the existence of the minimum-scattering superabsorbers, in which the system can absorb more energy while maintaining scattering by exciting more partial modes, as highlights in the red-dash box in Fig. **3-2**. Consider a core-shell nanowire system made of silicon in shell and gold in core with the outer radius of $132.98\,\mathrm{nm}$ and the inner to outer radius ratio of a fixed constant 0.42. The material dispersions are based on measurement results provided in [169]. In Fig. **3-4**(a), the power distribution of the core-shell system with varying operation wavelength λ

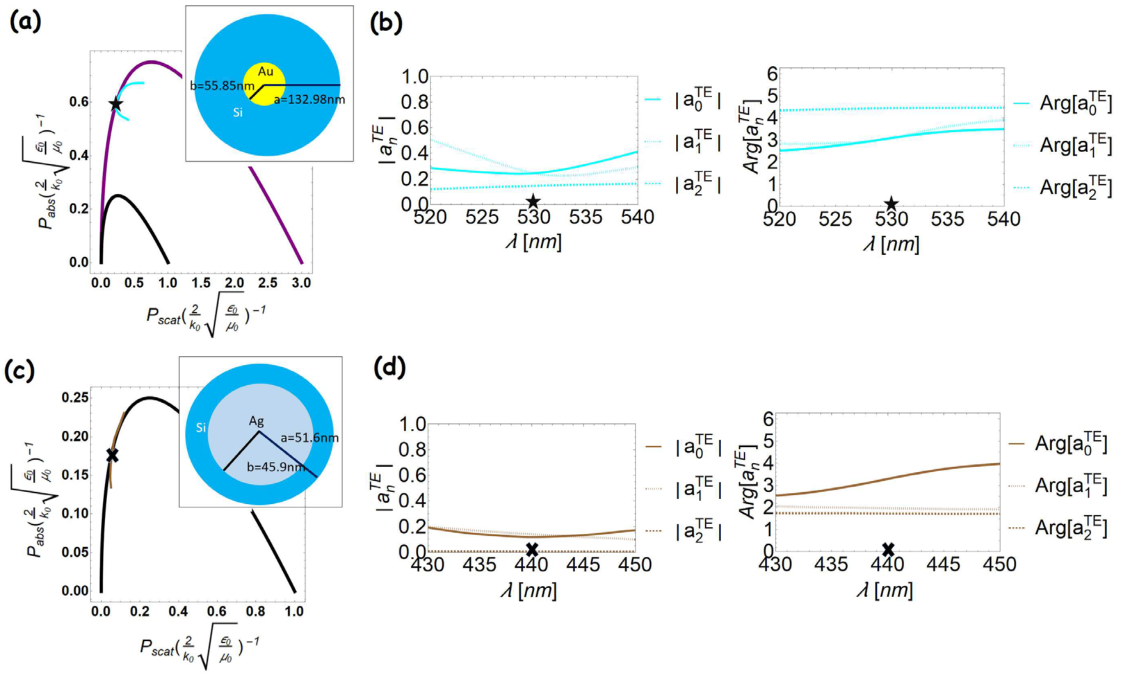

Figure 3-4 (a)(c) Normalized scattering and absorption power diagram of two kind of systems. The cyan line in (a) represents a core-shell nanorod with silicon in shell and gold in core. The outer radius $a = 132.98$ nm and the ratio of inner-outer radius is 0.42; The brown line in (c) represents the other core-shell nanorod with silicon in shell and silver in core. The outer radius $a = 51.6$ nm and the ratio of inner-outer radius is 0.89. The black and purple lines indicate the boundary of $N = 0$ and $N = 1$ modes, respectively. (b)(d) The corresponding magnitudes and phases of each partial mode for the system in (a) and (c). The operated wavelength λ is ranging from 520 nm to 540 nm and from 430 nm to 450 nm, respectively. In addition, the black star in (a)(b) and the black cross in (c)(d) are the intersection of the systems and the boundary of $N = 1$ and $N = 0$ modes, respectively.

from 520 nm to 540 nm, as denoted by the cyan line. In order to understand its inherent scattering coefficient components, we also plot the magnitudes and phases for each partial modes $n = [0, 1, 2]$, as shown in Fig. **3-4**(b). In this wavelength range, the dominant modes are $n = [-1, 0, 1]$. Note that only at $\lambda = 530$ nm, the cyan line would intersect with the boundary of the $N = 1$ mode (as the black star marks in Fig. **3-4**(a)&(b)), revealing a system with lower scattering but larger absorption. In this case, the normalized absorption and normalized scattering power are 0.6 and 0.2, respectively. In phase analysis of Fig. **3-4**(b), it is interesting to see that the phases from dominant modes at 530 nm (black star) would be π.

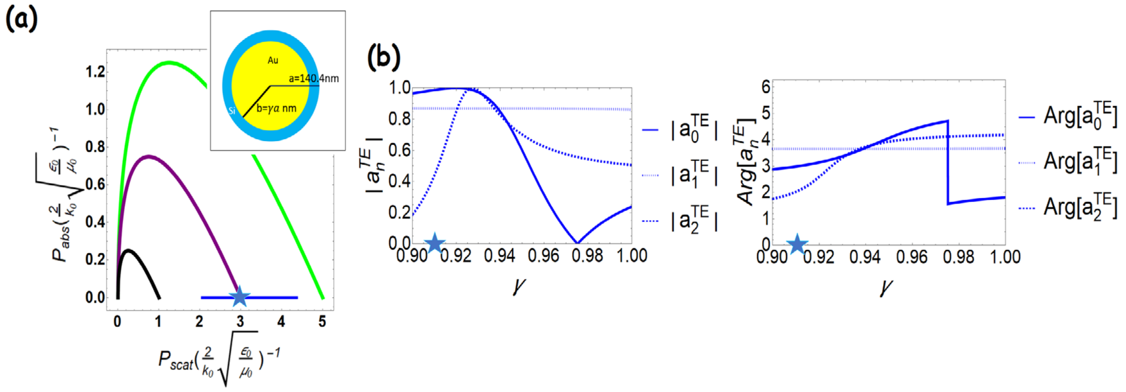

Figure 3-5 (a) Normalized scattering and absorption power distribution of a core-shell nanorod system with silicon in shell and gold in core. As the inset shows, the outer radius is fixed that $a = 140.4\ \mathrm{nm}$ and the ratio of inner-outer radius γ is varying. The blue line represents the power distribution of the system when γ is varying from 0.9 to 1 (which implies the pure gold nanorod). The black, purple, and green lines indicate the boundary of $N = 0$, $N = 1$, $N = 2$ modes, respectively. The blue star marks the intersection with the $N = 1$ boundary, which is located at $\gamma = 0.912$, as shown in (b). (b) The corresponding magnitudes and phases of each dominant scattering coefficient for the system in (a). The operated wavelength λ is fixed at $500\ \mathrm{nm}$. In addition, we assume the materials in this system are lossless, that is, the relative permittivity of gold and silicon here are -2.8 and 18.5, respectively.

Furthermore, we considered another system of silicon in shell and silver in core with an outer radius of $51.6\ \mathrm{nm}$ and the ratio of inner to outer radii 0.89. In Fig. **3-4**(c), the brown line shows the power distribution of scattering and absorption in the wavelength ranging from $430\ \mathrm{nm}$ to $450\ \mathrm{nm}$. Obviously, the system is operated in the $N = 0$ region. Here we marked the system operated at $440\ \mathrm{nm}$ by a black cross, which is the intersection with $N = 0$ boundary, with the minimum-scattering super-absorption property. The normalized absorption and normalized scattering power in this case are 0.18 and 0.05, respectively. However, the contributed modes, as shown in Fig. **3-4**(d), are $n = 0$ and $n = 1$. According to the phase analysis in Fig. **3-4**(d), the phases of dominant modes do not need to be π. In addition, this system certainly possesses the desirable power performance for a minimum-scattering superabsorber. This outcome implies that when designing a system related to energy issues, it enables an opportunity to loosen constraints of scattering coefficients when taking a system with higher partial modes into account.

In a superscattering case, the system has multiple partial modes resonances operated at same wavelength beyond a single mode limit. This mechanism results from inducing confined surface waves in multi-layered system. The constraints can be loosened by employing more higher modes excited. In Fig. **3-5**(a), a core-shell system with gold in core and silicon in shell is chosen to verify the assumption by tuning the inner to outer radius ratio γ. Here the operating wavelength is fixed to $500\ \mathrm{nm}$. In order to clearly observe the mode resonances, we assumed that the materials are lossless in this system. As shown in Fig. **3-5**(b), the blue line denotes the system with $\gamma = 0.9$ to $\gamma = 1$. We can observe that at $\gamma = 0.912$ (marked by a blue star), there is an intersection with the boundary of the $N = 1$ mode while the dominant modes are $n = [-2, -1, 0, 1, 2]$. In addition, its phases are not π, either. As a result. this system displays a superscattering behavior achieved by exciting higher partial modes, i.e., quasi-supperscatters.

3.6. Summary

In this chapter, we proposed a theoretical model that can analyze all the dominant powers of scattering, absorption, and extinction modes and represent as a general power diagram using energy functions related to scattering and absorption and math techniques such as differential calculus and Lagrange multiplier. The power diagram is irrespective of any structure configuration, materials, and operating environment. For a system containing N partial modes, there is a clear boundary in absorption, scattering, and extinction. Aling the boundary, all dominant scattering coefficients are the same. However, insides the boundary, there is no such relation for scattering coefficients. The region of a system with higher partial modes can completely cover a system with lower modes. Therefore, it can properly induce higher scattering modes to simulate the same power distribution in lower ones, which represents the degeneracy of light scattering in absorption, scattering, and extinction. In addition, we also discussed several examples of quasi-minimum scattering superabsorption and quasi-superscattering. This work not only provides the complete information for power distribution in light scattering, but also loosen degrees of freedom in practical design of power harvesting and sensing.

4. RESTORATION OF ANTENNA RADIATION PATTERN USING CONDITIONAL GENERATIVE ADVERSARIAL NETWORK

4.1. Introduction

Antenna is indispensable to wireless communication nowadays. From televisions to mobile phones, people receive information propagating using different type of antennas in their daily life. Recently, the product using 5th generation technology standard (5G) has been well-developed [170]–[172]. With high frequency band signals, the wireless transmission rate rapidly speeds up. While 5G are expected as the foundation of the next generation's technologies, there are several drawbacks needed to be improved [173]. One of the most series problems is the coverage rate. In exchange for the high speed, 5G signals are very sensitive to the environment due to the high frequency band, so that the coverage area of a 5G antenna is much smaller comparing to the antennas in previous generation. In order to make the coverage area as wide as possible in noisy environment, Unmanned Aerial Vehicles (UAVs) is used to measure the antenna radiation pattern and find the best place to set up 5G base stations recently [174]–[176]. The antenna radiation pattern plays an important role for deployment and configuration of antennas and their arrays. However, measuring an antenna's radiation pattern and gain is generally very time-consuming and is limited to specific planes or angles [97]–[99]. Hence, it is an urgent task to develop new measurement and characterization techniques that enable fast and accurate evaluation of radiation patterns of antennas placed in realistic environments.

There are many previous works studying for an efficient method of the radiation pattern measurement. One of the most popular techniques is to measure the field radiated within a short distance compared to the wavelength (i.e., Near-field region), and then evaluate the far-field radiation pattern from the near-field result, which is so-called the near-field-far-field transformations (NF-FFT) [97]–[99]. Since the near-field pattern can be achieved by scanning a small measurement plane closed to the antenna mechanically, this kind of techniques can significantly reduce the acquisition time for the required spatial measurement [99]. Then, the far-field pattern can be acquired by the Fourier Transform (FT) analysis [103], [105]. The half-wavelength spatial sampling technique for the measurement data is also developed by Nyquist-Shannon theory, which is adopted as the most efficient algorithm for NF-FFT currently.

Though NF-FFT is powerful especially when measuring the radiation pattern of large antennas, it is composed of complex mathematical models and the accuracy is easily to be affected by the tiny disturbance from the environment [177]. In addition, the finite size of the measurement plane, the presence of scattering in the environment, and the multi-reflection effect between the measurement plane and the probe can also influence the far-field pattern after the transformation [178]. As a result, it is required to search a more stable method with similar or better efficiency and accuracy.

Recently, Machine learning (ML)-assisted models become popular and have been applied into many electromagnetic (EM) problems. Some ML techniques, such as the inverse design model, shows a strong potential in the substitution of numerical simulations and optimization of metamaterials, metasurfaces, or antennas [1], [5], [19]–[21], [26]–[28], [43], [46]. In addition to the common ML-assisted models such as principal component analysis (PCA) [179], [180], support vector machines (SVM) [181], [182], or K-nearest neighbors (KNN) [183], [184], the modern models based on neural network (NN) structures present outstanding performance when dealing with a very large dataset of over millions of data amount [185]–[187]. Several NN models, such as convolutional neural networks (CNN) [188], [189], recurrent neural networks (RNN) [190], or deep neural networks (DNN) [191], [192] are commonly used in the inverse design models. In recent years, the generative adversarial networks (GAN) have also become one of the potential options since it enables accurate pattern recognition and restoration that have been validated in computer vision and image processing areas [193]–[197]. Different from traditional machine learning methods, GAN can learn how to generate new data with the same statistics as the training set and can be particularly useful for generating images that look authentic to human observers. In the field of the computer vision, it has been proved that GAN has a strong ability to dehaze or recover the blank of images [198]–[200]. In the same vein, GAN may allow one to exploit the limited measurement data to evaluate the detailed radiation pattern with sidelobes and nulls, so that extremely reduce the measuring time of UAVs.

Based on our literature review, none of prior works applied GAN to radiation pattern measurement as far as we know. Hence in this chapter, we proposed a new class of neural network architecture, generative adversarial network (GAN), that can rapidly and accurately evaluate the radiation pattern of antennas and their arrays. In our proposed method, the GAN model is trained using the simulated radiation patterns of antennas with different geometries and array configurations, which are available in our database. First, the GAN generator is fed with different antenna geometries and fragments of radiation pattern. Then, the GAN generator attempts to create (recover) the entire radiation pattern in angular space, while the discriminator will compare the similarity between the real plot obtained from full-wave simulations and the plots made by the generator. Finally, the generator is expected to complete the entire radiation pattern of the antenna, even though a few data points are known. As a result, the proposed GAN model can enable measuring the full 3-D radiation pattern of an antenna without tediously measuring the radiated power at all angles, resulting in a significant reduction in the measurement time.

4.2. Motivation

The antenna radiation pattern plays the most important role for deployment and configuration of antennas and their arrays. In general, measuring an antenna's radiation pattern and gain is very time-consuming and is limited to specific planes or angles. Hence, it is an urgent task to develop new measurement and characterization techniques that enable fast and accurate evaluation of radiation patterns of antennas placed in realistic environments, especially for the future 5G network with massive base stations in noisy environments. The proposed GAN model can enable measuring the full 3-D radiation pattern of an antenna without tediously measuring the radiated power at all angles, resulting in a significant reduction in the measurement time. We envision that the proposed technique may be beneficial for practical experimental measurements of antenna radiation patterns, radar cross sections (RCS), wireless channel capacities, as well as various radiation and scattering parameters.

4.3. Definition of Terms

The definition of the key terms in this chapter is descripted as follow:

(a) Radiation pattern

The radiation pattern refers to the directional or angular dependence of the intensity or gain of the radio waves transmitted from the source. In the field of antenna design, the radiation pattern usually implies the far-field pattern of the antenna, that is, the distribution of the intensity or power per solid angle and the directivity gain when the radio waves propagate to infinity. Due to the interferes of the radio waves, the intensity will have local maxima at the angles where the radio waves arrive in phase, and local minima at the angles where the radio waves arrive out of phase, result in the “lobes” visualized on the radiation pattern plot. For directional antennas, there is a main lobe (global maximum of the radiation pattern) at the desired angle and many side lobes which the maximum values are smaller than the maximum of the main lobe along the rest undesired directions. Fig. **4-1** represents an example of the radiation patterns of a Yagi-Uda antenna which has operating frequency at $300\ \mathrm{MHz}$. It can be seen that the antenna has a main lobe along the positive z-axis and several side lobes next to the main lobe, implies that most of the radiation waves concentrates on the top direction. In addition, the 3-D radiation pattern can be fully interpreted by two 2-D radiation patterns that from the views of the azimuth angle equals to 0^o (E-plane) and 90^o (H-plane).

(b) Antenna gain and the directivity

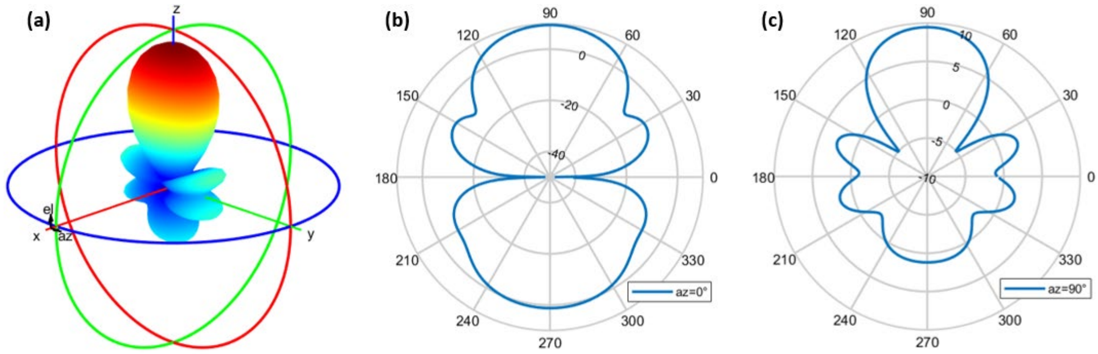

Figure 4-1 An example of the far-field radiation pattern of antennas. (a) The 3-D radiation pattern, (b) The 2-D radiation pattern with azimuth angle equals to 0^o (E-plane), and (c) The 2-D radiation pattern with azimuth angle equals to 90^o of a Yagi-Uda antenna which has operating frequency at $300\ \mathrm{MHz}$.

The antenna's gain is a key performance that describes how well the antenna converts power into radio waves in a specified direction (or desired direction of directional antennas). It is defined as the ratio of the power produced by the antenna to the power produced by the ideal (lossless) isotropic antenna, i.e.

$$G = \epsilon_{antenna} D$$

where $\epsilon_{antenna} = P_0/P_{in}$ is the efficiency and $D = U_{max}/U_0$ is the directivity of the antenna. Antenna gain and the directivity are usually expressed in decibels (dB) or decibels-isotropic (dBi).

(c) Generative adversarial network (GAN)

GAN is a type of neural networks (NN) proposed by I. Goodfellow et al. [201] in 2014. Unlike conventional NN, GAN involves two network models: the generator and the discriminator. The generator attempts to make "fake" data as real data as possible, while the discriminator tries to distinguish whether the data are fake or not. The two networks contest with each other and get the best performance eventually. Therefore, GAN is the combination of unsupervised learning and reinforcement learning. There are many applications in the field of computer vision such as image style transferring, super-resolution, and image recovering. In our proposed model, GAN is also used to recover the radiation patter from the coarse measurement data as similar as image recovering.

4.4. Procedure

The proposed method is described as Fig. **4-2** and is executed with the steps as follow:

(1) Data collection

Ideally, the desired radiation patterns of antennas were supposed to be measured in the anechoic chamber. Unfortunately, due to the covid-19 pandemic, it is limited to work in the lab and collect varieties of data for

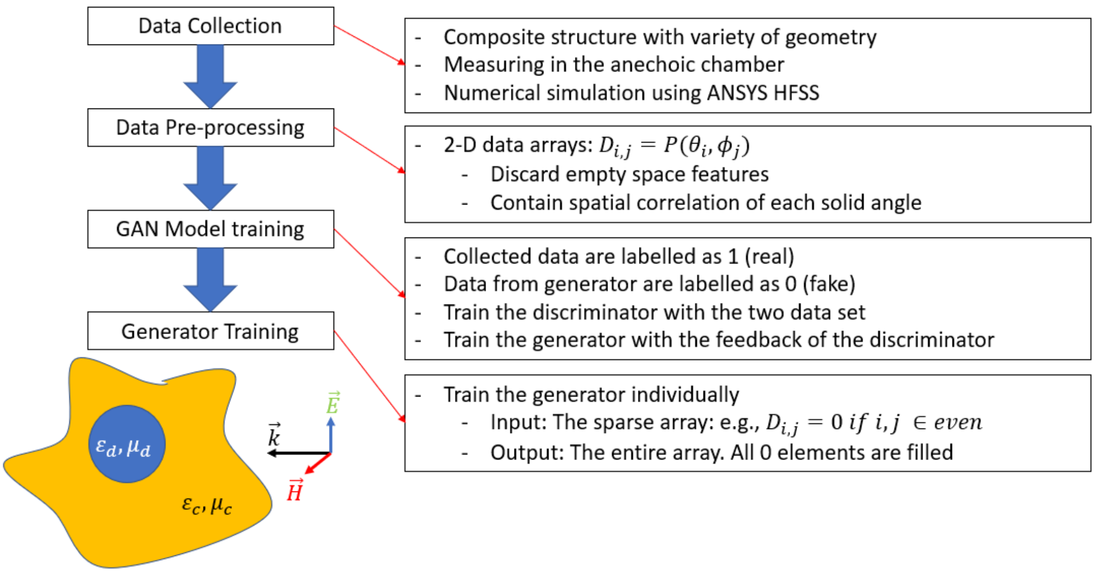

Figure 4-2 The procedure of the experiment for the proposed model. Each step is explained in detail in Sect. 5.4.

model's training. Therefore, we generated the desired data from both analytical solutions using Matlab and numerical simulation using Finite Element Analysis (FEA) for the initial training of the proposed model.

(2) Data pre-processing

Based on our initial trial, using the radiation pattern plot to train the proposed NN model is in fact inappropriate since it only consists of edges of the lobes so that the features are too less to be discriminated. As a result, the form of the dataset is transferred to the two-dimensional array D with the size of 64×64. Each element of D is the intensity measuring per solid angle, i.e.

$$D_{i,j} = I(\theta_i, \phi_j)$$

Where θ and ϕ are the polar angle (angle with respect to z-axis) and azimuth angle (angle with respect to x-axis), respectively. With this form, the blanks in the radiation pattern plot are all discarded, and the features become more concentrated. The input data fully contains the information of the radiation pattern in angular space. In addition, since the array are arranged with θ and ϕ, each element is strong correlated to its neighbor, which makes the estimation of the proposed model be more reliable.

(3) Model training

The proposed model is based on deep convolutional GAN (DCGAN) and conditional GAN (c-GAN). GAN is a mutually competitive model that consists of two NN system: the generator and discriminator. Each epoch, both the generator and discriminator are trained simultaneously. The generator generates "fake" data from an input of random Gaussian noises, and then feeds the fake data as well as the "real" data (i.e., the dataset from step (1) and (2)) into the discriminator. The discriminator learns how to distinguish the two kinds of data, while the generator improves its skill to mimic the real data and produce the data as real as possible. In order to make GAN model be usable, this procedure needs to be executed with a huge amount of iterations (approximately 500 ~ 1,000 epochs) since the goal is much more complex comparing to common NN model such as convolutional NN (CNN) or residual NN (ResNet). The rest detail of the proposed GAN models will be described in the following section in this chapter.

(4) Model validation

There are two goals in our proposed model. First, we expect the generator can not only generate the data like real one from random noises, but also restore the data measuring sparsely or with some missing part. In addition, we also expect the training enable the discriminator to distinguish the type of the antenna or object making the radiation pattern. We have tried several ways and decided to used c-GAN to achieve the goals eventually since the c-GAN model enable to generate specific data based on the additional input (which is the meaning of “conditional-”). Comparing to the mixture of DCGAN and other NN such as artificial NN (ANN) or encoder-decoder, the c-GAN model achieves the goal more directly. As a result, in this step, the condition input is the data measured sparsely. The generator of the proposed c-GAN model is expected to restore the sparse data and output the entire radiation pattern plot.

(5) Training and Testing with noisy data

In our propose, the model should be able to accurately estimate the radiation patterns measured in noisy environments. Though currently it is not available to generate this kind of data (since the experiments are necessary), we assume the next step is to make the model be able to be applied in this condition using transfer learning technique.

The rest of this chapter will introduce the concepts and tools needed in detail.

4.5. Configurations of Antennas and Radiation Patterns

To simplify the problem, we will start with Yagi-Uda antenna. Yagi-Uda antenna is an antenna array consisting of several dipole antennas which are so-called parasitic elements. The dipole antenna oriented to the desired direction are the director and driven element, while the lengthy one at the end of the structure is the reflector. The current on the reflector lags the current on the driven element by π (out of phase), result in the destructive interference so that the waves toward the direction of the reflector is cancelled. On the other hand, due to the reactance caused by the length difference, the current on the reflector adds another π phase difference to the director, leading the constructive interference of the waves toward the direction of the director. As a result, Yagi-Uda antenna has very high directivity. Yagi-Uda antenna can be designed as the microstrip antenna integrated on the chip and applied to 5G telecom due to its high directivity and simplicity of the structure. It can also apply to many wireless technologies such as Wi-Fi, Bluetooth, and RF-ID.

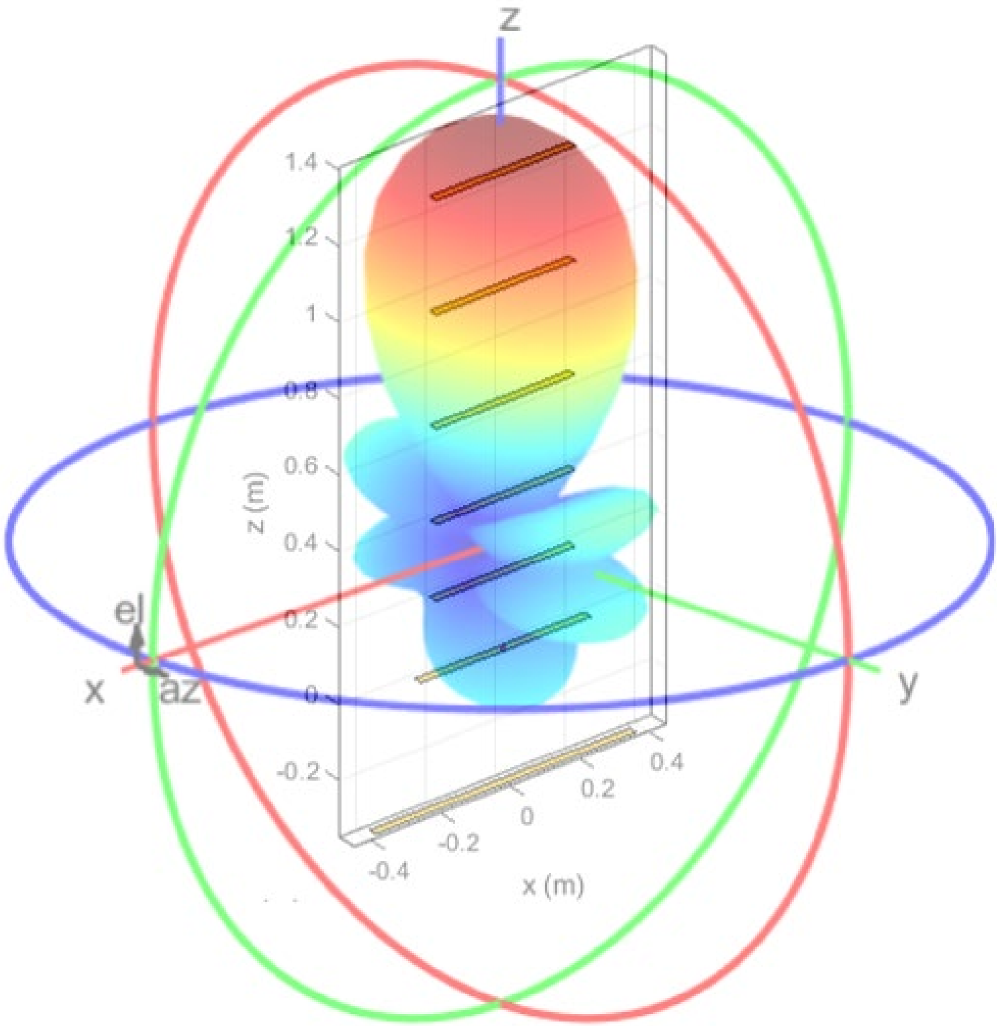

Figure 4-3 The schematic of an example of the Yagi-Uda antenna and its radiation pattern.

An example of the radiation pattern of a Yagi-Uda antenna is presented as Fig. **4-3**. The main lobe towards the forward direction (the direction of the director) with four side lobes (due to the destructive interference) toward the rest directions. Comparing to other antennas, the radiation pattern of Yagi-Uda antennas is simpler because of its high directivity, hence it is suitable to be the initial data for the proposed model. In addition to Yagi-Uda Antennas, there are also other types of antennas applied into the proposed model, such as dipole antennas and reflector antennas with different reflectors, which are shown in Fig. **4-4**.

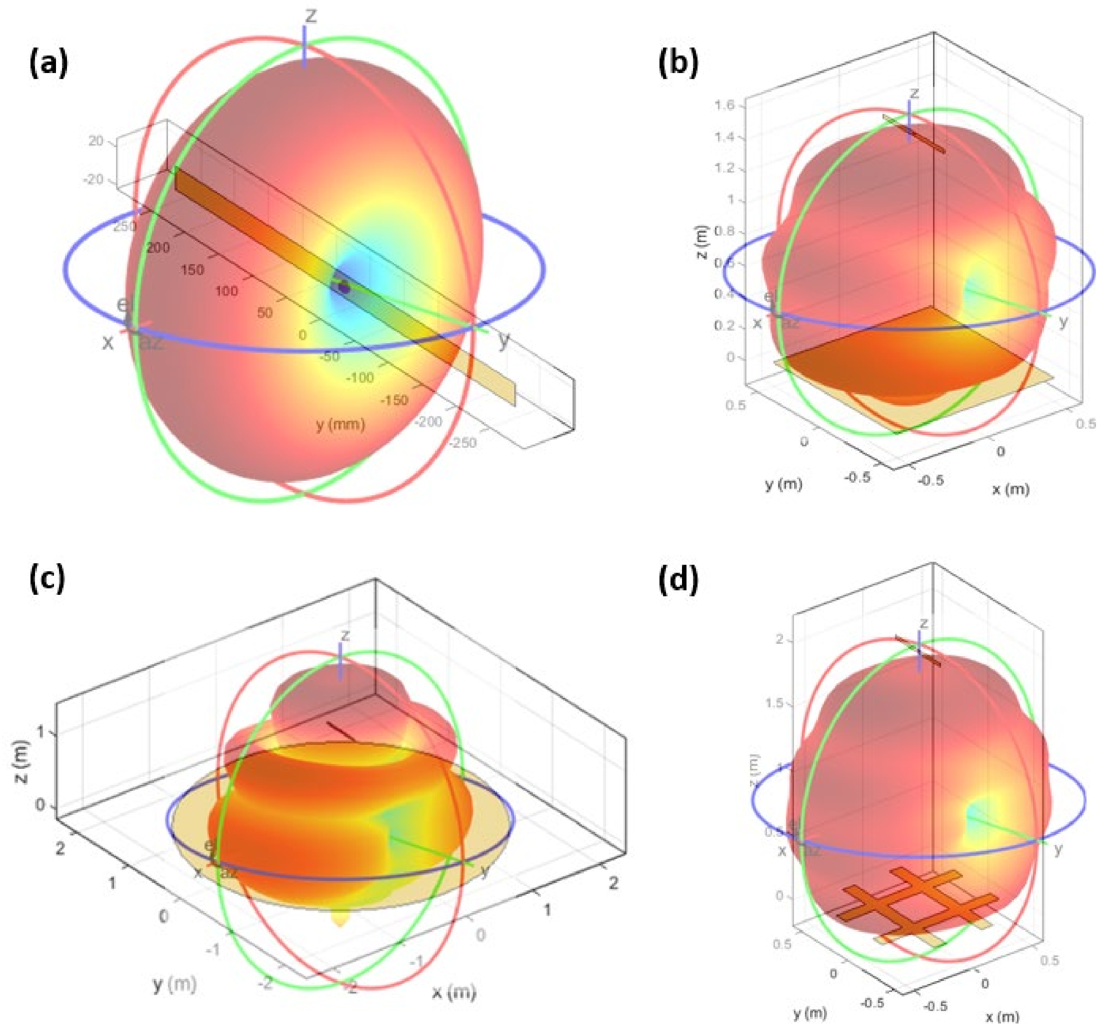

Figure 4-4 Examples for the types of antenna radiation patterns applied into the proposed model: (a) Dipole antenna and reflector antennas with (b) Plane reflector (c) Disk reflector (d) Grid reflector, respectively.

4.6. Numerical Simulation Using Finite Element Method

To well-train and validate the proposed NN models, the large amount of data is necessary. Since it is difficult to collect bunches of measurement data within a short time, the numerical simulation is a suitable substitution. We mainly use ANSYS HFSS software to simulate variety of antennas and generate their radiation patterns. ANSYS HFSS is based on the finite element method (FEM) which has been widely used to solve not only EM but also optical or mechanical problems. In FEM, the complex geometry is divided to many tiny subdomains called mesh. Each mesh contains the same environment configuration inside so that it can be represent by a set of linear equations that approximate the original complex partial differential equations (PDE) using Galerkin's formulation method:

$$\sum_{j=1}^{N} K_{ij}\varphi_j = b_i$$

where $i = 1, 2, \dots, N$ and

$$K_{ij} = \iint_{\Omega} \varepsilon\, \nabla N_i \cdot \nabla N_j d\Omega$$

$$b_i = \iint_{\Omega} \rho_e N_i d\Omega + \int_{\Gamma_N} \kappa_N N_i d\Gamma - \sum_{j=1}^{N_D} \varphi_j^D \iint_{\Omega} \varepsilon\, \nabla N_i \cdot \nabla N_j^D d\Omega$$

or in matrix form:

$$[K]\{\varphi\} = \{b\}$$

The entire problem can be analyzed by solving the equations of the meshes individually. The calculation process starts from the mesh with initial condition, and then the meshes next to the first one, and so on. The result of the previous mesh becomes the boundary condition of the next mesh, hence the process eliminate the spatial derivatives from the original PDE.

In general, the mesh is usually the triangle since it can fit any kind of the complex geometry of the structure. The angles of the mesh should not be too small in order to make the result be more accurate. Ideally, the best shape of the mesh is regular triangle. In practice, however, the mesh would be acute triangle to fit the boundary of the complex geometry of the designed structure.

4.7. Generative Adversarial Network

GAN involves two network models: the generator and the discriminator. The generator attempts to make "fake" data as real data as possible, while the discriminator tries to distinguish whether the data are fake or not. The two networks contest with each other and get the best performance eventually. Unlike common NN models, there is no explicit discrimination of the training and testing steps. All the real data are used to train the discriminator network and then the fake data made by the generator network are used to test the discriminator network. Then the generator network improve itself based on the score of the test of the discriminator.

In our model, the binary cross-entropy loss function is used to measure the performance of the discriminator model:

$$Loss = -(y\log(p) + (1-y)\log(1-p))$$

where $y = \{0, 1\}$ is the label of the correct classification (0: fake data generated by the generator network, 1: real data collected from the experiments) and p is the predicted probability of the classification by the discriminator network. In our proposed model,

$$p = \tanh\,(r_d)$$

where r_d is the output of the discriminator network.

Next, the Adam optimizer is used to modify the parameters of the network. The Adam optimizer is proposed by D. P. Kingma et al. [202] in 2014. It is an algorithm for 1st order gradient-based optimization of stochastic objective functions based on adaptive estimates of lower-order moments. The equations are straightforward to implement:

$$W \leftarrow W - \eta \frac{\widehat{m_t}}{\sqrt{\widehat{v_t} + \epsilon}}$$

where η is the learning rate and

$$\widehat{m_t} = \frac{m_t}{1 - \beta_1^t}$$

$$\widehat{v_t} = \frac{v_t}{1 - \beta_2^t}$$

with

$$m_t = \beta_1 m_{t-1} + (1 - \beta_1) \frac{\partial L_t}{\partial W_t}$$

$$v_t = \beta_2 v_{t-1} + (1 - \beta_2) \left(\frac{\partial L_t}{\partial W_t}\right)^2$$

are the momentum and velocity of the gradient, respectively.

As we mentioned in Sect. 5.4, the measuring data will be transferred to a two-dimensional array D with the shape 64×64. Each element of D contains the intensity measuring per solid angle, i.e.

$$D_{i,j} = I(\theta_i, \phi_j)$$

If we consider $D_{i,j}$ as the intensity of a pixel, the array D can be seen as a grey-scale image of size 64×64. Therefore, it is easier to load the experimental data to the model. Since for the radiation pattern, the relative intensity of each solid angle is more meaningful comparing to the absolute intensity, we can normalize the data by:

$$\widehat{D_{ij}} = \frac{D_{ij} - \min{(D_{ij})}}{\max(D_{ij}) - \min{(D_{ij})}}$$

Hence the value of all the elements of D is within the range of $[0, 1]$, which rapidly increases the accuracy of the generator network.

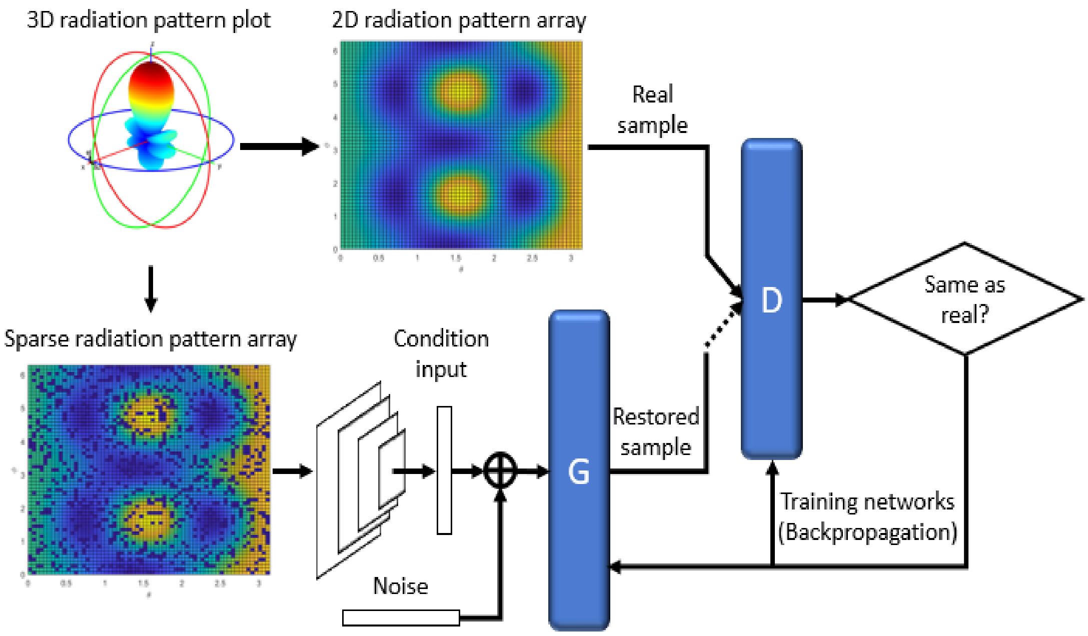

Figure 4-5 The schematic of the proposed c-GAN model. “G” and “D” imply the generator and discriminator networks of the c-GAN structure, respectively. The generator receives the 2-D sparse radiation pattern as the condition and tries to restore the entire radiation pattern. The discriminator receives the real and restored 2-D radiation pattern and attempts to distinguish which one is real. The generator keeps improving itself based on the criteria made by the discriminator and eventually learns the ability of radiation pattern restoration.

The schematic of the proposed model is represented in Fig. **4-5**. “G” and “D” imply the generator and discriminator networks of the c-GAN structure, respectively. The radiation pattern data is first transformed to 2-D spatial correlated array and normalized to $[0, 1]$. For the input of the generator, part of the information of the input radiation pattern is randomly removed (i.e., the elements are reset as zero). The generator receives the 2-D sparse radiation pattern as the condition and tries to restore the entire radiation pattern. The discriminator receives the real and restored 2-D radiation pattern and attempts to distinguish which one is real. The generator keeps improving itself based on the criteria made by the discriminator and eventually learns the ability of radiation pattern restoration.

4.8. Results and Discussion

(a) Radiation Pattern of Dielectric Ball Scattering

An initial trial using the radiation patterns of the radiation wave scattered by a dielectric ball with different size and material properties is presented in this section in order to verify the feasibility of the proposed GAN model. The measurement object and the environment are explained as follows:

A dielectric ball with permittivity ϵ_d permeability μ_d is placed in the space. An incident wave with central frequency f_n propagating toward the center of the ball. Let the incident wave function be expressed as

$$\Psi^{\mathrm{inc}}(\boldsymbol{z}) = e^{-jk\boldsymbol{z}}$$

where k is the wave number and z is the incident direction. According to Maxwell's equation, the total wave satisfies the Helmholtz equations:

$$\nabla \Psi + k^2 \Psi = 0$$

where $\Psi = \Psi^{inc} + \Psi^{sca}$ is the total field. Since Ψ is independent of the azimuth angle ϕ, it can be transferred as a scalar function of the elevator angle θ, i.e.,

$$\Psi = e^{-jkz} = e^{-jkrcos\theta}$$

By using wave transform, Ψ can be expanded as the spherical wave function

$$\Psi = \sum_{n=0}^{\infty} j^{-n}(2n+1) j_n(kr) P_n(\cos\theta)$$

Where $j_n(kr)$ are the spherical Bessel functions and $P_n(\cos\theta) = P_n^0(\cos\theta)$ are the Legendre polynomials. Therefore, the θ- and ϕ-components of the incident electrical and magnetic fields are

$$E_\theta^{inc} = -\frac{E_0 \cos\phi}{kr}\sum_{n=1}^{\infty} j^{-n}\frac{2n+1}{n(n+1)}\left[j\hat{J}_n'(kr)\frac{dP_n^1(\cos\theta)}{d\theta} + \hat{J}_n(kr)\frac{P_n^1(\cos\theta)}{\sin\theta}\right]$$

$$E_\phi^{inc} = \frac{E_0 \sin\phi}{kr}\sum_{n=1}^{\infty} j^{-n}\frac{2n+1}{n(n+1)}\left[j\hat{J}_n'(kr)\frac{P_n^1(\cos\theta)}{\sin\theta} + \hat{J}_n(kr)\frac{dP_n^1(\cos\theta)}{d\theta}\right]$$

$$H_\theta^{inc} = -\frac{H_0 \sin\phi}{kr}\sum_{n=1}^{\infty} j^{-n}\frac{2n+1}{n(n+1)}\left[\hat{J}_n(kr)\frac{P_n^1(\cos\theta)}{\sin\theta} + j\hat{J}_n'(kr)\frac{dP_n^1(\cos\theta)}{d\theta}\right]$$

$$H_\phi^{inc} = -\frac{H_0 \cos\phi}{kr}\sum_{n=1}^{\infty} j^{-n}\frac{2n+1}{n(n+1)}\left[\hat{J}_n(kr)\frac{dP_n^1(\cos\theta)}{d\theta} + j\hat{J}_n'(kr)\frac{P_n^1(\cos\theta)}{\sin\theta}\right]$$

Where $\hat{J}_n(kr)$ are the Riccati-Bessel functions and $E_r^{inc} = H_r^{inc} = 0$ since there is no electrical and magnetic fields along the direction of wave propagation. The analytical solution of the scattering fields can be obtained from the incident fields:

$$E_r^{sc} = E_0\frac{\cos\phi}{j(kr)^2}\sum_{n=0}^{\infty} a_n n(n+1)\hat{H}_n^{(2)}(kr)P_n^1(\cos\theta)$$

$$E_\theta^{sc} = -\frac{E_0 \cos\phi}{kr}\sum_{n=1}^{\infty}\left[a_n j\hat{H}_n^{(2)'}(kr)\frac{dP_n^1(\cos\theta)}{d\theta} + b_n\hat{H}_n^{(2)}(kr)\frac{P_n^1(\cos\theta)}{\sin\theta}\right]$$

$$E_\phi^{sc} = \frac{E_0 \sin\phi}{kr}\sum_{n=1}^{\infty}\left[a_n j\hat{H}_n^{(2)'}(kr)\frac{P_n^1(\cos\theta)}{\sin\theta} + b_n\hat{H}_n^{(2)}(kr)\frac{dP_n^1(\cos\theta)}{d\theta}\right]$$

$$H_r^{sc} = H_0\frac{\sin\phi}{j(kr)^2}\sum_{n=0}^{\infty} b_n n(n+1)\,\hat{H}_n^{(2)}(kr)P_n^1(\cos\theta)$$

$$H_\theta^{sc} = -\frac{H_0 \sin\phi}{kr}\sum_{n=1}^{\infty}\left[a_n\hat{H}_n^{(2)}(kr)\frac{P_n^1(\cos\theta)}{\sin\theta} + b_n j\hat{H}_n^{(2)'}(kr)\frac{dP_n^1(\cos\theta)}{d\theta}\right]$$

$$H_\phi^{sc} = -\frac{H_0 \sin\phi}{kr}\sum_{n=1}^{\infty}\left[a_n\hat{H}_n^{(2)}(kr)\frac{dP_n^1(\cos\theta)}{d\theta} + b_n j\hat{H}_n^{(2)'}(kr)\frac{P_n^1(\cos\theta)}{\sin\theta}\right]$$

And the internal fields due to the refraction are

$$E_r^{int} = E_0 \frac{\cos\phi}{j(k_d r)^2} \sum_{n=0}^{\infty} c_n n(n+1) \hat{J}_n(kr) P_n^1(\cos\theta)$$

$$E_\theta^{int} = -\frac{E_0 \cos\phi}{k_d r} \sum_{n=1}^{\infty} \left[c_n j \hat{J}_n'(k_d r) \frac{dP_n^1(\cos\theta)}{d\theta} + d_n \hat{J}_n(k_d r) \frac{P_n^1(\cos\theta)}{\sin\theta} \right]$$

$$E_\phi^{int} = \frac{E_0 \sin\phi}{k_d r} \sum_{n=1}^{\infty} \left[c_n j \hat{J}_n'(k_d r) \frac{P_n^1(\cos\theta)}{\sin\theta} + d_n \hat{J}_n(k_d r) \frac{dP_n^1(\cos\theta)}{d\theta} \right]$$

$$H_r^{int} = E_0 \frac{\sin\phi}{j\eta_d (k_d r)^2} \sum_{n=0}^{\infty} d_n n(n+1) \hat{J}_n(k_d r) P_n^1(\cos\theta)$$

$$H_\theta^{int} = -\frac{E_0 \sin\phi}{\eta_d k_d r} \sum_{n=1}^{\infty} \left[c_n \hat{J}_n(k_d r) \frac{P_n^1(\cos\theta)}{\sin\theta} + d_n j \hat{J}_n'(k_d r) \frac{dP_n^1(\cos\theta)}{d\theta} \right]$$

$$H_\phi^{int} = -\frac{E_0 \cos\phi}{\eta_d k_d r} \sum_{n=1}^{\infty} \left[c_n \hat{J}_n(k_d r) \frac{dP_n^1(\cos\theta)}{d\theta} + d_n j \hat{J}_n'(k_d r) \frac{P_n^1(\cos\theta)}{\sin\theta} \right]$$

The coefficients a_n, b_n, c_n, d_n can be obtained using the boundary conditions

$$\left[E_\theta^{inc} + E_\theta^{sc}\right]_{r=a} = \left[E_\theta^{int}\right]_{r=a}$$

$$\left[E_\phi^{inc} + E_\phi^{sc}\right]_{r=a} = \left[E_\phi^{int}\right]_{r=a}$$

$$\left[H_\theta^{inc} + H_\theta^{sc}\right]_{r=a} = \left[H_\theta^{int}\right]_{r=a}$$

$$\left[H_\phi^{inc} + H_\phi^{sc}\right]_{r=a} = \left[H_\phi^{int}\right]_{r=a}$$

We can then evaluate the radiation pattern, or in other words, the intensity of the scattering wave at a long distance far from the dielectric ball per solid angle as

$$[I_r(\theta,\phi)]_{r \gg a} = \sqrt{[\left||E^{sc}|\right|^2 + \left||H^{sc}|\right|^2]_{r \gg a}}$$

Since the I_r are arranged as an array in angular space, the intensity of the radiation patterns can be plotted as a 2-D intensity or contour images. An example of

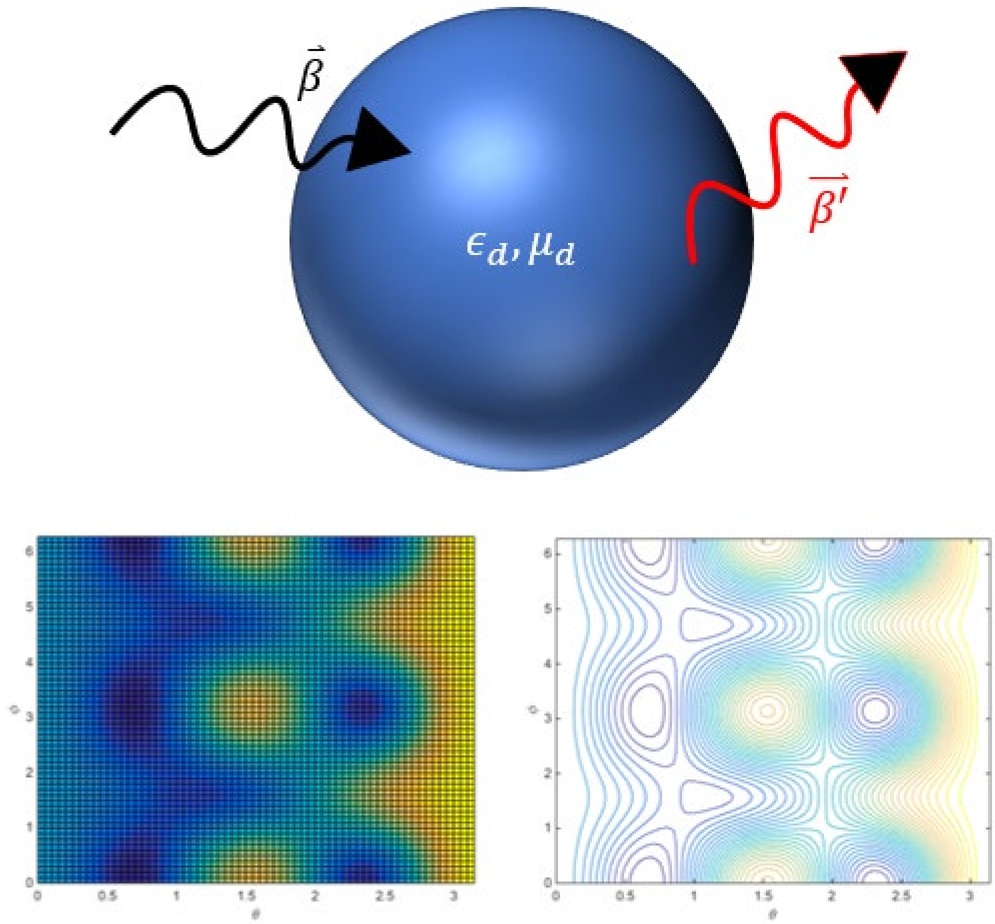

Figure 4-6 An example of the intensity (left) and contour (right) 2-D radiation pattern plots of the radiation wave scattered by a dielectric ball with permittivity ϵ_d and permeability μ_d.

the 2-D radiation pattern plot is shown in Fig. **4-6**.

A complete 2-D radiation pattern dataset is generated by the analytical solution derived in the previous paragraph using the Matlab-kernel and is fed into the proposed GAN model to validate if GAN can generate the radiation plot similar or the same as Fig. **4-6**. In our proposed model, the discriminator network consists of five convolution layers with batch-normalization layers of each that extract features of the data arrays. In the last layer, a non-linear activate function, $\tanh(\cdot)$, is applied to regularize the outputs to [0, 1], which represents the probability of how real of the input data. On the other hand, the generator network consists of the same number of deconvolution layers as the discriminator network and is fed with a Gaussian noise. The outputs are

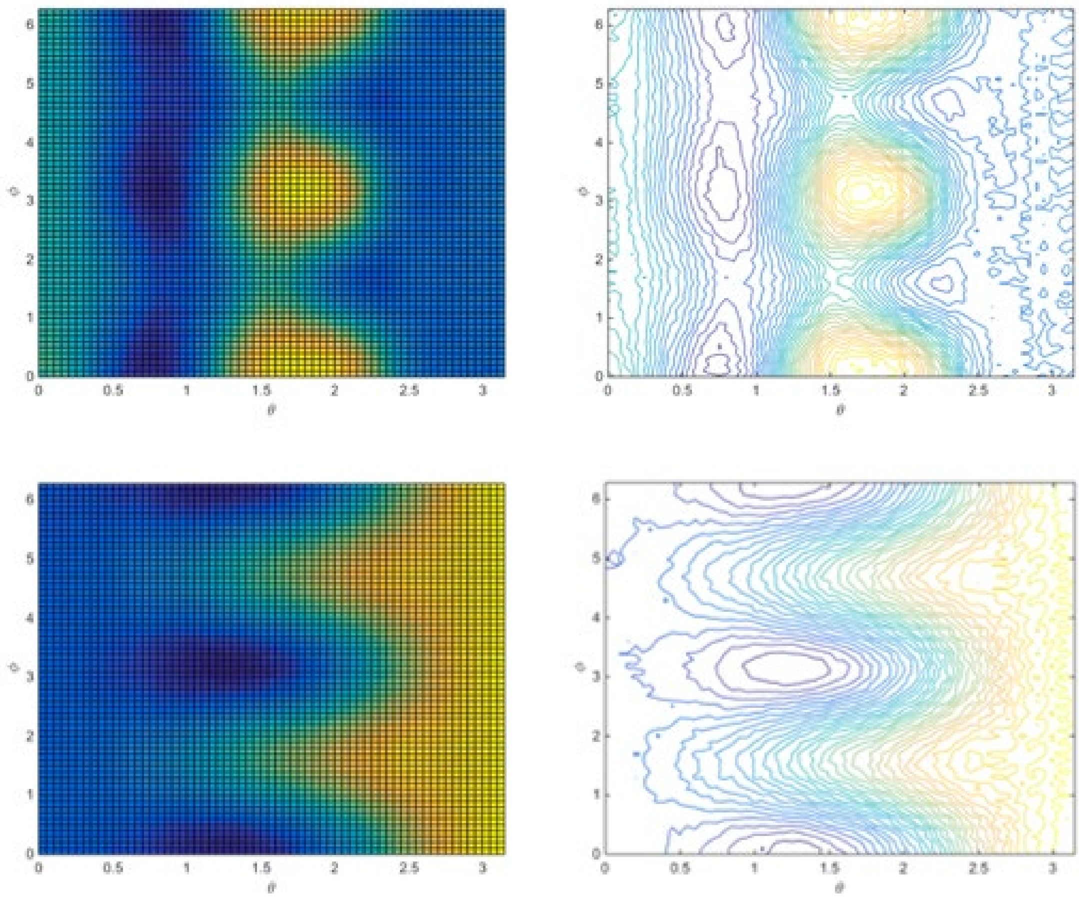

Figure 4-7 The 2-D radiation patterns generated using the proposed GAN model. The intensity plots (left) show that GAN can produce radiation patterns as real. The contour plots (right) show the detail of the generated radiation patterns.

the intensity array of the size 64×64. Two samples of the radiation pattern plotted by the proposed GAN model are shown as Fig. **4-7**. It is proved that the GAN model has the strong potential in generating the 2-D radiation pattern plots. It is noticed that the contour plots in the right side of Fig. **4-7** also contains some noises especially at the location with weak intensities. This is due to the limitation of GAN and can be improved using the low pass filter when in the post-processing step.

In this experiment, we also test different kinds of the GAN structure and different pre-processing methods to find the optimal model since GAN is difficult to find a set of optimal parameters theoretically. The result in Fig. **4-7** is plotted by the model with the best performance comparing to others.

(b) Antenna Radiation Patterns Restoration Using C-GAN

The second experiment is to restore the real antenna radiation patterns with the sparse radiation pattern that some information is missing. Radiation patterns of several types of the antenna are generated using the Matlab kernel and the numerical simulation. The type of antennas includes dipole antennas, Yagi-Uda antennas, reflector Antennas with the plane, disk, parabolic, corner, and grid reflectors. Several samples of the antenna radiation patterns are displayed in Fig. **4-3** and **4-4**. Here we display a few more antenna radiation pattern’s samples as well as the pre-processing procedure, as Fig. **4-8**. In addition, the proposed condition-GAN (c-GAN) model is represented in Fig. **4-5**. The result for the pattern restoration is as shown in Fig. **4-9**. In order to prove that the proposed model can recognize the sparse radiation pattern and restore the missing elements, we list five examples from the test dataset that is not involved in the training procedure. According to Fig. **4-9**, it is proved that the sparse antenna radiation patterns can actually be well-recovered from the proposed GAN model. Similar as Sect. 5.8(a), some noises appear in the restored patterns. However, as the amount of data increases, the proposed model becomes more stable. In fact, most of the noises happened at low intensity areas, while the parts where the modes locate are nearly the same as the original radiation pattern, which implies the powerful potential for radiation pattern restoration of the proposed c-GAN model.

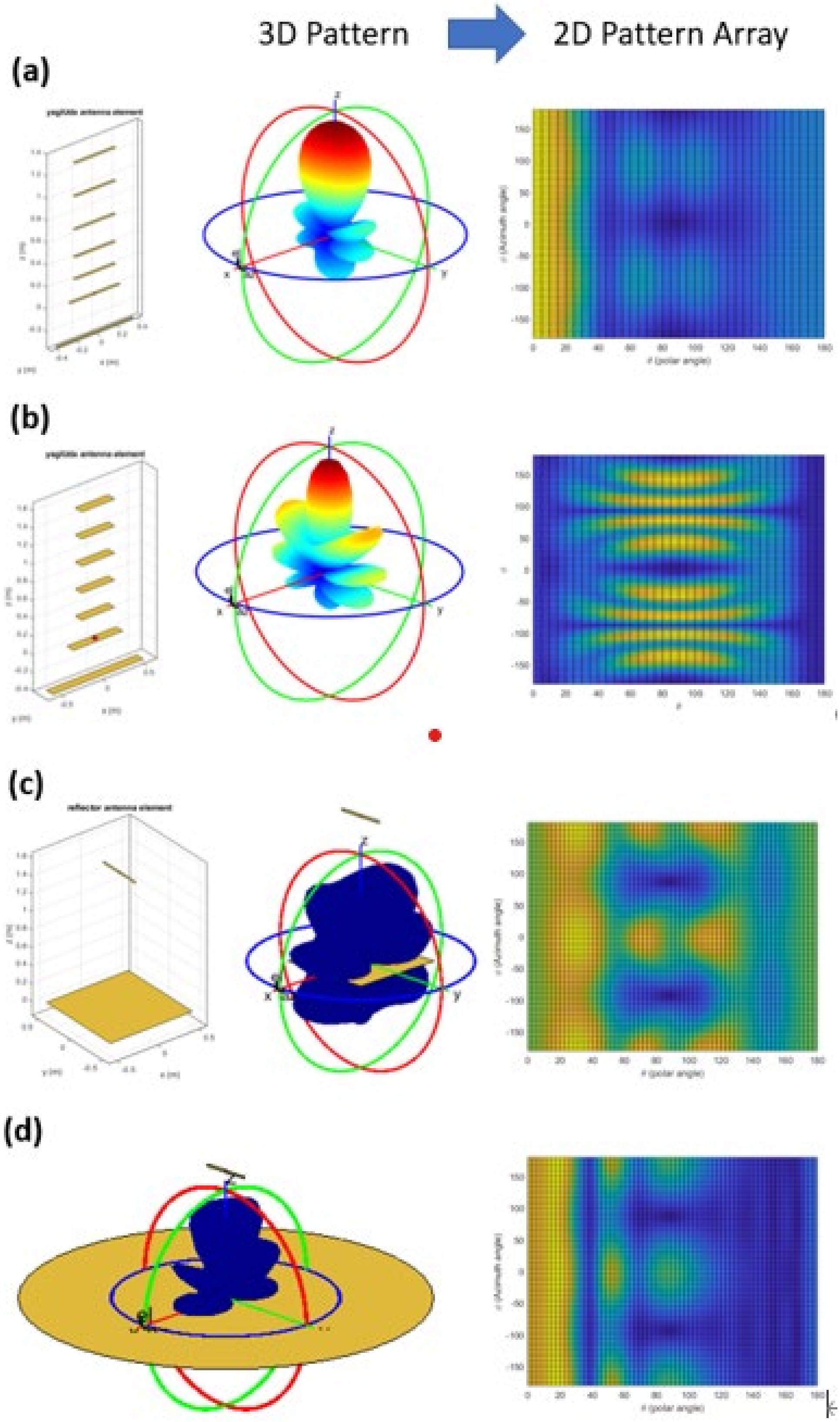

Figure 4-8 Samples for the antenna radiation patterns used in the proposed c-GAN model. (a)(b) Yagi-Uda antennas. (c)(d) Reflector antennas. Each samples contain the schematic of the antenna structure, the 3-D radiation pattern, and the 2-D radiation pattern used to train the model.

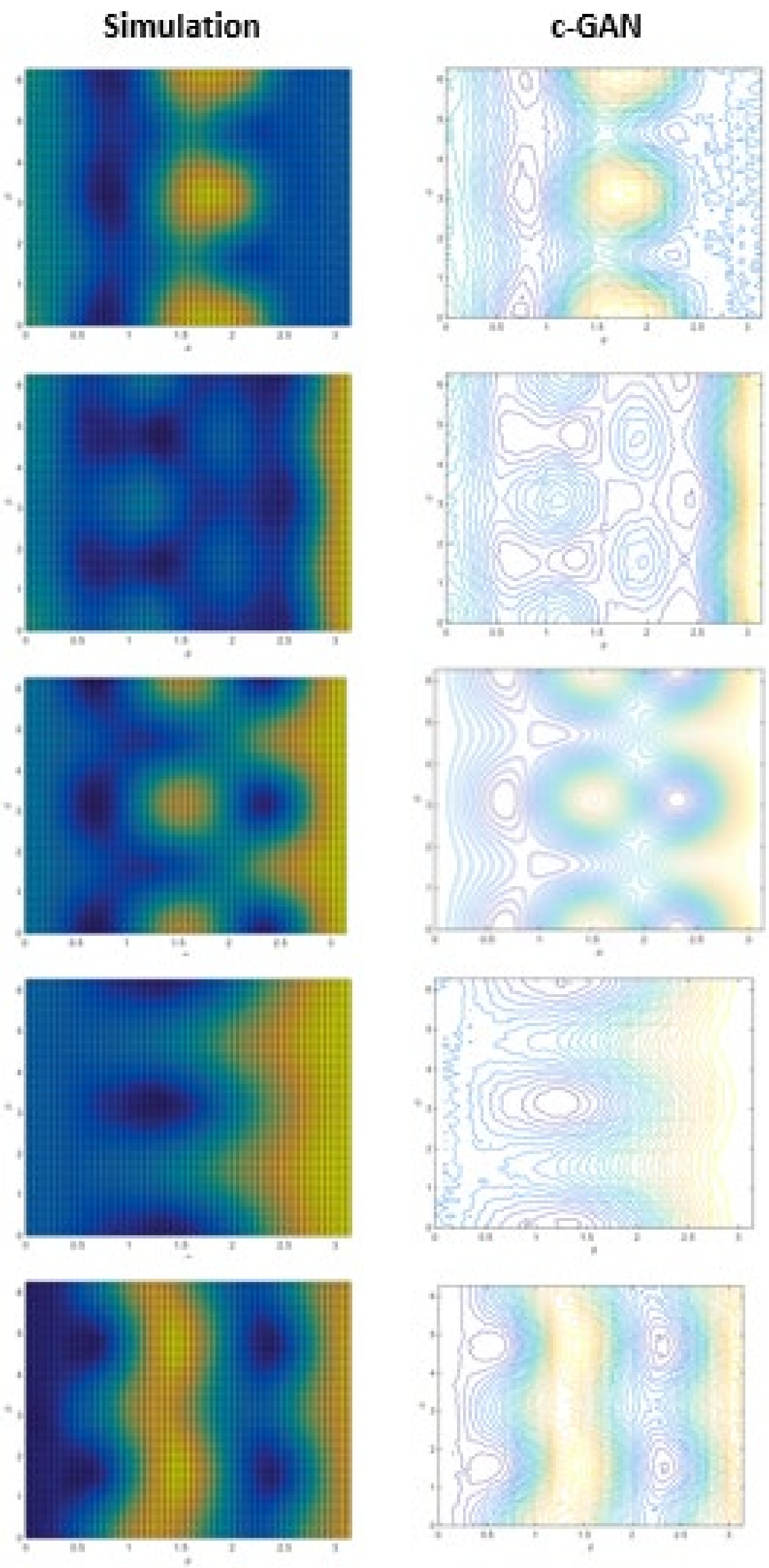

Figure 4-9 The result of radiation pattern restoration. Left: Original patterns generated by the numerical simulation. Right: Restored patterns by the proposed c-GAN model.

4.9. Summary

In this chapter, we proposed a method using the GAN model that can support the tasks of radiation patterns' measurement and enables a fast and accurate evaluation of radiation patterns of different types of antennas. The procedure of the experiment is described and explained in detail. To demonstrate the feasibility, the initial of the dielectric ball scattering experiment is also represented. In the experiment, different GAN network structures have been implemented in order to optimize the structure parameters of the proposed model. The first experiment demonstrates the potential of the proposed GAN model that can generate the radiation patterns similar or nearly the same as real radiation patterns. In addition, the result of the second experiment shows the ability of antenna pattern restoration from the sparse radiation pattern. Though the proposed GAN model still unavoidably produces some noises at low intensity areas, it performs well when recovering the part where mode appears. As a result, we believe that the proposed method is feasible and worthy to further study and apply into 5G telecom and antenna design. Generally speaking, measuring an antenna's radiation pattern and gain is very time-consuming and is limited to specific planes or angles. We expect the proposed model that enable a fast and accurate evaluation of radiation patterns of antennas even placed in realistic environments and can be applied to support the construction of 5G base stations in the future.

5. MACHINE LEARNING-ASSISTED DESIGN OF METASURFACE RADOMES

5.1. Introduction

Nowadays, the growing demand for broad channel bandwidth and high data transmission rate has become an essential topic in modern wireless communication systems and is needed to be developed urgently [92]. As the breakthrough of the 5th generation (5G) technology, bunches of advanced technologies, such as internet of things (IoTs) [89], autonomous driving [90], healthcare and medical applications [91], and smart home technologies [92]. Due to the requirement for incorporating multiple antennas into an equipment, the development of the multiple-input and multiple-output (MIMO) antenna array has got a great concern since it enable both high capacities and high-speed wireless communication [203], hence becomes an extremely popular topic recently.

Though it seems convenient, the design of MIMO systems has several challenges needed to be solved, which includes in-situ performance [116], [117], antenna size [119], and mutual coupling among each antenna [120], [121]. Ideally, 5G antennas are expected to operate at millimeter-wave (mm-Wave) band with good radiation characteristics. However, as the operating frequency increases, the signal will attenuate significantly with propagation distance. In addition, high operating frequency also indicates that the signal is easily interfered by the environment. Therefore, it is required that a 5G MIMO antenna system must be as small as possible in order to install in a limited space. Among all kinds of antennas, Fabry-Perot Cavity (FPC) antenna is a simple but efficient option since it can achieve high gain and high directivity radiation, which enable applications of long-range wireless communications

[86]–[88]. Common FPC antenna consists of a partially reflective surface (PRS) and a metal ground on the top and bottom surface respectively to form a resonant cavity. A source antenna feeds a radiation propagated back and forth inside the cavity, and eventually emits a signal generated by the superposition of all in-phase radiation waves toward PRS's direction, resulting in high gain and high directivity.

However, making the MIMO device smaller also reduce the gap between each antenna element, result in not only high spatial correlation but also strong mutual coupling [120], [121]. A MIMO system usually consists of multiple transmit and receive antennas with different functions and varieties of operating frequency to achieve wide channel capacities. When MIMO antennas send and receive signals from multiple independent channels simultaneously, the narrow space leads tremendously inter-coupling effect induced by surface current flows from excited ports, surface waves, space radiations, or the opposing effect of mutual coupling on reflection coefficients [120], [121], which affects the performance of the wireless system, the efficiency of each antenna element, and the error rate of data transmission. Therefore, how to reduce the mutual coupling among antennas has got a significant concern in MIMO antenna design. Verities of methods has been referred to achieve mutual coupling reduction. Conventional methods such as antennas replacement [123], [204], geometry modification with defected ground structures (DGSs) [122], [124] or parasitic element structures [126], [127] are used to reduce the mutual coupling effect from the surface current flow. In order to reconfigure the MIMO antenna array, numerical simulations and optimization methods, such as partial swarm optimization (PSO) [205], [206], genetic algorithms (GA) [207], and galaxy-based search algorithms (GbSA) [208], [209] are widely used to optimize the geometry configurations and mitigate the mutual coupling effect from digital domain. However, these methods usually lead gain reduction as well. In addition, it is difficult to achieve mutual coupling reduction over broad bandwidth.

In recent years, inserting metamaterials between the antennas, such as decoupling networks [210], neutralization lines [211], [212], and complementary split ring resonators (CSRRs) [142], [143] also become an efficient technique in mutual coupling reduction. Metamaterials are made of artificial structure arrays that enable the permittivity and permeability of the metamaterials to be negative, hence can achieve surface current flow or radiation wave isolation. In addition to metamaterials, metasurfaces are also a potential option [213]–[215]. Metasurfaces are a kind of metamaterials with extremely thin thickness, hence can be considered as a 2-D surface. Comparing to conventional metamaterials, metasurfaces won't change the antenna array structures due to the small size, hance the influence of gain reduction becomes alleviate. Moreover, metasurfaces can not only be inserted at the gap between antennas, but also be an antenna radome on the antennas for port isolation [216].

Recently, machine learning (ML)-assisted algorithms have been greatly concerned and widely applied to many fields. In the field of electromagnetics (EM), one of the most famous applications is the inverse design model [216]. Since the design of EM devices is usually relied on numerical simulation models, the inverse design model is expected to be an effective optimization technique for numerical simulation. It is first pre-trained with the data from simulation software, and then predicts the optimal geometrical configurations by the performance features, such as S-parameters or resonant frequencies, of the design. Comparing to conventional optimization methods such as PSO and GA, ML-assisted models dramatically increase the searching space, hence enable the design with large degree of freedom (DoF) [217], [218], result in the reduction of calculation time and resource. In short, it is suitable for designing the device with complex geometry.

In this chapter, we proposed a ML-assisted method to design an optical transparent metasurface radome that can cover the antenna array and mediate the electromagnetic mutual coupling between antennas. The proposed ML algorithm can automatically synthesize the metasurface radome to tailor reflection, transmission, and absorption of EM waves in a unidirectional or bidirectional manner. The metasurface is composed of a transparent conducting sheet and assembled by the pixel-based bricks. The data for training is generated by random numerical simulations using Ansys HFSS, controlled by a Matlab kernel. The inverse design model is then trained by the dataset loaded with EM information including reflection and transmission spectra and polarization dependencies, so as to produce the optimum metasurface geometry for the specific application. A set of metasurface configurations are inserted back to the numerical simulator to validate the performance of the ML-assisted design tool. Several constraints are made to limit the searching space. Two representative metasurface design examples, including an ultrathin, bidirectional metasurface-absorber (which exhibits high absorption in the entire X-band, and a wide-angle unidirectional metasurface-absorber, are presented to validate the performance of the proposed ML-assisted design model.

5.2. Transparent Metasurface Radomes Based on Pixel-Level Bricks

Optical transparent metasurface radomes that have broad absorption band at specific frequency band while being nearly transparent out of the absorption band can not only be applied in radar stealth technologies [219], [220], but can efficiently reduce the mutual coupling effect from the radiation waves transmitted or received by each antenna in MIMO antenna arrays and have attracted a growing concern in the

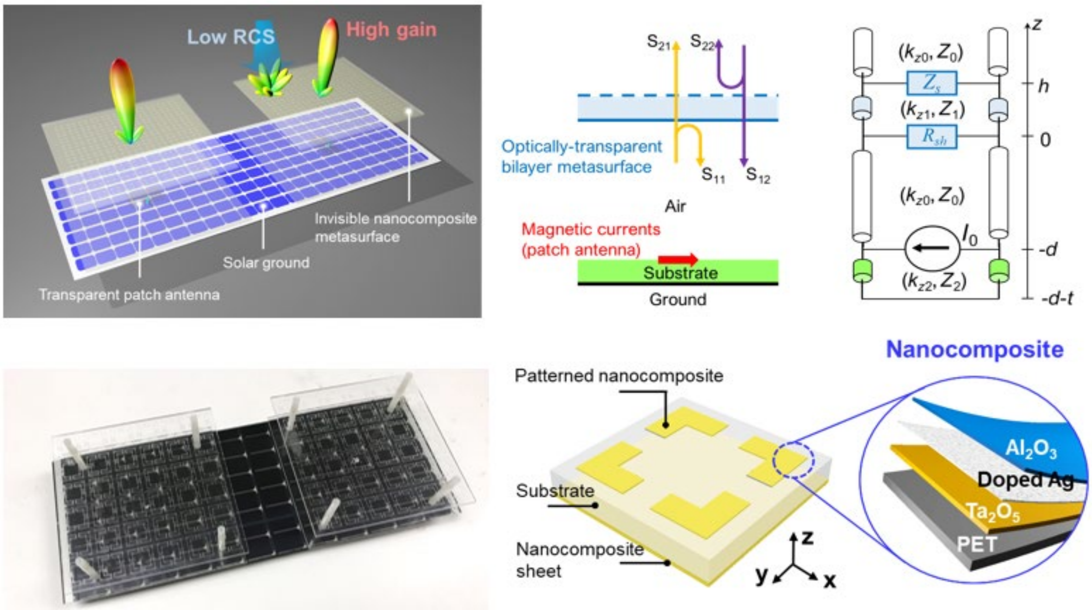

Figure 5-1 The schematic of the transparent metasurface radome from the previous work by Z. Liang and P. Chen [213] in 2021. Their proposed metasurface radome enable physical protection to the transparent patch antenna array integrated with a solar cell ground plane, while keeping high gain and low RCS of the patch antenna array. The metasurface structure is made of a nanocomposite sheet and is transferred to the optical transparent substrate.

construction of 5G telecom infrastructure [219], [220]. In 2021, Z. Liang and P. Chen [216] have proposed an idea that applied a metasurface radome made of conductive nanocomposite materials to physically protect the transparent patch antenna array while keeping high gain and low RCS of the patch antenna array. The schematic of the metasurface radomes by Liang is represented in Fig. **5-1**. Followed by the previous work of Z. Liang, we proposed a new class of inverse design models that can achieve the design of the transparent metasurface radomes using pixel-level bricks that enable broad band, wide-angle absorption at 5G frequency band. In our proposed design, the geometry of the metasurface is built by many pixel-level bricks, as shown in Fig. **5-2**. The gold bricks are made of the composite conductive sheet with the surface resistivity of $3.7\ \Omega/\mathrm{sq}$. The blue bricks represent as the empty space (i.e., without the conductivity sheet). Since the antennas in MIMO systems may transmit or receive different directions of polarization, the proposed metasurface absorber should also

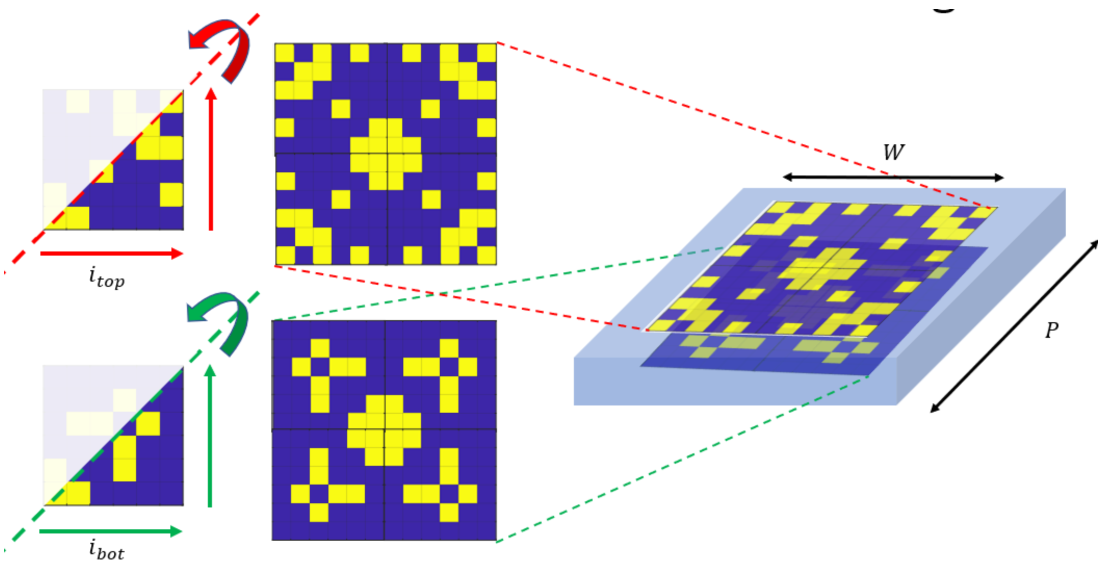

Figure 5-2 The schematic of the design concept of the proposed metasurface radomes. The geometry configurations consist of the spatial indexes of the top and bottom metasurfaces, the width of the designable area for the metasurface structure, and the characteristic length of the unit cell.

adopt unpolarized waves. Hence, the geometry of the entire metasurface must be fully symmetrical. As a result, the design can be confined to a one-eighth triangle area. Here the geometry configurations are saved as a vector consisting of the spatial indexes of each brick on the metasurface. In addition, two set of spatial indexes may be inserted into the configuration vector if the metasurfaces exist on both sides of the radome. Furthermore, to increase the searching space, the characteristic length of each unit cell and the width of the designable area of the metasurface structure also vary and are considered into the geometrical information. Therefore, the geometry configuration vector is described as:

$$\bar{G} = [\bar{\iota_t}, \bar{\iota_b}, W, P]$$

where

$$\bar{\iota_t} = \left[i_t^{(1)}, i_t^{(2)}, \dots, i_t^{(m)}\right]$$

$$\overline{\iota_b} = \left[i_b^{(1)}, i_b^{(2)}, \dots, i_b^{(n)}\right]$$

are the spatial indexes of the top and bottom metasurfaces. And

$$W = [W_1, W_2, \dots, W_{11}]$$

$$P = [P_1, P_2, \dots, P_{11}]$$

are the binary numbers of the width of the designable area and the characteristic length of the unit cell, respectively. In order to feed the vector to the proposed ML-assisted model with an accurate form, $\overline{\iota_t}$ and $\overline{\iota_b}$ are transformed into binary arrays where "0" and "1" imply the empty space and the resistance brick, respectively. For W and P, the precision under decimal is defined to the first digit after decimal point that the first five elements (i.e., $W_1 \sim W_5$ and $P_1 \sim P_5$) describe the integer part, and the next six elements (i.e., $W_6 \sim W_{11}$ and $P_6 \sim P_{11}$) describe the float part of the binary value. Two examples are presented as follows:

$$23.4_{(10)} = 10111.011001_{(2)}$$

$$15.9_{(10)} = 01111.111001_{(2)}$$

5.3. Numerical Simulation Setup

The numerical simulation is used to generate data as more as possible for training the proposed ML-assisted model. We mainly used Ansys HFSS for the data collection step. The concept of the numerical simulation and the finite element method have already been mentioned in Sect. 5.6. In the proposed method, we first randomly generated the geometry configurations using a Matlab kernel and inserted the configurations into the simulation software, and then collected the spectra of all s-parameters of the metasurfaces built by the geometry configurations. The procedure is fully automatic and is controlled by Matlab and visual basic script (VBscript).

5.4. ML-Assisted Inverse Design Model

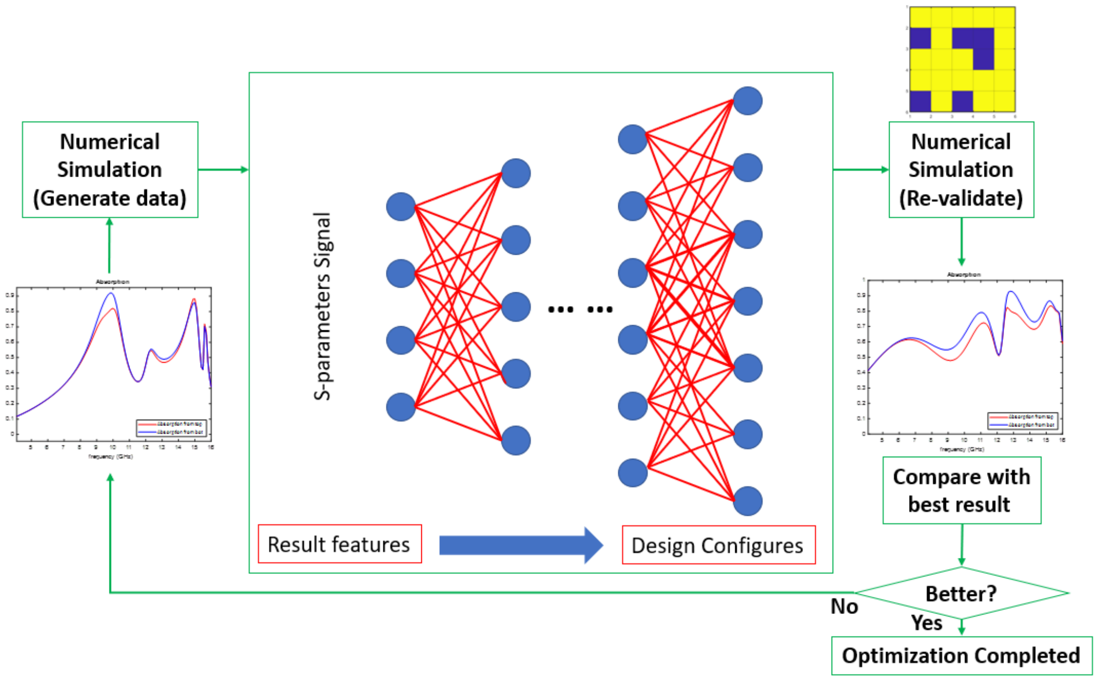

Figure 5-3 The schematic of the proposed inverse design model. The input is the s-parameters of the metasurface evaluated by the simulation software and the output is the corresponding geometry configuration vector. The s-parameters can be either the reflection and transmission or the absorption calculated from the reflection and transmission.

We mainly used the concept of the inverse design model. The schematic of the proposed model is as shown in Fig. **5-3**. In the inverse design model, the input is the s-parameters evaluated by the simulation software and the output is the geometry configuration vector corresponding to the input s-parameters. The s-parameters for the input can be either the transmission and reflection, or the absorption calculated from the transmission and reflection rate. The proposed model can recognize the s-parameters and reconstruct the geometry configuration vector corresponding to the input. The output geometry configuration vector is then transferred back to the decimal values and implemented into the simulation software again in order to validate the performance of the reconstruction ability of the proposed model. The

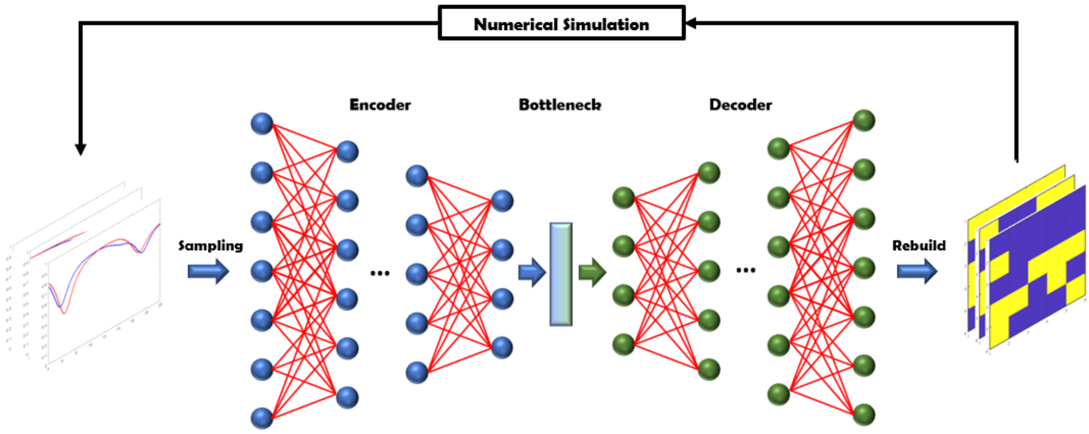

Figure 5-4 The schematic of the proposed auto-encoder-decoder (AED) model. The input s-parameters are first discretized and fed into the encoder. The encoder extracts the latent features and passes the information to the decoder with a non-linear activation function at bottleneck. The decoder then decodes the information and reconstructs the geometry configurations and sends it back to the numerical simulation software to validate the result.

result of each training round is then compared with the best result from the previous round to find the optimal model.

The main part of the proposed model is the neural network (NN) structure that as shown at the middle of Fig. **5-3**. We have tried several types of the NN structures, such as artificial neural networks (ANN) and classical convolutional neural networks (CNN), and have decided to apply the auto-encoder-decoder (AED) network for the proposed model.

5.5. Auto-Encoder-Decoder

The Auto-encoder-decoder (AED) is an unsupervised learning technique that is usually used in data reconstruction [221], [222]. The network can be divided into three phases: the encoder, the bottleneck, and the decoder. The encoder network can compress the input information. In other words, it can extract the key features from the input and represent the features as a short summary. On the other hand, the decoder network can interpret the summary made from the encoder network and attempt to reconstruct the object. Between the two network structures, the bottleneck connects the encoder and the decoder networks with a non-linear activation function. The summary of the original information is flattened and transferred to a vector in this phase and fed to the decoder network. The input and output of the AED can be either 1-D vectors, 2-D arrays, or even higher-dimensional data structures like videos. In addition, it is not limited to have the same dimension between the input and the output. Therefore, AED networks are popular and have been widely used in image reconstruction [223], object or anomaly behavior detection [224], and natural language processing (NLP) [225], [226].

Fig. **5-4** represents the proposed AED-based inverse design model. The input s-parameters are first discretized and fed into the encoder. The encoder extracts the latent features of the input and passes the information to the decoder with a non-linear activation function at bottleneck. The decoder then decodes the information and attempts to reconstruct the geometry configurations. The output is sent back to the numerical simulation software to validate the consistency between the numerical simulation and the proposed model. Based on the trials we have done, we applied only convolution layers to reduce the dimension of the input instead of pooling layers. The convolution layer is set to divide the dimension by 2 or 3 in each layer. In the same vein, the deconvolution layers that can amplify the dimension of the input by 2 or 3 (corresponding to the structure of the encoder) are applied in the decoder. At the output of the decoder, a $\tanh(*)$ function is applied to force the output vector be -1 or 1. Here we don't use the sigmoid function to reach $0/1$ array, since the proposed model is easy to fade out when using the sigmoid function. In addition, it is difficult to find a suitable threshold to regularize the output.

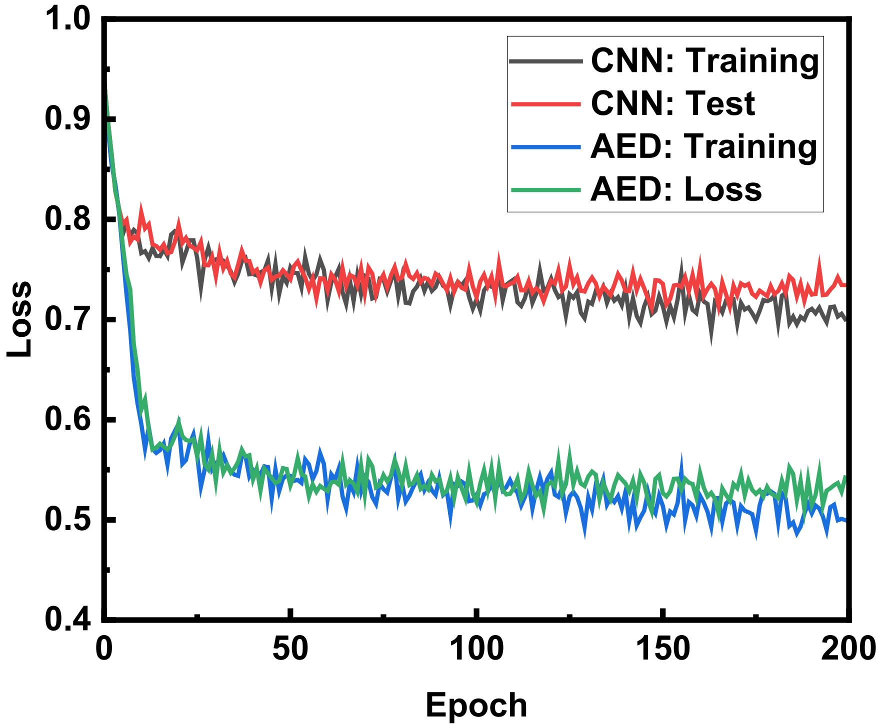

Figure 5-5 The comparison of the training and test MSE losses from the model using the tradition CNN and the proposed AED structures.

Moreover, similar as GAN networks, AED networks is also sensitive to the input so that it is easy to overfit the training data, hence a suitable loss function is crucial for the performance of the proposed model. Based on our verification, the mean square error (MSE) function is applied into the proposed model for backpropagation. In addition, a L1-regularization term is added after the MSE function to prevent overfitting.

To validate the current AED model is the optimal one among other NN structures, we also made a test to compare the performance between the traditional CNN and the proposed AED structures. Fig. **5-5** shows the training and test loss of the model using the traditional CNN and that using the proposed AED structure. It shows that the proposed AED model converges much faster and has lower MSE loss in both training

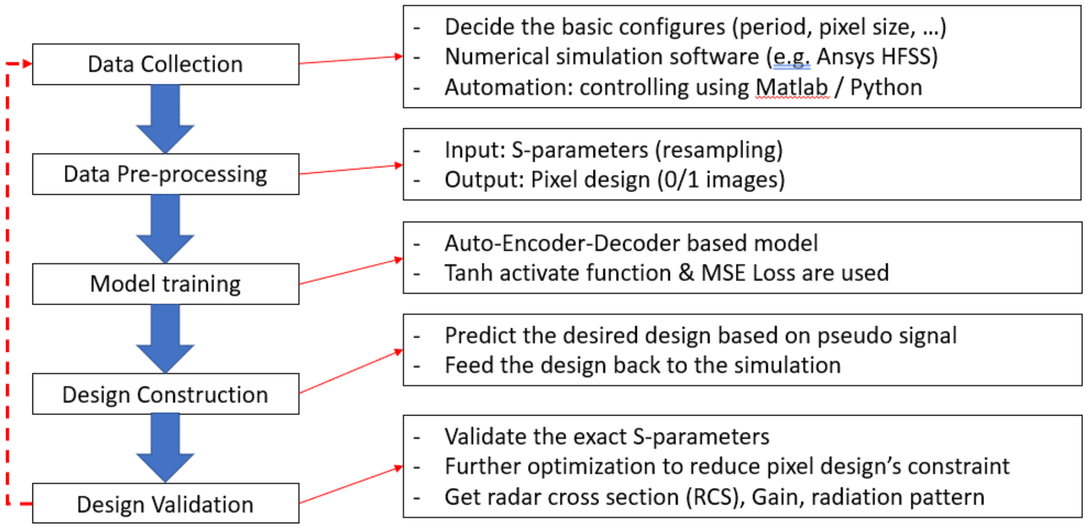

Figure 5-6 The procedure of the experiment for the proposed model. Details of each step is descripted in Sect. 6.6.

and test steps than traditional CNN model, which proves the out-performance of the proposed AED model.

5.6. Procedure

The procedure of the experiment for the proposed AED model is listed and presented in Fig. **5-6**. The geometry configurations are randomly generated and transferred to the binary vector form using the Matlab kernel. The training s-parameters of the corresponding geometry configurations are generated and collected using the numerical simulation software. All the input s-parameters are discretized with a fixed length sampling frequency. Unlike Sect. 5.4, the normalization step is not required since the absorption is calculated by the reflection and transmission rate which are transferred to power, hence it has already been limited to $[0, 1]$.

The proposed ML-assisted model is based on AED, with the loss function of the MSE plus a L1 regularization term and the activation function of $\tanh(*)$ at the output of the decoder network. After the activation function, the elements of the output vector are approaching to -1 or 1. A threshold is set to make the output vector to be a $0/1$ vector, i.e.,

$$\hat{e_i} = \begin{cases} 0\,, e_i < 0 \\ 1\,, e_i \geq 0 \end{cases}$$

where e_i denotes the i^{th} element of the output vector. Then the output vector is interpreted by Matlab and implemented to the numerical simulation software again to validate if the performance is consistent with the numerical simulation result.

When the model is well-trained, a set of pseudo s-parameters which has high absorption at the desired frequency band is fed to the proposed model. The proposed model then provides the corresponding geometry configuration vectors. In fact, the values of the pseudo s-parameters can be critical since the proposed model can be considered as a regression problem which attempts to minimize the loss. The trade-off is that the simulation result of the corresponding geometry configurations may not be fully match, or even be inconsistent when the input condition is too critical to reach the expected values under the geometry constraints set in the beginning. Therefore, the model has to be treated carefully and tried multiple times in order to get the expected result.

For our purpose, the expected frequency band is set at the X-band (i.e., $8 \sim 12$ GHz) of antennas. The expected geometry is set with the constraints as Table **5-1**. In common sense, the resonant frequency is expected to be near the characteristic length of the unit cell in the free space. For the X-band, the center frequency is

TABLE I: THE GEOMETRY CONSTRAINTS FOR THE INPUT OF PROPOSED MODEL

Parameters	P	W	l_{brick}	**Designable area (Num. bricks)**
Min (mm)	12	10	0.8	
Max (mm)	24	P	2	21 (6 × 6)

$10\,\mathrm{GHz}$ so that the wavelength is approximately $30\,\mathrm{mm}$. In addition, due to the limitation of the fabrication process by the laser cutter, the smallest size of a unit brick should be no less than $0.5\,\mathrm{mm}$. Due to the complexity of the proposed design, we set the minimum of the length of a unit brick be $0.8\,\mathrm{mm}$. Another key factor is the number of the bricks. More pixels imply wider searching space. In order to validate the feasibility of the proposed ML-assisted model in a certain way, we define the designable area as a 6×6 right triangle. In other words, the maximum number of bricks is

$$\sum_{n-1}^{6} n = 21$$

and hence the DoF is

$$(2^{21} \times 2) \times 121 \times 141 \approx 71.5 \text{ billions}$$

where the first term is the total number of possible geometries of the $0/1$ pixel-based design on top and bottom surfaces. The second and third terms depict the maximum number of possible P and W, respectively. Therefore, it is large enough to verify the feasibility of the proposed ML-assisted model.

The proposed AED model is implemented using Pytorch API by Python kernels. The environment for the experiment is under Ubuntu 16.04 operating system. The training process is executed by a Intel Core i7-6700HQ CPU with the clock rate of 2.67 GHz, 16 GB DDR4 RAM, and a NVIDIA GTX-960M GPU. The size of the dataset is approximately $30{,}000$, which is much smaller than the DoF. This difference indicates the strong potential of the proposed ML-assisted model.

5.7. Results and Discussion

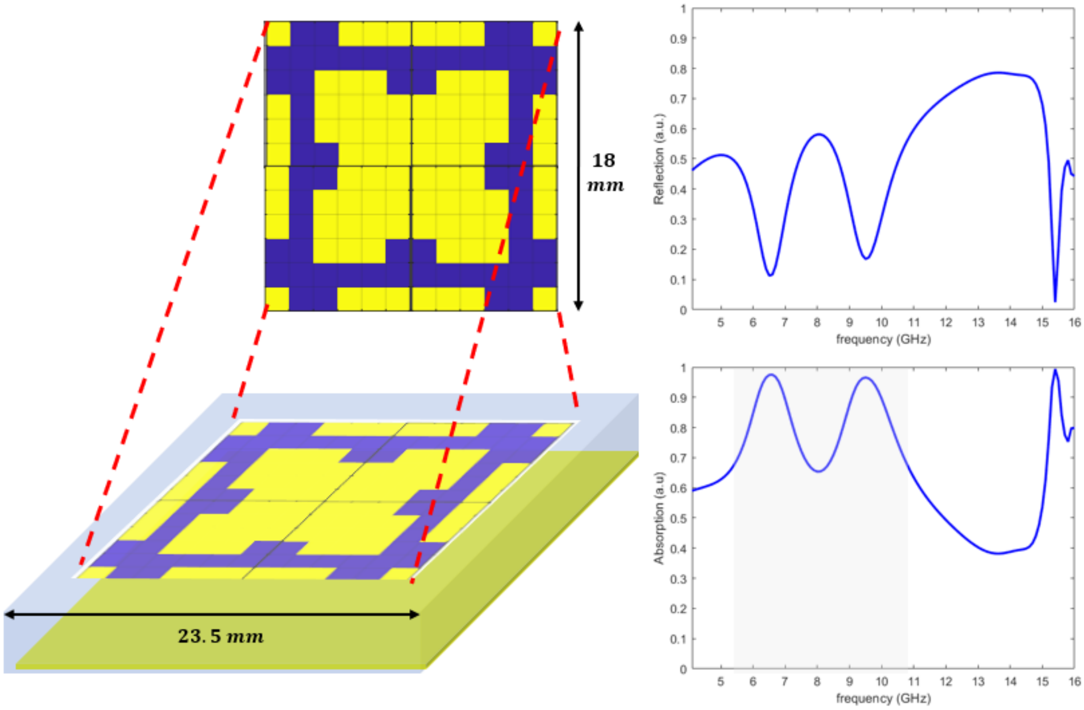

Figure 5-7 The result of the proposed ML-assisted model applied in the design of unidirectional absorber. The gray region in the s-parameters plot shows a dual band absorber nearly X-band.

We present three experiment to show the feasibility and performance of the proposed ML-assisted model.

(a) Unidirectional Absorber

The first experiment is a unidirectional absorber which has high absorption on one side and fully reflection on the other side. Since the fully reflection can be simply achieved by a ground plane, only the s-parameters on one side are required for model training. Hence, we present this example as an initial trial for the proposed model. A sample of the design from the proposed well-trained model are shown in Fig. **5-7**. The s-parameters plot in Fig. **5-7** shows a dual band absorber at the frequency band near the X-band. The width of the designable area is $18\,\mathrm{mm}$ or $1.5\,\mathrm{mm}$ width per unit brick, which is above the minimum size of the fabrication process. The characteristic length is $23.5\,\mathrm{mm}$ which is close to $30\,\mathrm{mm}$ that matches our initial assumption. It is noticed that the result may not be totally the same as the pseudo s-parameters. However, the proposed model will attempt to find a case that matches the desired design as close as possible.

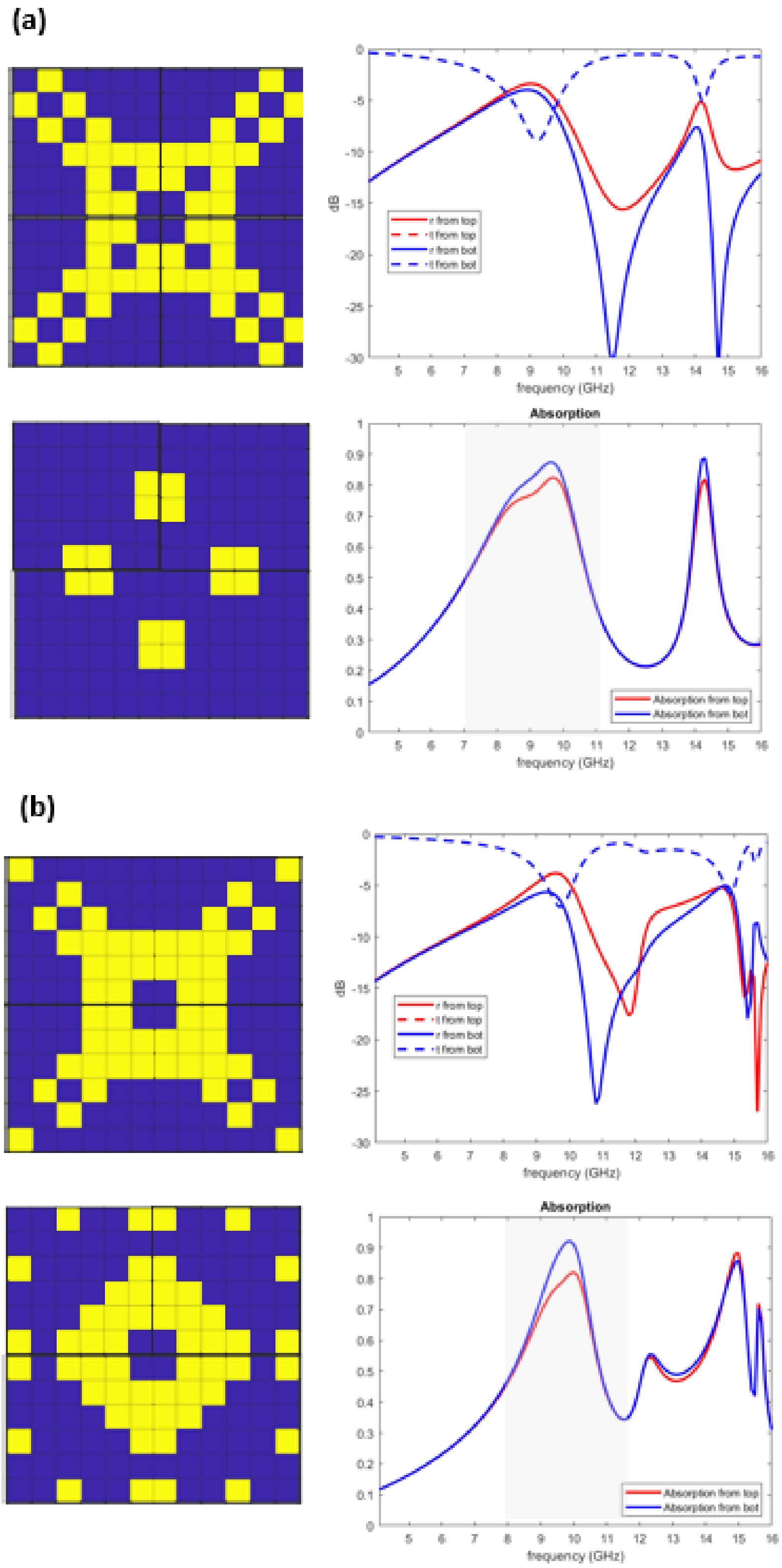

Figure 5-8 The result of the proposed ML-assisted model applied in the design of bidirectional absorber. The geometry plots denote the designed metasurfaces on the top (top-left) and bottom (bottom-left) surfaces. The grey area in the s-parameters plot denotes the high absorption frequency band of the radome.

(b) Bidirectional Absorber

The second experiment is to design a broad band bidirectional absorber radome which is the main application of the proposed method. The input is the absorption rate from two sides. Two samples generated by the proposed ML-assisted model are presented in Fig. **5-8**. The left-side of each sample display the metasurfaces on the top and bottom sides generated from the proposed ML-assisted model. The right-side plots show the transmission and the reflection in dB, and the corresponding absorption rate. According to the plots, it shows that both designs reach a broad band, high absorption rate around $8\ \mathrm{GHz}$ to $12\ \mathrm{GHz}$, as the gray regions label in the plots. It is noticed that some unexpected high absorption peaks appeared at high frequencies. It is due to the complexity of the EM model. When adding or removing a brick, the change of the behavior of the surface current flow is not linear. Though the AED model can reach the expected performance at the frequency it focuses on, it may also lead unexpected behavior out of the focus frequency band. However, it is not an issue for our purpose, since the main idea is to create a metasurface with broad band absorption rate that can absorb extra radiation wave and hence reduce the mutual coupling effect.

(c) Wide-angle Unidirectional Absorber

The last experiment is to validate if the proposed ML-assisted model can reach high absorption rate even with large incident angle. It is also a crucial factor since the radiation waves at the large incident or emitted angle are one of the main reason for mutual coupling. However, the size of the input data has a dramatic increment since the s-parameters at all angles have to be taken into account, which sharply raise the complexity of the proposed model. In order to reduce the DoF, the experiment is limited to a unidirectional absorption problem. In addition, the s-parameters are

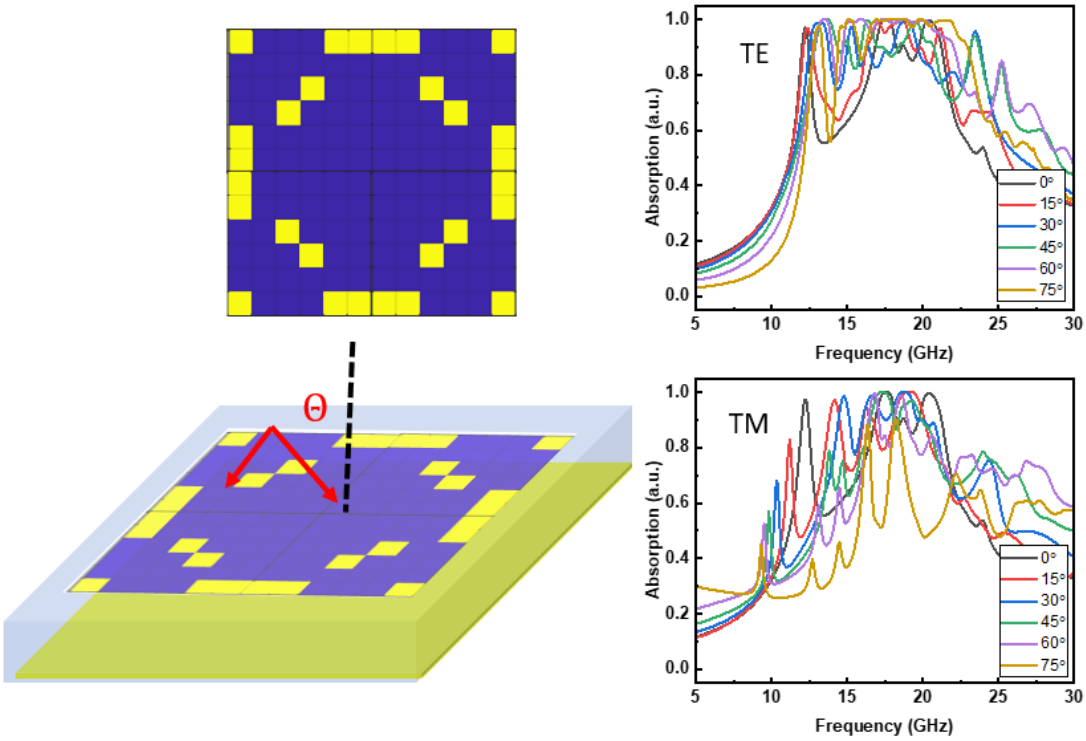

Figure 5-9 The result of the proposed ML-assisted model applied in the design of a broad band, wide-angle bidirectional absorber. The geometry plot denotes the designed metasurface on the top surface.

evaluated every 15^o from $0^o \sim 75^o$ and reshaped as a 2-D array of six signals. An example generated from the proposed AED model is shown in Fig. **5-9**. It shows that the generated design enables a broad band high absorption peak around $15\ \mathrm{GHz}$ to $20\ \mathrm{GHz}$ with the incident angle from 0^o to 75^o when in TE mode and the incident angle from 0^o to 60^o when in TM mode. Though the absorption rate slightly decreases at 75^o incident angle in TE mode, the performance is well enough to be applied to the MIMO radome for mutual coupling reduction.

5.8. Summary

In this chapter, we proposed a ML-assisted model based on AED that can design the metasurface radomes composed of a transparent conducting sheet and assembled by the pixel-based bricks that enable mutual coupling reduction to MIMO antenna arrays. With different kinds of the input data, the proposed model can provide the design of radomes with multiple usages. Three representative metasurface design examples, including an ultrathin, bidirectional metasurface-absorber which exhibits high absorption in the entire X-band, and a wide-angle unidirectional metasurface-absorber, are presented to validate the proposed ML-assisted design model. The results of the three experiments show that the proposed ML-assisted inverse design model has the potential in complex metasurface design. Due to the complexity of EM behaviors, the input s-parameters may not be completely the same as the simulation result of the corresponding geometry configurations when at the frequencies out of the proposed frequency band. However, the s-parameters match well at the frequencies nearly the proposed frequency band. In addition, the spectra of the s-parameters can be modified by scaling the size of the characteristic length and the designable area. Furthermore, the proposed model can be applied to design circular polarization converters or eliminator with the similar methodology as that mentioned in this chapter.

6. CONCLUSION AND FUTURE WORK

In this thesis, we proposed the ML-assisted methodology for couple EM applications. Chapter 3 presented a theoretical model that can analyze all the dominant powers of scattering, absorption, and extinction modes and represent as a general power diagram using energy functions related to scattering and absorption and math techniques such as differential calculus and Lagrange multiplier. According to the power diagrams shown in Sect. 3.4, there is a clear boundary between absorption, scattering, and extinction. The region of a system with higher partial modes can completely cover a system with lower modes. Therefore, it can properly induce higher scattering modes to simulate the same power distribution in lower ones, which represents the degeneracy of light scattering in absorption, scattering, and extinction.

The study of Chapter 3 shows that EM problems can be solved theoretically under specific constraints. However, when the complexity becomes higher, analytical solutions are sometimes hard to get an exact solution or be suitable for all practical cases. In addition, although the numerical simulation is an efficient method to substitute the exact solution, it is still very time-consuming when solving high DoF problems. Hence, in Chapter 4 and 5, we presented a different kind of method that can solve and optimize two EM problems with high DoF using ML-assisted models.

Chapter 4 presented a ML-assisted method using the GAN model that can support the tasks of radiation patterns' measurement and enables a fast and accurate evaluation of radiation patterns of different types of antennas. Different GAN network structures have been implemented and tested to optimize the proposed model. The first experiment demonstrates the potential of the proposed GAN model that can generate the radiation patterns similar or nearly the same as real radiation patterns. In addition, the result of the second experiment shows the ability of antenna pattern restoration from the sparse radiation pattern.

Chapter 5 presented a ML-assisted model based on the AED that can design the metasurface radomes composed of a transparent conducting sheet and assembled by the pixel-based bricks that enable mutual coupling reduction to MIMO antenna arrays. With different kinds of the input, the proposed model can provide the corresponding design of radomes with multiple usages. Three representative metasurface design examples, including an ultrathin, bidirectional metasurface-absorber which exhibits high absorption in the entire X-band, and a wide-angle unidirectional metasurface-absorber, are presented to validate the proposed ML-assisted design model. The results show that the proposed ML-assisted inverse design model has the potential in complex metasurface design. In addition, the operating frequency can be modified by scaling the size of the characteristic length and the designable area.

ML and NN have been extremely popular recently. Many previous works and products show the strong potential of ML and NN in making technologies more advanced. In the same vein, Chapter 4 and 5 demonstrate that ML-assisted models can also be well applied to EM problems. In the future, there is a need to investigate more applications of the ML-assisted model in EM topics. In addition, the investigation for eliminating small disturbance from NN structures is also needed.

Furthermore, the future works include the investigation of the radiation pattern measurement in a real noisy environment, the metasurface design with different basis such as the triangle and hexagon, and the metasurface design for circular polarization converters or suppressors.

APPENDIX

The approval of citation of the content in *Chapter 3*:

CCC RightsLink

Help ∨ Email Support

Degeneracy of light scattering and absorption by a single nanowire

SPRINGER NATURE

Author: Jeng Yi Lee et al

Publication: Scientific Reports

Publisher: Springer Nature

Date: Sep 20, 2021

Creative Commons

You are not required to obtain permission to reuse this article.

To request permission for a type of use not listed, please contact Springer Nature

The approval of the reuse of Fig. **5-1** in <u>*Sect. 5-2*</u>:

CCC | RightsLink

Home | Help | Live Chat | Sign in | Create Account

IEEE Requesting permission to reuse content from an IEEE publication

A Low-RCS and Low-ECC Transparent Meta-Radomes Based on a Conductive Nanocomposite

Conference Proceedings: 2021 IEEE International Symposium on Antennas and Propagation and USNC-URSI Radio Science Meeting (APS/URSI)

Author: Liang Zhu

Publisher: IEEE

Date: 04 December 2021

Copyright © 2021, IEEE

Thesis / Dissertation Reuse

The IEEE does not require individuals working on a thesis to obtain a formal reuse license, however, you may print out this statement to be used as a permission grant:

Requirements to be followed when using any portion (e.g., figure, graph, table, or textual material) of an IEEE copyrighted paper in a thesis:

1) In the case of textual material (e.g., using short quotes or referring to the work within these papers) users must give full credit to the original source (author, paper, publication) followed by the IEEE copyright line © 2011 IEEE.
2) In the case of illustrations or tabular material, we require that the copyright line © [Year of original publication] IEEE appear prominently with each reprinted figure and/or table.
3) If a substantial portion of the original paper is to be used, and if you are not the senior author, also obtain the senior author's approval.

Requirements to be followed when using an entire IEEE copyrighted paper in a thesis:

1) The following IEEE copyright/ credit notice should be placed prominently in the references: © [year of original publication] IEEE. Reprinted, with permission, from [author names, paper title, IEEE publication title, and month/year of publication]
2) Only the accepted version of an IEEE copyrighted paper can be used when posting the paper or your thesis on-line.
3) In placing the thesis on the author's university website, please display the following message in a prominent place on the website: In reference to IEEE copyrighted material which is used with permission in this thesis, the IEEE does not endorse any of [university/educational entity's name goes here]'s products or services. Internal or personal use of this material is permitted. If interested in reprinting/republishing IEEE copyrighted material for advertising or promotional purposes or for creating new collective works for resale or redistribution, please go to http://www.ieee.org/publications_standards/publications/rights/rights_link.html to learn how to obtain a License from RightsLink.

If applicable, University Microfilms and/or ProQuest Library, or the Archives of Canada may supply single copies of the dissertation.

BACK | CLOSE WINDOW

CITED LITERATURE

[1] F. Andriulli, P. Y. Chen, D. Erricolo, and J. M. Jin, "Guest Editorial Machine Learning in Antenna Design," in IEEE Transactions *on Antennas and Propagation, vol. 70, no. 7, pp. 4948-4952*, Jul. 2022. doi: 10.1109/TAP.2022.3189963.

[2] M. Malmstrom, I. Skog, S. M. Razavi, Y. Zhao, and F. Gunnarsson, "5G positioning - A machine learning approach," in *2019 16th Workshop on Positioning, Navigation and Communication, WPNC 2019*, Oct. 2019. doi: 10.1109/WPNC47567.2019.8970186.

[3] M. R. Naeini and M. Fakharzadeh, "A 28 GHz beam-switching yagi-uda array using rotman lens for 5g wireless communications," in *2017 IEEE Antennas and Propagation Society International Symposium, Proceedings*, Oct. 2017, vol. 2017-January, pp. 2617–2618. doi: 10.1109/APUSNCURSINRSM.2017.8073351.

[4] Q. Hua *et al.*, "A Novel Compact Quadruple-Band Indoor Base Station Antenna for 2G/3G/4G/5G Systems," *IEEE Access*, vol. 7, pp. 151350–151358, 2019, doi: 10.1109/ACCESS.2019.2947778.

[5] K. Kim, J. Lee, and J. Choi, "Deep Learning Based Pilot Allocation Scheme (DL-PAS) for 5G Massive MIMO System," *IEEE Commun. Lett.*, vol. 22, no. 4, pp. 828–831, Apr.2018, doi: 10.1109/LCOMM.2018.2803054.

[6] N. Ojaroudiparchin, M. Shen, and G. F. Pedersen, "Multi-layer 5G mobile phone antenna for multi-user MIMO communications," in *2015 23rd Telecommunications Forum, TELFOR 2015*, Jan. 2016, pp. 559–562. doi: 10.1109/TELFOR.2015.7377529.

[7] E. H. Mujammami and A. B. Sebak, "Wideband High Gain Printed Quasi-Yagi Diffraction Gratings-Based Antenna for 5G Applications," *IEEE Access*, vol. 7, pp. 18089–18100, 2019, doi: 10.1109/ACCESS.2019.2897092.

[8] A. Zhao and Z. Ren, "Size Reduction of Self-Isolated MIMO Antenna System for 5G Mobile Phone Applications," *IEEE Antennas Wirel. Propag. Lett.*, vol. 18, no. 1, pp. 152–156, Jan.2019, doi: 10.1109/LAWP.2018.2883428.

CITED LITERATURE (Continued)

[9] H. C. Huang, “Overview of antenna designs and considerations in 5G cellular phones,” in *2018 IEEE International Workshop on Antenna Technology, iWAT2018 - Proceedings*, Jun. 2018, pp. 1–4. doi: 10.1109/IWAT.2018.8379253.

[10] M. Shafi *et al.*, “5G: A tutorial overview of standards, trials, challenges, deployment, and practice,” *IEEE J. Sel. Areas Commun.*, vol. 35, no. 6, pp. 1201–1221, Jun.2017, doi: 10.1109/JSAC.2017.2692307.

[11] W. Hong, K. H. Baek, Y. Lee, Y. Kim, and S. T. Ko, “Study and prototyping of practically large-scale mmWave antenna systems for 5G cellular devices,” *IEEE Commun. Mag.*, vol. 52, no. 9, pp. 63–69, Sep.2014, doi: 10.1109/MCOM.2014.6894454.

[12] Y. Zeng, Q. Wu, and R. Zhang, “Accessing from the Sky: A Tutorial on UAV Communications for 5G and beyond,” *Proc. IEEE*, vol. 107, no. 12, pp. 2327–2375, Dec.2019, doi: 10.1109/JPROC.2019.2952892.

[13] Y. Huo, F. Lu, F. Wu, and X. Dong, “Multi-beam multi-stream communications for 5G and beyond mobile user equipment and UAV proof of concept designs,” in *IEEE Vehicular Technology Conference*, Sep. 2019, vol. 2019-September. doi: 10.1109/VTCFall.2019.8891154.

[14] B. Li, Z. Fei, and Y. Zhang, “UAV communications for 5G and beyond: Recent advances and future trends,” *IEEE Internet Things J.*, vol. 6, no. 2, pp. 2241–2263, Apr.2019, doi: 10.1109/JIOT.2018.2887086.

[15] A. Salari and D. Erricolo, “Unmanned Aerial Vehicles for High-Frequency Measurements: An accurate, fast, and cost-effective technology,” *IEEE Antennas Propag. Mag.*, vol. 64, no. 1, pp. 39–49, Feb.2022, doi: 10.1109/MAP.2021.3061026.

[16] H. Zhang, Y. Song, C. Han, and L. Zhang, “Remote Sensing Image Spatiotemporal Fusion Using a Generative Adversarial Network,” *IEEE Trans. Geosci. Remote Sens.*, pp. 1–14, Aug.2020, doi: 10.1109/tgrs.2020.3010530.

CITED LITERATURE (Continued)

[17] Q. Wang, H. Fan, G. Sun, W. Ren, and Y. Tang, "Recurrent Generative Adversarial Network for Face Completion," *IEEE Trans. Multimed.*, pp. 1–1, Mar.2020, doi: 10.1109/tmm.2020.2978633.

[18] W. Ma, Z. Pan, J. Guo, and B. Lei, "Super-resolution of remote sensing images based on transferred generative adversarial network," in *International Geoscience and Remote Sensing Symposium (IGARSS)*, Oct. 2018, vol. 2018-July, pp. 1148–1151. doi: 10.1109/IGARSS.2018.8517442.

[19] Y. Kim, "Application of Machine Learning to Antenna Design and Radar Signal Processing: A Review," in 2018 International Symposium on Antennas and Propagation (ISAP), Oct. 2018, pp. 1-2.

[20] L. Boldrini, J. E. Bibault, C. Masciocchi, Y. Shen, and M. I. Bittner, "Deep Learning: A Review for the Radiation Oncologist," *Front. Oncol.*, vol. 9, p. 977, Oct.2019, doi: 10.3389/fonc.2019.00977.

[21] T. Tang, T. Hong, C. Liu, W. Zhao, and M. Kadoch, "Design of 5G dual-antenna passive repeater based on machine learning," in *2019 15th International Wireless Communications and Mobile Computing Conference, IWCMC 2019*, Jun. 2019, pp. 1907–1912. doi: 10.1109/IWCMC.2019.8766614.

[22] J. Huang *et al.*, "A big data enabled channel model for 5G wireless communication systems," arXiv, Feb. 28, 2020. doi: 10.1109/tbdata.2018.2884489.

[23] T. Wang, S. Wang, and Z. H. Zhou, "Machine learning for 5G and beyond: From model-based to data-driven mobile wireless networks," in China Communications, vol. 16, no. 1, pp. 165-175, Jan. 2019, doi: 10.12676/j.cc.2019.01.015.

[24] D. A. Awan, R. L. G. Cavalcante, M. Yukawa, and S. Stanczak, "Detection for 5G-NOMA: An online adaptive machine learning approach," in *IEEE International Conference on Communications*, Jul. 2018, vol. 2018-May. doi: 10.1109/ICC.2018.8422449.

CITED LITERATURE (Continued)

[25] Y. Yang, Y. Li, W. Zhang, F. Qin, P. Zhu, and C. X. Wang, "Generative-Adversarial-Network-Based Wireless Channel Modeling: Challenges and Opportunities," *IEEE Commun. Mag.*, vol. 57, no. 3, pp. 22–27, Mar.2019, doi: 10.1109/MCOM.2019.1800635.

[26] T. Maksymyuk, J. Gazda, O. Yaremko, and D. Nevinskiy, "Deep learning based massive MIMO beamforming for 5G mobile network," in *Proceedings of the 2018 IEEE 4th International Symposium on Wireless Systems within the International Conferences on Intelligent Data Acquisition and Advanced Computing Systems, IDAACS-SWS 2018*, Nov. 2018, pp. 241–244. doi: 10.1109/IDAACS-SWS.2018.8525802.

[27] D. Erricolo *et al.*, "Machine learning in electromagnetics: A review and some perspectives for future research," in *Proceedings of the 2019 21st International Conference on Electromagnetics in Advanced Applications, ICEAA 2019*, Sep. 2019, pp. 1377–1380. doi: 10.1109/ICEAA.2019.8879110.

[28] J. A. Hodge, K. V. Mishra, and A. I. Zaghloul, "RF Metasurface Array Design Using Deep Convolutional Generative Adversarial Networks," in *IEEE International Symposium on Phased Array Systems and Technology*, Oct. 2019, vol. 2019-October. doi: 10.1109/PAST43306.2019.9020794.

[29] R. Colella, F. P. Chietera, and L. Catarinucci, "Yagi-Uda Antenna with Fully 3D-Printed Bow-Tie Elements," in 2020 IEEE Microwave Theory and Techniques in Wireless Communications (MTTW), Nov. 2020, pp. 62–66. doi: 10.1109/mttw51045.2020.9245029.

[30] N. O. Parchin, R. A. Abd-Alhameed, Y. Li, M. H. Nielsen, and M. Shen, "High-Performance Yagi-Uda Antenna Array for 28 GHz Mobile Communications," in *27th Telecommunications Forum, TELFOR 2019*, Nov. 2019. doi: 10.1109/TELFOR48224.2019.8971142.

[31] Y. W. Hsu, T. C. Huang, H. S. Lin, and Y. C. Lin, "Dual-Polarized Quasi Yagi-Uda Antennas with Endfire Radiation for Millimeter-Wave MIMO Terminals," *IEEE Trans. Antennas Propag.*, vol. 65, no. 12, pp. 6282–6289, Dec.2017, doi: 10.1109/TAP.2017.2734238.

CITED LITERATURE (Continued)

[32] F. T. Celik and K. Karacuhha, “Dual - Band Microtrip Quasi - Yagi Antenna Design for Free Band and 5G Mobile Communication,” in *Proceedings of International Seminar/Workshop on Direct and Inverse Problems of Electromagnetic and Acoustic Wave Theory, DIPED*, Nov. 2018, vol. 2018-September, pp. 189–192. doi: 10.1109/DIPED.2018.8543132.

[33] T. C. Huang, Y. W. Hsu, and Y. C. Lin, “End-fire Quasi-Yagi antennas with pattern diversity on LTCC technology for 5G mobile communications,” in *RFIT 2016 - 2016 IEEE International Symposium on Radio-Frequency Integration Technology*, Sep. 2016. doi: 10.1109/RFIT.2016.7578205.

[34] R. Hussain, A. T. Alreshaid, S. K. Podilchak, and M. S. Sharawi, “Compact 4G MIMO antenna integrated with a 5G array for current and future mobile handsets,” *IET Microwaves, Antennas Propag.*, vol. 11, no. 2, pp. 271–279, Jan.2017, doi: 10.1049/iet-map.2016.0738.

[35] Y. Li, C. Y. D. Sim, Y. Luo, and G. Yang, “12-Port 5G Massive MIMO Antenna Array in Sub-6GHz Mobile Handset for LTE Bands 42/43/46 Applications,” *IEEE Access*, vol. 6, pp. 344–354, Oct.2017, doi: 10.1109/ACCESS.2017.2763161.

[36] Y. H. Chen, A. H. Twing, D. Badawi, J. Danavi, M. McCauley, and A. E. Cetin, “Atrial Fibrillation Risk Prediction from Electrocardiogram and Related Health Data with Deep Neural Network,” in *ICASSP, IEEE International Conference on Acoustics, Speech and Signal Processing - Proceedings*, May 2020, vol. 2020-May, pp. 1269–1273. doi: 10.1109/ICASSP40776.2020.9054403.

[37] M. Wernick, Y. Yang, J. Brankov, G. Yourganov, and S. Strother, “Machine learning in medical imaging,” in *IEEE Signal Processing Magazine*, 2010, vol. 27, no. 4, pp. 25–38. doi: 10.1109/MSP.2010.936730.

[38] G. D. Magoulas and A. Prentza, “Machine learning in medical applications,” in *Lecture Notes in Computer Science (including subseries Lecture Notes in Artificial Intelligence and Lecture Notes in Bioinformatics)*, 2001, vol. 2049 LNAI, pp. 300–307. doi: 10.1007/3-540-44673-7_19.

CITED LITERATURE (Continued)

[39] J. Lemley, S. Bazrafkan, and P. Corcoran, "Deep Learning for Consumer Devices and Services: Pushing the limits for machine learning, artificial intelligence, and computer vision.," *IEEE Consum. Electron. Mag.*, vol. 6, no. 2, pp. 48–56, Apr.2017, doi: 10.1109/MCE.2016.2640698.

[40] H. C. Shin *et al.*, "Deep Convolutional Neural Networks for Computer-Aided Detection: CNN Architectures, Dataset Characteristics and Transfer Learning," *IEEE Trans. Med. Imaging*, vol. 35, no. 5, pp. 1285–1298, May2016, doi: 10.1109/TMI.2016.2528162.

[41] N. D. Sidiropoulos, L. DeLathauwer, X. Fu, K. Huang, E. E. Papalexakis, and C. Faloutsos, "Tensor Decomposition for Signal Processing and Machine Learning," *IEEE Trans. Signal Process.*, vol. 65, no. 13, pp. 3551–3582, Jul.2017, doi: 10.1109/TSP.2017.2690524.

[42] S. Kolouri, S. R. Park, M. Thorpe, D. Slepcev, and G. K. Rohde, "Optimal Mass Transport: Signal processing and machine-learning applications," *IEEE Signal Process. Mag.*, vol. 34, no. 4, pp. 43–59, Jul.2017, doi: 10.1109/MSP.2017.2695801.

[43] O. Simeone, "A Very Brief Introduction to Machine Learning with Applications to Communication Systems," *IEEE Trans. Cogn. Commun. Netw.*, vol. 4, no. 4, pp. 648–664, Dec.2018, doi: 10.1109/TCCN.2018.2881442.

[44] G. Zhu, D. Liu, Y. Du, C. You, J. Zhang, and K. Huang, "Toward an Intelligent Edge: Wireless Communication Meets Machine Learning," *IEEE Commun. Mag.*, vol. 58, no. 1, pp. 19–25, Jan.2020, doi: 10.1109/MCOM.001.1900103.

[45] G. Hinton, S. Osindero, M. Welling, and Y. W. Teh, "Unsupervised Discovery of Nonlinear Structure Using Contrastive Backpropagation," *Cogn. Sci.*, vol. 30, no. 4, pp. 725–731, Jul.2006, doi: 10.1207/s15516709cog0000_76.

[46] K. Fukushima, "A Neural Network for Visual Pattern Recognition," *Computer (Long. Beach. Calif).*, vol. 21, no. 3, pp. 65–75, 1988, doi: 10.1109/2.32.

CITED LITERATURE (Continued)

[47] G. A. Carpenter, “Neural network models for pattern recognition and associative memory,” *Neural Networks*, vol. 2, no. 4. Pergamon, pp. 243–257, Jan.01, 1989. doi: 10.1016/0893-6080(89)90035-X.

[48] J. BROMLEY *et al.*, “SIGNATURE VERIFICATION USING A ‘SIAMESE’ TIME DELAY NEURAL NETWORK,” *Int. J. Pattern Recognit. Artif. Intell.*, vol. 07, no. 04, pp. 669–688, Aug.1993, doi: 10.1142/s0218001493000339.

[49] L. Deng, G. Hinton, and B. Kingsbury, “New types of deep neural network learning for speech recognition and related applications: An overview,” in *ICASSP, IEEE International Conference on Acoustics, Speech and Signal Processing - Proceedings*, Oct. 2013, pp. 8599–8603. doi: 10.1109/ICASSP.2013.6639344.

[50] Y. Zhao, X. Jin, and X. Hu, “Recurrent convolutional neural network for speech processing,” in *ICASSP, IEEE International Conference on Acoustics, Speech and Signal Processing - Proceedings*, Jun. 2017, pp. 5300–5304. doi: 10.1109/ICASSP.2017.7953168.

[51] J. Deng, W. Dong, R. Socher, L. J. Li, K. Li, and F. F. Li, “ImageNet: A large-scale hierarchical image database,” in 2009 IEEE Conference on Computer Vision and Pattern Recognition, Mar. 2009, pp. 248–255. doi: 10.1109/cvpr.2009.5206848.

[52] C. Alippi, S. Disabato, and M. Roveri, “Moving Convolutional Neural Networks to Embedded Systems: The AlexNet and VGG-16 Case,” in *Proceedings - 17th ACM/IEEE International Conference on Information Processing in Sensor Networks, IPSN 2018*, Oct. 2018, pp. 212–223. doi: 10.1109/IPSN.2018.00049.

[53] M. Al-Qizwini, I. Barjasteh, H. Al-Qassab, and H. Radha, “Deep learning algorithm for autonomous driving using GoogLeNet,” in *IEEE Intelligent Vehicles Symposium, Proceedings*, Jul. 2017, pp. 89–96. doi: 10.1109/IVS.2017.7995703.

CITED LITERATURE (Continued)

[54] Z. Zhong, L. Jin, and Z. Xie, “High performance offline handwritten Chinese character recognition using GoogLeNet and directional feature maps,” in *Proceedings of the International Conference on Document Analysis and Recognition, ICDAR*, Nov. 2015, vol. 2015-November, pp. 846–850. doi: 10.1109/ICDAR.2015.7333881.

[55] Z. Lu, X. Jiang, and A. Kot, “Deep Coupled ResNet for Low-Resolution Face Recognition,” *IEEE Signal Process. Lett.*, vol. 25, no. 4, pp. 526–530, Apr.2018, doi: 10.1109/LSP.2018.2810121.

[56] F. N. Iandola, S. Han, M. W. Moskewicz, K. Ashraf, W. J. Dally, and K. Keutzer, “SqueezeNet: AlexNet-level accuracy with 50x fewer parameters and <0.5MB model size,” arXiv., Feb. 2016, Accessed: Dec.13, 2020. [Online]. Available: http://arxiv.org/abs/1602.07360

[57] D. Cheng, G. Meng, G. Cheng, and C. Pan, “SeNet: Structured Edge Network for Sea-Land Segmentation,” *IEEE Geosci. Remote Sens. Lett.*, vol. 14, no. 2, pp. 247–251, Feb.2017, doi: 10.1109/LGRS.2016.2637439.

[58] T. Young, D. Hazarika, S. Poria, and E. Cambria, “Recent trends in deep learning based natural language processing [Review Article],” *IEEE Computational Intelligence Magazine*, vol. 13, no. 3. Institute of Electrical and Electronics Engineers Inc., pp. 55–75, Aug.01, 2018. doi: 10.1109/MCI.2018.2840738.

[59] D. W. Otter, J. R. Medina, and J. K. Kalita, “A survey of the usages of deep learning in natural language processing,” arXiv, Jul. 27, 2018. doi: 10.1109/tnnls.2020.2979670.

[60] S. Wang, J. Cao, and P. S. Yu, “Deep learning for spatio-temporal data mining: a survey,” arXiv, Jun.11, 2019. doi: 10.1109/tkde.2020.3025580.

[61] P. Wlodarczak, J. Soar, and M. Ally, “Multimedia data mining using deep learning,” in *2015 5th International Conference on Digital Information Processing and Communications, ICDIPC 2015*, Nov. 2015, pp. 190–196. doi: 10.1109/ICDIPC.2015.7323027.

CITED LITERATURE (Continued)

[62] H. Kabir, Y. Wang, M. Yu, and Q. J. Zhang, “Neural network inverse modeling and applications to microwave filter design,” *IEEE Trans. Microw. Theory Tech.*, vol. 56, no. 4, pp. 867–879, Apr.2008, doi: 10.1109/TMTT.2008.919078.

[63] S. R. H. Hoole, “Artificial Neural Networks in the Solution of Inverse Electromagnetic Field Problems,” *IEEE Trans. Magn.*, vol. 29, no. 2, pp. 1931–1934, 1993, doi: 10.1109/20.250786.

[64] S. X. Ta, I. Park, and R. W. Ziolkowski, “Crossed Dipole Antennas: A review,” *IEEE Antennas Propag. Mag.*, vol. 57, no. 5, pp. 107–122, Oct.2015, doi: 10.1109/MAP.2015.2470680.

[65] C. A. Balanis, “Antenna theory: A Review," in Proceedings of the IEEE, vol. 80, no. 1, pp. 7-23, Jan. 1992, doi: 10.1109/5.119564.

[66] C. A. Balanis, “Antenna Theory: A Review,” *Proc. IEEE*, vol. 80, no. 1, pp. 7–23, 1992, doi: 10.1109/5.119564.

[67] D. F. Filipovic, W. Y. Ali-Ahmad, and G. M. Rebeiz, “Millimeter-Wave Double-Dipole Antennas for High-Gain Integrated Reflector Illumination,” *IEEE Trans. Microw. Theory Tech.*, vol. 40, no. 5, pp. 962–967, 1992, doi: 10.1109/22.137404.

[68] D. F. Filipovic, W. Y. Ali-Ahmad, and G. M. Rebeiz, “Millimeter-wave double-dipole antennas for high-gain integrated reflector illumination,” in IEEE Transactions on Microwave Theory and Techniques, vol. 40, no. 5, pp. 962-967, May 1992, doi: 10.1109/22.137404.

[69] H. F. Hofmann, T. Kosako, and Y. Kadoya, “Design parameters for a nano-optical Yagi–Uda antenna,” *New J. Phys.*, vol. 9, no. 7, p. 217, Jul.2007, doi: 10.1088/1367-2630/9/7/217.

[70] J. Hao, J. Ren, X. Du, J. H. Mikkelsen, M. Shen, and Y. Z. Yin, “Pattern-Reconfigurable Yagi-Uda Antenna Based on Liquid Metal,” *IEEE Antennas Wirel. Propag. Lett.*, vol. 20, no. 4, pp. 587–591, Apr.2021, doi: 10.1109/LAWP.2021.3058115.

CITED LITERATURE (Continued)

[71] R. A. Alhalabi and G. M. Rebeiz, “Differentially-fed millimeter-wave yagi-uda antennas with folded dipole feed,” *IEEE Trans. Antennas Propag.*, vol. 58, no. 3, pp. 966–969, Mar.2010, doi: 10.1109/TAP.2009.2039320.

[72] M. T. Wu and M. L. Chuang, “Multibroadband Slotted Bow-Tie Monopole Antenna,” *IEEE Antennas Wirel. Propag. Lett.*, vol. 14, pp. 887–890, 2015, doi: 10.1109/LAWP.2014.2383441.

[73] A. C. Durgun, C. A. Balanis, C. R. Birtcher, and D. R. Allee, “Design, simulation, fabrication and testing of flexible bow-tie antennas,” *IEEE Trans. Antennas Propag.*, vol. 59, no. 12, pp. 4425–4435, Dec.2011, doi: 10.1109/TAP.2011.2165511.

[74] D. Kaushal and A. Sonker, “Fractals for Custom Monopole Antenna Solutions: A Review,” *IEEE Technical Review*, vol. 39, no. 2, pp. 402–410, 2020, doi: 10.1080/02564602.2020.1837683.

[75] C. Kittiyanpunya and M. Krairiksh, “A four-beam pattern reconfigurable Yagi-Uda antenna,” *IEEE Trans. Antennas Propag.*, vol. 61, no. 12, pp. 6210–6214, 2013, doi: 10.1109/TAP.2013.2282914.

[76] E. Lier, “Review of soft and hard horn antennas, including metamaterial-based hybrid-mode horns,” *IEEE Antennas Propag. Mag.*, vol. 52, no. 2, pp. 31–39, Apr.2010, doi: 10.1109/MAP.2010.5525564.

[77] G. M. Rebeiz and D. B. Rutledge, “Integrated horn antennas for millimeter-wave applications,” *Ann. Des Télécommunications*, vol. 47, no. 1–2, pp. 38–48, Jan.1992, doi: 10.1007/BF02998725/METRICS.

[78] N. Tevar, P. Mehta, and K. Bhatt, “A review paper on conical corrugated horn antenna,” *Proc. 2016 IEEE Int. Conf. Wirel. Commun. Signal Process. Networking, WiSPNET 2016*, pp. 889–892, Sep.2016, doi: 10.1109/WISPNET.2016.7566260.

CITED LITERATURE (Continued)

[79] S. Hur, Y. J. Cho, J. Lee, N. G. Kang, J. Park, and H. Benn, "Synchronous channel sounder using horn antenna and indoor measurements on 28 GHz," *2014 IEEE Int. Black Sea Conf. Commun. Networking, BlackSeaCom 2014*, pp. 83–87, 2014, doi: 10.1109/BLACKSEACOM.2014.6849010.

[80] R. T. Lee and G. S. Smith, "A design study for the basic TEM horn antenna," *IEEE Antennas Propag. Mag.*, vol. 46, no. 1, pp. 86–92, Feb.2004, doi: 10.1109/MAP.2004.1296150.

[81] A. R. Mallahzadeh and S. Esfandiarpour, "Wideband H-Plane horn antenna based on ridge substrate integrated waveguide (RSIW)," *IEEE Antennas Wirel. Propag. Lett.*, vol. 11, pp. 85–88, 2012, doi: 10.1109/LAWP.2012.2183110.

[82] A. R. Weily, K. P. Esselle, B. C. Sanders, and T. S. Bird, "A woodpile EBG sectoral horn antenna," *IEEE Antennas Propag. Soc. AP-S Int. Symp.*, vol. 4 B, pp. 323–326, 2005, doi: 10.1109/APS.2005.1552813.

[83] A. R. Weily, K. P. Esselle, T. S. Bird, and B. C. Sanders, "Linear array of woodpile EBG sectoral horn antennas," *IEEE Trans. Antennas Propag.*, vol. 54, no. 8, pp. 2263–2274, Aug.2006, doi: 10.1109/TAP.2006.879181.

[84] A. P. King, "The Radiation Characteristics of Conical Horn Antennas," *Proc. IRE*, vol. 38, no. 3, pp. 249–251, 1950, doi: 10.1109/JRPROC.1950.230734.

[85] H. Choi and S. Lee, "Design of an exponentially-tapered TEM horn antenna for the wide broadband communication," *Microw. Opt. Technol. Lett.*, vol. 40, no. 6, pp. 531–534, Mar.2004, doi: 10.1002/MOP.20025.

[86] R. Orr, G. Goussetis, and V. Fusco, "Design method for circularly polarized fabry-perot cavity antennas," *IEEE Trans. Antennas Propag.*, vol. 62, no. 1, pp. 19–26, 2014, doi: 10.1109/TAP.2013.2286839.

[87] Y. H. Lv, X. Ding, and B. Z. Wang, "Dual-Wideband High-Gain Fabry-Perot Cavity Antenna," *IEEE Access*, vol. 8, pp. 4754–4760, 2020, doi: 10.1109/ACCESS.2019.2962078.

CITED LITERATURE (Continued)

[88] L. Y. Ji, P. Y. Qin, and Y. J. Guo, “Wideband Fabry-Perot Cavity Antenna with a Shaped Ground Plane,” *IEEE Access*, vol. 6, pp. 2291–2297, Dec.2017, doi: 10.1109/ACCESS.2017.2782749.

[89] L. DaXu, W. He, and S. Li, “Internet of things in industries: A survey,” *IEEE Trans. Ind. Informatics*, vol. 10, no. 4, pp. 2233–2243, Nov.2014, doi: 10.1109/TII.2014.2300753.

[90] E. Yurtsever, J. Lambert, A. Carballo, and K. Takeda, “A Survey of Autonomous Driving: Common Practices and Emerging Technologies,” *IEEE Access*, vol. 8, pp. 58443–58469, 2020, doi: 10.1109/ACCESS.2020.2983149.

[91] A. S. M. Mosa, I. Yoo, and L. Sheets, “A systematic review of healthcare applications for smartphones,” *BMC Med. Inform. Decis. Mak.*, vol. 12, no. 1, pp. 1–31, Jul.2012, doi: 10.1186/1472-6947-12-67/TABLES/12.

[92] S. Suresh and P. V. Sruthi, “A review on smart home technology,” *IC-GET 2015 - Proc. 2015 Online Int. Conf. Green Eng. Technol.*, Apr.2016, doi: 10.1109/GET.2015.7453832.

[93] R. Tian, B. K. Lau, and Z. Ying, “Multiplexing efficiency of MIMO antennas,” *IEEE Antennas Wirel. Propag. Lett.*, vol. 10, pp. 183–186, 2011, doi: 10.1109/LAWP.2011.2125773.

[94] H. Zhang, Z. Wang, J. Yu, and J. Huang, “A compact MIMO antenna for wireless communication,” *IEEE Antennas Propag. Mag.*, vol. 50, no. 6, pp. 104–107, 2008, doi: 10.1109/MAP.2008.4768932.

[95] A. A. Ibrahim, J. Machac, and R. M. Shubair, “Compact UWB MIMO antenna with pattern diversity and band rejection characteristics,” *Microw. Opt. Technol. Lett.*, vol. 59, no. 6, pp. 1460–1464, Jun.2017, doi: 10.1002/MOP.30564.

[96] D. A. Gore and A. J. Paulraj, “MIMO antenna subset selection with space-time coding,” *IEEE Trans. Signal Process.*, vol. 50, no. 10, pp. 2580–2588, Oct.2002, doi: 10.1109/TSP.2002.803337.

CITED LITERATURE (Continued)

[97] M. A. Maisto, R. Pierri, and R. Solimene, “Near-Field Warping Sampling Scheme for Broad-Side Antenna Characterization,” *Electron. 2020, Vol. 9, Page 1047*, vol. 9, no. 6, p. 1047, Jun.2020, doi: 10.3390/ELECTRONICS9061047.

[98] F. R. Varela, B. G. Iragüen, and M. Sierra-Castañer, “Near-Field to Far-Field Transformation on Arbitrary Surfaces via Multi-Level Spherical Wave Expansion,” *IEEE Trans. Antennas Propag.*, vol. 68, no. 1, pp. 500–508, Jan.2020, doi: 10.1109/TAP.2019.2935108.

[99] A. D. Yaghjian, “An Overview of Near-Field Antenna Measurements,” *IEEE Trans. Antennas Propag.*, vol. 34, no. 1, pp. 30–45, 1986, doi: 10.1109/TAP.1986.1143727.

[100] G. A. Woonton, “The Effect of an Obstacle in the Fresnel Field on the Distant Field of a Linear Radiator,” *J. Appl. Phys.*, vol. 21, no. 6, p. 577, Apr.2004, doi: 10.1063/1.1699710.

[101] R. P. GLOVER, J. R. KITCHELL, R. H. KYLE, J. C. DAVILA, and R. G. TROUT, “Experiences with Myocardial Revascularization By Division of the Internal Mammary Arteries,” *Dis. Chest*, vol. 33, no. 6, pp. 637–657, Jun.1958, doi: 10.1378/CHEST.33.6.637.

[102] D. M. Kerns, “Plane-Wave Scattering-Matrix Theory of Antennas And Antenna-Antenna Interactions: Formulation And Applications”, Mathematical Sciences, vol. 80B, pp. 5-51, 1976, doi: 10.6028/NBS.IR.75-824.

[103] P. F. Wacker, “Non-planar near field measurements: Spherical scanning,” Final Report, National Bureau of Standards, 1975, Accessed: Jan.17, 2023. [Online]. Available: https://ui.adsabs.harvard.edu/abs/1975nbs..reptR....W/abstract

[104] P. J. Wood, “The prediction of antenna characteristics from spherical near field measurements. II - Experimental validation,” *MarRv*, vol. 40, pp. 117–155, 1977, Accessed: Jan.17, 2023. [Online]. Available: https://ui.adsabs.harvard.edu/abs/1977MarRv..40..117W/abstract

CITED LITERATURE (Continued)

[105] A. D. Yaghjian and R. C. Wittmann, “The Receiving Antenna as a Linear Differential Operator: Application to Spherical Near-Field Scanning,” *IEEE Trans. Antennas Propag.*, vol. 33, no. 11, pp. 1175–1185, 1985, doi: 10.1109/TAP.1985.1143520.

[106] A. Capozzoli, C. Curcio, and A. Liseno, “Truncation in quasi-raster near-field acquisitions [Measurements Corner],” *IEEE Antennas Propag. Mag.*, vol. 54, no. 5, pp. 174–183, 2012, doi: 10.1109/MAP.2012.6348140.

[107] J. Wang and A. Yarovoy, “Sampling Design of Synthetic Volume Arrays for Three-Dimensional Microwave Imaging,” *IEEE Trans. Comput. Imaging*, vol. 4, no. 4, pp. 648–660, Dec.2018, doi: 10.1109/TCI.2018.2875332.

[108] C. Jiang, Y. C. Soh, and H. Li, “Sensor placement by maximal projection on minimum eigenspace for linear inverse problems,” *IEEE Trans. Signal Process.*, vol. 64, no. 21, pp. 5595–5610, Nov.2016, doi: 10.1109/TSP.2016.2573767.

[109] J. Ranieri, A. Chebira, and M. Vetterli, “Near-optimal sensor placement for linear inverse problems,” *IEEE Trans. Signal Process.*, vol. 62, no. 5, pp. 1135–1146, Mar.2014, doi: 10.1109/TSP.2014.2299518.

[110] S. Joshi and S. Boyd, “Sensor selection via convex optimization,” *IEEE Trans. Signal Process.*, vol. 57, no. 2, pp. 451–462, 2009, doi: 10.1109/TSP.2008.2007095.

[111] J. Laviada, A. Arboleya-Arboleya, Y. Álvarez, B. González-Valdés, and F. Las-Heras, “Multiview three-dimensional reconstruction by millimetre-wave portable camera,” *Sci. Reports 2017 71*, vol. 7, no. 1, pp. 1–11, Jul.2017, doi: 10.1038/s41598-017-06475-7.

[112] M.G. Fernandez, Y. A. Lopez, and F. L. H. Andres, “Antenna measurement and diagnostics processing techniques using unmanned aerial vehicles," in 2019 13th European Conference on Antennas and Propagation (EuCAP), pp. 1-5, 2019.

CITED LITERATURE (Continued)

[113] M.G. Fernandez, Y. A. Lopez, and F. L. H. Andres, “Advances in Antenna Measurement and Characterization Using Unmanned Aerial Vehicles," in 2019 13th European Conference on Antennas and Propagation (EuCAP), pp. 1-5, 2019.

[114] F. R. Varela, B. G. Iraguen, and M. Sierra-Castaner, “Application of Nonuniform FFT to Spherical Near-Field Antenna Measurements,” *IEEE Trans. Antennas Propag.*, vol. 68, no. 11, pp. 7571–7579, Nov.2020, doi: 10.1109/TAP.2020.2998898.

[115] F. R. Varela, B. G. Iraguen, and M. Sierra-Castaner, “Under-sampled spherical near-field antenna measurements with error estimation,” *IEEE Trans. Antennas Propag.*, vol. 68, no. 8, pp. 6364–6371, Aug.2020, doi: 10.1109/TAP.2020.2986718.

[116] S. Aerts *et al.*, “In-situ measurement methodology for the assessment of 5G NR massive MIMO base station exposure at sub-6 GHz frequencies,” *IEEE Access*, vol. 7, pp. 184658–184667, 2019, doi: 10.1109/ACCESS.2019.2961225.

[117] S. Aerts *et al.*, “In Situ Assessment of 5G NR Massive MIMO Base Station Exposure in a Commercial Network in Bern, Switzerland,” *Appl. Sci. 2021, Vol. 11, Page 3592*, vol. 11, no. 8, p. 3592, Apr.2021, doi: 10.3390/APP11083592.

[118] F. Jameel, Faisal, M. A. A. Haider, and A. A. Butt, “Massive MIMO: A survey of recent advances, research issues and future directions,” *2017 Int. Symp. Recent Adv. Electr. Eng. RAEE 2017*, vol. 2018-January, pp. 1–6, Jun.2017, doi: 10.1109/RAEE.2017.8246040.

[119] K. W. Forsythe, D. W. Bliss, and G. S. Fawcett, “Multiple-Input Multiple-Output (MIMO) radar: Performance issues,” *Conf. Rec. - Asilomar Conf. Signals, Syst. Comput.*, vol. 1, pp. 310–315, 2004, doi: 10.1109/ACSSC.2004.1399143.

[120] A. Kumar, A. Q. Ansari, B. K. Kanaujia, J. Kishor, and L. Matekovits, “A Review on Different Techniques of Mutual Coupling Reduction Between Elements of Any MIMO Antenna. Part 1: DGSs and Parasitic Structures,” *Radio Sci.*, vol. 56, no. 3, p. e2020RS007122, Mar.2021, doi: 10.1029/2020RS007122.

CITED LITERATURE (Continued)

[121] A. Kumar, A. Q. Ansari, B. K. Kanaujia, J. Kishor, and L. Matekovits, “A Review on Different Techniques of Mutual Coupling Reduction Between Elements of Any MIMO Antenna. Part 2: Metamaterials and Many More,” *Radio Sci.*, vol. 56, no. 3, p. e2020RS007222, Mar.2021, doi: 10.1029/2020RS007222.

[122] H. Huang, Y. Liu, S. S. Zhang, and S. X. Gong, “Compact polarization diversity ultrawideband mimo antenna with triple band-notched characteristics,” *Microw. Opt. Technol. Lett.*, vol. 57, no. 4, pp. 946–953, Apr.2015, doi: 10.1002/MOP.28957.

[123] H. Huang, Y. Liu, and S. X. Gong, “Broadband omnidirectional dual-polarized antenna with high isolation,” *Microw. Opt. Technol. Lett.*, vol. 57, no. 8, pp. 1848–1852, Aug.2015, doi: 10.1002/MOP.29199.

[124] W. J. Liao, C. Y. Hsieh, B. Y. Dai, and B. R. Hsiao, “Inverted-F/Slot Integrated Dual-Band Four-Antenna System for WLAN Access Points,” *IEEE Antennas Wirel. Propag. Lett.*, vol. 14, pp. 847–850, 2015, doi: 10.1109/LAWP.2014.2381362.

[125] Nirdosh, C. M. Tan, and M. R. Tripathy, “A miniaturized T-shaped MIMO antenna for X-band and Ku-band applications with enhanced radiation efficiency,” *2018 27th Wirel. Opt. Commun. Conf. WOCC 2018*, pp. 1–5, Jun.2018, doi: 10.1109/WOCC.2018.8372695.

[126] A. MoradiKordalivand, T. A. Rahman, and M. Khalily, “Common Elements Wideband MIMO Antenna System for WiFi/LTE Access-Point Applications,” *IEEE Antennas Wirel. Propag. Lett.*, vol. 13, pp. 1601–1604, 2014, doi: 10.1109/LAWP.2014.2347897.

[127] J. Deng, J. Li, L. Zhao, and L. Guo, “A Dual-Band Inverted-F MIMO Antenna with Enhanced Isolation for WLAN Applications,” *IEEE Antennas Wirel. Propag. Lett.*, vol. 16, pp. 2270–2273, 2017, doi: 10.1109/LAWP.2017.2713986.

[128] D. Lu, L. Wang, E. Yang, and G. Wang, “Design of High-Isolation Wideband Dual-Polarized Compact MIMO Antennas with Multiobjective Optimization,” *IEEE Trans. Antennas Propag.*, vol. 66, no. 3, pp. 1522–1527, Mar.2018, doi: 10.1109/TAP.2017.2784446.

CITED LITERATURE (Continued)

[129] D. N. Elsheakh, H. A. Elsadek, E. A. Abdallah, M. F. Iskander, and H. Elhenawy, “Low mutual coupling 2 × 2 microstrip patch array antenna by using novel shapes of defect ground structure,” *Microw. Opt. Technol. Lett.*, vol. 52, no. 5, pp. 1208–1215, May2010, doi: 10.1002/MOP.25152.

[130] S. K. Sahu, B. A. Kumar, and K. K. Sethi, “Dual Notch Band Rejected Filter with Defected Slot for WLAN and Satellite Applications,” *Lect. Notes Electr. Eng.*, vol. 601, pp. 1184–1189, 2020, doi: 10.1007/978-981-15-1420-3_129/FIGURES/5.

[131] M. Munde, A. Nandgaonkar, and S. Deosarkar, “Dual Feed Wideband Annular Ring Microstrip Antenna with Circular DGS for Reduced SAR,” *Prog. Electromagn. Res. B*, vol. 88, pp. 175–195, 2020, doi: 10.2528/PIERB20071804.

[132] Q. Li *et al.*, “Mutual Coupling Reduction between Patch Antennas Using Meander Line,” *Int. J. Antennas Propag.*, vol. 2018, 2018, doi: 10.1155/2018/2586382.

[133] L. Wu, H. Lyu, and H. Yu, “A Novel Compact UWB-MIMO Antenna with Quintuple Notched-Band Characteristics,” *Wirel. Pers. Commun.*, vol. 108, no. 3, pp. 1827–1840, Oct.2019, doi: 10.1007/S11277-019-06498-5/FIGURES/12.

[134] H. Arun, A. K. Sarma, M. Kanagasabai, S. Velan, C. Raviteja, and M. G. N. Alsath, “Deployment of modified serpentine structure for mutual coupling reduction in MIMO antennas,” *IEEE Antennas Wirel. Propag. Lett.*, vol. 13, pp. 277–280, 2014, doi: 10.1109/LAWP.2014.2304541.

[135] M. S. Sharawi, M. A. Jan, and D. N. Aloi, “Four-shaped 2×2 multi-standard compact multiple-input-multiple-output antenna system for long-term evolution mobile handsets,” *IET Microwaves, Antennas Propag.*, vol. 6, no. 6, pp. 685–696, Apr.2012, doi: 10.1049/IET-MAP.2011.0528/CITE/REFWORKS.

[136] Y. Sun, Y. He, W. He, L. Zhang, and S. W. Wong, “A Wideband Circularly Polarized Cross-Dipole Antenna with L-shape Slots,” *2020 IEEE Int. Symp. Antennas Propag. North Am. Radio Sci. Meet. IEEECONF 2020 - Proc.*, pp. 673–674, Jul.2020, doi: 10.1109/IEEECONF35879.2020.9330316.

CITED LITERATURE (Continued)

[137] X. Liu, M. Amin, and J. Liang, "Wideband MIMO antenna with enhanced isolation for wireless communication application," *IEICE Electron. Express*, vol. 15, no. 22, pp. 20180948–20180948, Nov.2018, doi: 10.1587/ELEX.15.20180948.

[138] S. Singhal, "Four element ultra-wideband fractal multiple-input multiple-output antenna," *Microw. Opt. Technol. Lett.*, vol. 61, no. 12, pp. 2811–2818, Dec.2019, doi: 10.1002/MOP.31980.

[139] R. G. Saadallah Alsultan and G. Ö. Yetkin, "Mutual coupling reduction of E-shaped MIMO antenna with matrix of C-shaped resonators," *Int. J. Antennas Propag.*, vol. 2018, 2018, doi: 10.1155/2018/4814176.

[140] V. G. Veselago, "The Electrodynamics of Substances With Simultaneously Negative Values of ε AND μ," *Sov. Phys. Uspekhi*, vol. 10, no. 4, p. 509, Apr. 1968, doi: 10.1070/PU1968V010N04ABEH003699.

[141] D. Schurig *et al.*, "Metamaterial electromagnetic cloak at microwave frequencies," *Science (80-.).*, vol. 314, no. 5801, pp. 977–980, Nov.2006, doi: 10.1126/SCIENCE.1133628/SUPPL_FILE/SCHURIG.SOM.PDF.

[142] J. Y. Lee, S. H. Kim, and J. H. Jang, "Reduction of Mutual Coupling in Planar Multiple Antenna by Using 1-D EBG and SRR Structures," *IEEE Trans. Antennas Propag.*, vol. 63, no. 9, pp. 4194–4198, Sep. 2015, doi: 10.1109/TAP.2015.2447052.

[143] A. Ramachandran, S. V. Pushpakaran, M. Pezholil, and V. Kesavath, "A Four-Port MIMO Antenna Using Concentric Square-Ring Patches Loaded with CSRR for High Isolation," *IEEE Antennas Wirel. Propag. Lett.*, vol. 15, pp. 1196–1199, 2016, doi: 10.1109/LAWP.2015.2499322.

[144] M. Bilal, R. Saleem, H. H. Abbasi, M. F. Shafique, and A. K. Brown, "An FSS-Based Nonplanar Quad-Element UWB-MIMO Antenna System," *IEEE Antennas Wirel. Propag. Lett.*, vol. 16, pp. 987–990, 2017, doi: 10.1109/LAWP.2016.2615884.

[145] H. M. Bernety and A. B. Yakovlev, "Reduction of Mutual Coupling Between Neighboring Strip Dipole Antennas Using Confocal Elliptical Metasurface Cloaks," *IEEE Trans. Antennas Propag.*, vol. 63, no. 4, pp. 1554–1563, Apr. 2015, doi: 10.1109/TAP.2015.2398121.

[146] Z. H. Jiang, P. E. Sieber, L. Kang, and D. H. Werner, "Restoring Intrinsic Properties of Electromagnetic Radiators Using Ultralightweight Integrated Metasurface Cloaks," *Adv. Funct. Mater.*, vol. 25, no. 29, pp. 4708–4716, Aug. 2015, doi: 10.1002/ADFM.201501261.

[147] S. Gupta, A. Kumar, and N. Kumar, "Design of ECC based authenticated group key agreement protocol using self-certified public keys," *Proc. 4th IEEE Int. Conf. Recent Adv. Inf. Technol. RAIT 2018*, pp. 1–5, Jun. 2018, doi: 10.1109/RAIT.2018.8388999.

[148] J. Y. Lee, Y. H.Chen, and P. Y. Chen, "Degeneracy of light scattering and absorption by a single nanowire," *Sci. Reports 2021 111*, vol. 11, no. 1, pp. 1–8, Sep.2021, doi: 10.1038/s41598-021-98011-x.

[149] A. Oklopi, C. M. Hirata, K. Heng, R. B. Miles, W. R. Lempert, and J. N. Forkey, "Laser Rayleigh scattering," *Meas. Sci. Technol.*, vol. 12, no. 5, p. R33, May 2001, doi: 10.1088/0957-0233/12/5/201.

[150] F. Q. Zhao and H. Hiroyasu, "The applications of laser Rayleigh scattering to combustion diagnostics," *Prog. Energy Combust. Sci.*, vol. 19, no. 6, pp. 447–485, Jan. 1993, doi: 10.1016/0360-1285(93)90001-U.

[151] L. Cao *et al.*, "Semiconductor nanowire optical antenna solar absorbers," *Nano Lett.*, vol. 10, no. 2, pp. 439–445, Feb. 2010, doi: 10.1021/NL9036627/SUPPL_FILE/NL9036627_SI_001.PDF.

[152] E. C. Garnett, M. L. Brongersma, Y. Cui, and M. D. McGehee, "Nanowire Solar Cells," *https://doi.org/10.1146/annurev-matsci-062910-100434*, vol. 41, pp. 269–295, Jul. 2011, doi: 10.1146/ANNUREV-MATSCI-062910-100434.

[153] S. Arslanagić and R. W. Ziolkowski, "Highly Subwavelength, Superdirective Cylindrical Nanoantenna," *Phys. Rev. Lett.*, vol. 120, no. 23, p. 237401, Jun. 2018, doi: 10.1103/PHYSREVLETT.120.237401/FIGURES/5/MEDIUM.

[154] J. Y. Lee, A. E. Miroshnichenko, and R. K. Lee, "Reexamination of Kerker's conditions by means of the phase diagram," *Phys. Rev. A*, vol. 96, no. 4, p. 043846, Oct. 2017, doi: 10.1103/PHYSREVA.96.043846/FIGURES/4/MEDIUM.

[155] J. Y. Lee, R. K. Lee, and A. E. Miroshnichenko, "Simultaneously nearly zero forward and nearly zero backward scattering objects," *Opt. Express, Vol. 26, Issue 23, pp. 30393-30399*, vol. 26, no. 23, pp. 30393–30399, Nov. 2018, doi: 10.1364/OE.26.030393.

[156] M. L. Brongersma, Y. Cui, and S. Fan, "Light management for photovoltaics using high-index nanostructures," *Nat. Mater. 2014 135*, vol. 13, no. 5, pp. 451–460, Apr. 2014, doi: 10.1038/nmat3921.

[157] K. Kneipp *et al.*, "Single Molecule Detection Using Surface-Enhanced Raman Scattering (SERS)," *Phys. Rev. Lett.*, vol. 78, no. 9, p. 1667, Mar. 1997, doi: 10.1103/PhysRevLett.78.1667.

[158] T. Huynh *et al.*, "Estimating CT Image from MRI Data Using Structured Random Forest and Auto-Context Model," *IEEE Trans. Med. Imaging*, vol. 35, no. 1, pp. 174–183, Jan. 2016, doi: 10.1109/TMI.2015.2461533.

[159] R. E. Hamam, A. Karalis, J. D. Joannopoulos, and M. Soljačić, "Coupled-mode theory for general free-space resonant scattering of waves," *Phys. Rev. A - At. Mol. Opt. Phys.*, vol. 75, no. 5, p. 053801, May 2007, doi: 10.1103/PHYSREVA.75.053801/FIGURES/2/MEDIUM.

[160] M. I. Tribelsky and B. S. Luk'yanchuk, "Anomalous light scattering by small particles," *Phys. Rev. Lett.*, vol. 97, no. 26, p. 263902, Dec. 2006, doi: 10.1103/PHYSREVLETT.97.263902/FIGURES/2/MEDIUM.

[161] Z. Ruan and S. Fan, "Design of subwavelength superscattering nanospheres," *Appl. Phys. Lett.*, vol. 98, no. 4, p. 043101, Jan. 2011, doi: 10.1063/1.3536475.

CITED LITERATURE (Continued)

[162] C. Qian *et al.*, “Experimental Observation of Superscattering,” *Phys. Rev. Lett.*, vol. 122, no. 6, p. 063901, Feb. 2019, doi: 10.1103/PHYSREVLETT.122.063901/FIGURES/4/MEDIUM.

[163] Z. Ruan and S. Fan, “Superscattering of light from subwavelength nanostructures,” *Phys. Rev. Lett.*, vol. 105, no. 1, p. 013901, Jun. 2010, doi: 10.1103/PHYSREVLETT.105.013901/FIGURES/4/MEDIUM.

[164] N. M. Estakhri and A. Alù, “Minimum-scattering superabsorbers,” *Phys. Rev. B - Condens. Matter Mater. Phys.*, vol. 89, no. 12, p. 121416, Mar.2014, doi: 10.1103/PHYSREVB.89.121416/FIGURES/3/MEDIUM.

[165] J. Y. Lee *et al.*, “Phase diagram for passive electromagnetic scatterers,” *Opt. Express*, vol. 24, no. 6, pp. 6480–6489, Mar. 2016, doi: 10.1364/OE.24.006480.

[166] A. E. Miroshnichenko and M. I. Tribelsky, “Ultimate Absorption in Light Scattering by a Finite Obstacle,” *Phys. Rev. Lett.*, vol. 120, no. 3, p. 033902, Jan.2018, doi: 10.1103/PHYSREVLETT.120.033902/FIGURES/2/MEDIUM.

[167] H. Noh, Y. Chong, A. D. Stone, and H. Cao, “Perfect coupling of light to surface plasmons by coherent absorption,” *Phys. Rev. Lett.*, vol. 108, no. 18, p. 186805, May 2012, doi: 10.1103/PHYSREVLETT.108.186805/FIGURES/4/MEDIUM.

[168] Z. R. Zhang, H. Q. Li, H. Chen, P. Bai, Y. Wu, and Y. Lai, “Multi-channel coherent perfect absorbers,” *Europhys. Lett.*, vol. 114, no. 2, p. 28003, May 2016, doi: 10.1209/0295-5075/114/28003.

[169] E. D. Palik, “Handbook of Optical Constants of Solids," 1991, https://books.google.com/books?hl=zh-TW&lr=&id=nxoqxyoHfbIC&oi=fnd&pg=PA3&ots=EG2XFCs_il&sig=H-OzxiHDthAI_iw2ZjtwYtoFqfk#v=onepage&q&f=false (accessed Jan.17, 2023).

[170] P. Pirinen, “A brief overview of 5G research activities,” *Proc. 2014 1st Int. Conf. 5G Ubiquitous Connect. 5GU 2014*, pp. 17–22, Feb.2014, doi: 10.4108/ICST.5GU.2014.258061.

CITED LITERATURE (Continued)

[171] I. Ahmad, S. Shahabuddin, T. Kumar, J. Okwuibe, A. Gurtov, and M. Ylianttila, “Security for 5G and beyond,” *IEEE Commun. Surv. Tutorials*, vol. 21, no. 4, pp. 3682–3722, Oct. 2019, doi: 10.1109/COMST.2019.2916180.

[172] R. Dangi, P. Lalwani, G. Choudhary, I. You, and G. Pau, “Study and Investigation on 5G Technology: A Systematic Review,” *Sensors 2022*, vol. 22, no. 1, pp. 26, Dec. 2021, doi: 10.3390/S22010026.

[173] N. Al-Falahy and O. Y. Alani, “Technologies for 5G Networks: Challenges and Opportunities,” *IT Prof.*, vol. 19, no. 1, pp. 12–20, Jan. 2017, doi: 10.1109/MITP.2017.9.

[174] J. Sae, P. Kurvi, S. Andreev, and M. Valkama, “Agile 5G Network Measurements: Operator Benefits of Employing Aerial Mobility,” *IEEE Internet Things Mag.*, vol. 5, no. 2, pp. 114–119, Sep. 2022, doi: 10.1109/IOTM.002.2200023.

[175] V. Sciancalepore, “First Responders Got Wings: UAVs to the Rescue of Localization Operations in Beyond 5G Systems,” *IEEE Commun. Mag.*, vol. 59, no. 11, pp. 28–34, Nov. 2021, doi: 10.1109/MCOM.101.2100273.

[176] V. Platzgummer, V. Raida, G. Krainz, P. Svoboda, M. Lerch, and M. Rupp, “UAV-Based coverage measurement method for 5G,” *IEEE Veh. Technol. Conf.*, vol. 2019-September, Sep. 2019, doi: 10.1109/VTCFALL.2019.8891252.

[177] L. L. Coq, C. Marchais, P. Besnier, A. Sharaiha, and G. L. Ray, “Small and ultra wide band antennas: A new challenge for characterisation,”*in 2006 First European Conference on Antennas and Propagation, 2006, pp. 1-4*, doi: 10.1109/EUCAP.2006.4584610.

[178] A. M. Jawad, R. Nordin, S. K. Gharghan, H. M. Jawad, and M. Ismail, “Opportunities and Challenges for Near-Field Wireless Power Transfer: A Review,” *Energies 2017,* vol. 10, no. 7, pp. 1022, Jul. 2017, doi: 10.3390/EN10071022.

CITED LITERATURE (Continued)

[179] J. Zhang and G. Y. Tian, "UHF RFID Tag Antenna-Based Sensing for Corrosion Detection & Characterization Using Principal Component Analysis," *IEEE Trans. Antennas Propag.*, vol. 64, no. 10, pp. 4405–4414, Oct. 2016, doi: 10.1109/TAP.2016.2596898.

[180] L. Zhu, J. Zhu, S. Wang, and J. Zhang, "Adaptive Transmit Antenna Selection Based on PCA for Millimeter Wave LOS MIMO Channel," *IEEE Access*, vol. 7, pp. 12087–12096, 2019, doi: 10.1109/ACCESS.2019.2892869.

[181] M. Pastorino and A. Randazzo, "The SVM-based smart antenna for estimation of the directions of arrival of electromagnetic waves," *IEEE Trans. Instrum. Meas.*, vol. 55, no. 6, pp. 1918–1925, Dec. 2006, doi: 10.1109/TIM.2006.884295.

[182] Z. Zheng, X. Chen, and K. Huang, "Application of support vector machines to the antenna design," *Int. J. RF Microw. Comput. Eng.*, vol. 21, no. 1, pp. 85–90, Jan. 2011, doi: 10.1002/MMCE.20491.

[183] L. Cui, Y. Zhang, R. Zhang, and Q. H. Liu, "A Modified Efficient KNN Method for Antenna Optimization and Design," *IEEE Trans. Antennas Propag.*, vol. 68, no. 10, pp. 6858–6866, Oct. 2020, doi: 10.1109/TAP.2020.3001743.

[184] B. Aspe *et al.*, "Frequency-Tunable Slot-Loop Antenna Based on KNN Ferroelectric Interdigitated Varactors," *IEEE Antennas Wirel. Propag. Lett.*, vol. 20, no. 8, pp. 1414–1418, Aug. 2021, doi: 10.1109/LAWP.2021.3084320.

[185] H. M. ElMisilmani, T. Naous, and S. K. AlKhatib, "A review on the design and optimization of antennas using machine learning algorithms and techniques," *Int. J. RF Microw. Comput. Eng.*, vol. 30, no. 10, p. e22356, Oct. 2020, doi: 10.1002/MMCE.22356.

[186] G. L. Santos, P. T. Endo, D. Sadok, and J. Kelner, "When 5G Meets Deep Learning: A Systematic Review," *Algorithms 2020*, vol. 13, no. 9, pp. 208, Aug. 2020, doi: 10.3390/A13090208.

CITED LITERATURE (Continued)

[187] M. M. Khan, S. Hossain, P. Mozumdar, S. Akter, and R. H. Ashique, "A review on machine learning and deep learning for various antenna design applications," *Heliyon*, vol. 8, no. 4, p. e09317, Apr. 2022, doi: 10.1016/J.HELIYON.2022.E09317.

[188] A. G. Hernandes and T. Abrão, "CNN-aided multiple PU spectrum sensing in uncalibrated massive antennas SU system," *Phys. Commun.*, vol. 53, p. 101715, Aug. 2022, doi: 10.1016/J.PHYCOM.2022.101715.

[189] H. Cheng, S. Ma, and H. Lee, "CNN-Based mmWave Path Loss Modeling for Fixed Wireless Access in Suburban Scenarios," *IEEE Antennas Wirel. Propag. Lett.*, vol. 19, no. 10, pp. 1694–1698, Oct. 2020, doi: 10.1109/LAWP.2020.3014314.

[190] P. R. Burd, K. Mannheim, T. März, J. Ringholz, A. Kappes, and M. Kadler, "Detecting radio frequency interference in radio-antenna arrays with the recurrent neural network algorithm," *Astron. Nachrichten*, vol. 339, no. 5, pp. 358–362, Jun. 2018, doi: 10.1002/ASNA.201813505.

[191] S. Abeywickrama, L. Jayasinghe, H. Fu, S. Nissanka, and C. Yuen, "RF-based Direction Finding of UAVs Using DNN," *2018 IEEE Int. Conf. Commun. Syst. ICCS 2018*, pp. 157–161, Jul. 2018, doi: 10.1109/ICCS.2018.8689177.

[192] S. J. Patel and M. Zawodniok, "DNN-Based RFID Antenna Tags Localization," *Conf. Rec. - IEEE Instrum. Meas. Technol. Conf.*, vol. 2021-May, May 2021, doi: 10.1109/I2MTC50364.2021.9460004.

[193] C. D. Prakash and L. J. Karam, "It Gan do better: GaN-based detection of objects on images with varying quality," *IEEE Trans. Image Process.*, vol. 30, pp. 9220–9230, 2021, doi: 10.1109/TIP.2021.3124155.

[194] Y. Huang, F. Zheng, R. Cong, W. Huang, M. R. Scott, and L. Shao, "MCMT-GAN: Multi-Task Coherent Modality Transferable GAN for 3D Brain Image Synthesis," *IEEE Trans. Image Process.*, vol. 29, pp. 8187–8198, 2020, doi: 10.1109/TIP.2020.3011557.

[195] N. M. Ahmed *et al.*, “Nano and micro porous GaN characterization using image processing method,” *Optik (Stuttg).*, vol. 123, no. 12, pp. 1074–1078, Jun. 2012, doi: 10.1016/J.IJLEO.2011.07.034.

[196] Z. Wang, Q. She, and T. E. Ward, “Generative Adversarial Networks in Computer Vision,” *ACM Comput. Surv.*, vol. 54, no. 2, p. 37, Feb. 2021, doi: 10.1145/3439723.

[197] Y. J. Cao *et al.*, “Recent Advances of Generative Adversarial Networks in Computer Vision,” *IEEE Access*, vol. 7, 2019, doi: 10.1109/ACCESS.2018.2886814.

[198] S. A. Hussein, T. Tirer, and R. Giryes, “Image-Adaptive GAN Based Reconstruction,” *Proc. AAAI Conf. Artif. Intell.*, vol. 34, no. 04, pp. 3121–3129, Apr. 2020, doi: 10.1609/AAAI.V34I04.5708.

[199] X. Pan, X. Zhan, B. Dai, D. Lin, C. C. Loy, and P. Luo, “Exploiting Deep Generative Prior for Versatile Image Restoration and Manipulation,” *IEEE Trans. Pattern Anal. Mach. Intell.*, vol. 44, no. 11, pp. 7474–7489, Nov. 2022, doi: 10.1109/TPAMI.2021.3115428.

[200] X. Yu, Y. Qu, and M. Hong, “Underwater-GAN: Underwater Image Restoration via Conditional Generative Adversarial Network,” *Lect. Notes Comput. Sci. (including Subser. Lect. Notes Artif. Intell. Lect. Notes Bioinformatics)*, vol. 11188 LNCS, pp. 66–75, 2019, doi: 10.1007/978-3-030-05792-3_7/TABLES/1.

[201] I. J. Goodfellow *et al.*, “Generative Adversarial Networks,” *Sci. Robot.*, vol. 3, no. January, pp. 2672–2680, Jun. 2014, doi: 10.48550/arxiv.1406.2661.

[202] D. P. Kingma and J. L. Ba, “Adam: A Method for Stochastic Optimization,” *3rd Int. Conf. Learn. Represent. ICLR 2015 - Conf. Track Proc.*, Dec. 2014, doi: 10.48550/arxiv.1412.6980.

[203] M. A. Jensen and J. W. Wallace, “A review of antennas and propagation for MIMO wireless communications,” *IEEE Trans. Antennas Propag.*, vol. 52, no. 11, pp. 2810–2824, Nov. 2004, doi: 10.1109/TAP.2004.835272.

CITED LITERATURE (Continued)

[204] Y. Wu and Y. Long, "A High Isolation MIMO Antenna without Decoupling Structure for LTE 700 MHz," *Int. J. Antennas Propag.*, vol. 2015, 2015, doi: 10.1155/2015/436259.

[205] I. Leal, M. Alencar, and W. Lopes, "Particle Swarm Optimization Applied to Control of Mutual Coupling in MIMO Systems," *Proc. - 2019 IEEE Latin-American Conf. Commun. LATINCOM 2019*, Nov. 2019, doi: 10.1109/LATINCOM48065.2019.8937863.

[206] I. Kim, C. W. Jung, Y. Kim, and Y. E. Kim, "Low-profile wideband MIMO antenna with suppressing mutual coupling between two antennas," *Microw. Opt. Technol. Lett.*, vol. 50, no. 5, pp. 1336–1339, May 2008, doi: 10.1002/MOP.23368.

[207] A. Recioui and H. Bentarzi, "Genetic algorithm based MIMO capacity enhancement in spatially correlated channels including mutual coupling," *Wirel. Pers. Commun.*, vol. 63, no. 3, pp. 689–701, Apr. 2012, doi: 10.1007/S11277-010-0159-5/METRICS.

[208] A. Recioui, "Application of a Galaxy-Based Search Algorithm to MIMO System Capacity Optimization," *Arab. J. Sci. Eng.*, vol. 41, no. 9, pp. 3407–3414, Sep. 2016, doi: 10.1007/S13369-015-1934-0/METRICS.

[209] A. Recioui and Y. Grainat, "Application and Optimization of MIMO Communication in Wide Area Monitoring Systems," *Int. J. Data Sci.*, vol. 1, no. 2, pp. 82–98, May 2020, doi: 10.18517/IJODS.1.2.82-98.2020.

[210] S. Roy and U. Chakraborty, "Mutual Coupling Reduction in a Multi-band MIMO Antenna Using Meta-Inspired Decoupling Network," *Wirel. Pers. Commun.*, vol. 114, no. 4, pp. 3231–3246, Oct. 2020, doi: 10.1007/S11277-020-07526-5/TABLES/3.

[211] S. Zhang and G. F. Pedersen, "Mutual Coupling Reduction for UWB MIMO Antennas with a Wideband Neutralization Line," *IEEE Antennas Wirel. Propag. Lett.*, vol. 15, pp. 166–169, 2016, doi: 10.1109/LAWP.2015.2435992.

CITED LITERATURE (Continued)

[212] S. Luo, Y. Li, Y. Xia, and L. Zhang, "A Low Mutual Coupling Antenna Array with Gain Enhancement Using Metamaterial Loading and Neutralization Line Structure," The Applied Computational Electromagnetics Society Journal (ACES), vol. 34, no. 3, pp. 411-418, Mar. 2019, https://journals.riverpublishers.com/index.php/ACES/article/view/8555.

[213] S. Gupta, Z. Briqech, A. R. Sebak, and T. A. Denidni, "Mutual-Coupling Reduction Using Metasurface Corrugations for 28 GHz MIMO Applications," *IEEE Antennas Wirel. Propag. Lett.*, vol. 16, pp. 2763–2766, Aug. 2017, doi: 10.1109/LAWP.2017.2745050.

[214] Z. Wang, L. Zhao, Y. Cai, S. Zheng, and Y. Yin, "A Meta-Surface Antenna Array Decoupling (MAAD) Method for Mutual Coupling Reduction in a MIMO Antenna System," *Sci. Reports 2018 81*, vol. 8, no. 1, pp. 1–9, Feb. 2018, doi: 10.1038/s41598-018-21619-z.

[215] M. Alibakhshikenari *et al.*, "A Comprehensive Survey on 'Various Decoupling Mechanisms with Focus on Metamaterial and Metasurface Principles Applicable to SAR and MIMO Antenna Systems,'" *IEEE Access*, vol. 8, pp. 192965–193004, 2020, doi: 10.1109/ACCESS.2020.3032826.

[216] L. Zhu and P. Y. Chen, "A Low-RCS and Low-ECC Transparent Meta-Radomes Based on a Conductive Nanocomposite," *2021 IEEE Int. Symp. Antennas Propag. North Am. Radio Sci. Meet. APS/URSI 2021 - Proc.*, pp. 1859–1860, 2021, doi: 10.1109/APS/URSI47566.2021.9703729.

[217] M. Zhao, T. Anzai, F. Shi, X. Chen, K. Okada, and M. Inaba, "Design, Modeling, and Control of an Aerial Robot DRAGON: A Dual-Rotor-Embedded Multilink Robot with the Ability of Multi-Degree-of-Freedom Aerial Transformation," *IEEE Robot. Autom. Lett.*, vol. 3, no. 2, pp. 1176–1183, Apr. 2018, doi: 10.1109/LRA.2018.2793344.

[218] P. Naseri and S. V. Hum, "A Generative Machine Learning-Based Approach for Inverse Design of Multilayer Metasurfaces," *IEEE Trans. Antennas Propag.*, vol. 69, no. 9, pp. 5725–5739, Sep. 2021, doi: 10.1109/TAP.2021.3060142.

CITED LITERATURE (Continued)

[219] M. Yan *et al.*, “An FSS-backed reflective polarization conversion meta-surface for radar stealth,” *Photonics Nanostructures - Fundam. Appl.*, vol. 43, p. 100846, Feb. 2021, doi: 10.1016/J.PHOTONICS.2020.100846.

[220] M. Yan *et al.*, “An FSS-Backed Dual-Band Reflective Polarization Conversion Metasurface,” *IEEE Access*, vol. 7, pp. 104435–104442, 2019, doi: 10.1109/ACCESS.2019.2931551.

[221] F. Feng, X. Wang, and R. Li, “Cross-modal retrieval with correspondence autoencoder,” *MM 2014 - Proc. 2014 ACM Conf. Multimed.*, pp. 7–16, Nov. 2014, doi: 10.1145/2647868.2654902.

[222] G. Zhang, Y. Liu, and X. Jin, “A survey of autoencoder-based recommender systems,” *Front. Comput. Sci.*, vol. 14, no. 2, pp. 430–450, Apr. 2020, doi: 10.1007/S11704-018-8052-6/METRICS.

[223] Y. Yang, Q. M. J. Wu, and Y. Wang, “Autoencoder with Invertible Functions for Dimension Reduction and Image Reconstruction,” *IEEE Trans. Syst. Man, Cybern. Syst.*, vol. 48, no. 7, pp. 1065–1079, Jul.2018, doi: 10.1109/TSMC.2016.2637279.

[224] Z. Chen, C. K. Yeo, B. S. Lee, and C. T. Lau, “Autoencoder-based network anomaly detection,” *Wirel. Telecommun. Symp.*, vol. 2018-April, pp. 1–5, May 2018, doi: 10.1109/WTS.2018.8363930.

[225] D. V. Kute, B. Pradhan, N. Shukla, and A. Alamri, “Deep Learning and Explainable Artificial Intelligence Techniques Applied for Detecting Money Laundering-A Critical Review,” *IEEE Access*, vol. 9, pp. 82300–82317, 2021, doi: 10.1109/ACCESS.2021.3086230.

[226] V. Shankar and S. Parsana, “An overview and empirical comparison of natural language processing (NLP) models and an introduction to and empirical application of autoencoder models in marketing,” *J. Acad. Mark. Sci.*, vol. 50, no. 6, pp. 1324–1350, Nov. 2022, doi: 10.1007/S11747-022-00840-3/FIGURES/3.

VITA

Name Yi-Huan Chen

Key strengths

- Electromagnetism
- Metamaterials and Metasurfaces
- Numerical simulation
- Nanofabrication
- Signal and image processing
- Machine Learning and deep learning

Education

Ph.D., Electrical and Computer Engineering,
University of Illinois Chicago, Chicago, Illinois, United States, 2023

M.Sc., Institute of Applied Mechanics,
National Taiwan University, Taipei, Taiwan, 2012
Thesis Title: Investigation of District Magnetic Field in Meta-materials Through Effective Medium Theorem

B.Sc., Engineering Science and Ocean Engineering,
National Taiwan University, Taipei, Taiwan, 2010

Experience

Research Intern, Here Tech., Chicago, Illinois

Research Assistant, University of Illinois Chicago, Chicago, Illinois

Teaching Assistant, University of Illinois Chicago, Chicago, Illinois

Research Assistant, Academia Sinica, Taipei, Taiwan

Radar Operator, Coast Guard Administration, Taipei, Taiwan

Publications

- L. Zhu, T. Ha, **Y. H. Chen**, H. Huang, and P. Y. Chen, *"A Passive Smart Face Mask for Wireless Cough Monitoring: A Harmonic Detection Scheme with Clutter Rejection,"* IEEE Trans Biomed Circuits Syst., vol. 16, no. 1, pp. 129-137, Feb 2022, doi: 10.1109/TBCAS.2022.3148725.

- **Y. H. Chen**, T. Ha, D. Errircolo, and P. Y. Chen, *"Restoration of Antenna Radiation Pattern Using Conditional Generative Adversarial Network,"* 2022 IEEE International Symposium on

VITA (Continued)

Publications (Continued)

Antennas and Propagation and USNC-URSI Radio Science Meeting (AP-S/URSI), Denver, CO, USA, 2022, pp. 481-482, doi: 10.1109/APSUSNCURSI47032.2022.9887123.

- J. Y. Lee, **Y. H. Chen**, and P. Y. Chen, *"Degeneracy of Light Scattering Absorption by a Single Nanowire,"* Sci. Reports 2021 111, vol. 11, no. 1, pp. 1–8, Sep.2021, doi: 10.1038/s41598-021-98011-x.
- **Y. H. Chen** and A. H. Twing, et al., *"Atrial Fibrillation Risk Prediction from Electrocardiogram and Related Health Data with Deep Neural Network,"* ICASSP 2020, pp.1269-1273, doi: 10.1109/ICASSP40776.2020.9054403.
- K.C. Lee and **Y. H. Chen**, et al., *"Plasmonic Gold Nanorods Coverage Influence on Enhancement of the Photo-luminescence of Two-Dimensional Transition Metal Dichalcogenides Monolayer,"* Sci Rep 5, 16374, 2015, doi: https://doi.org/10.1038/srep16374.

Project

- Investigation of Frequency Band Width of Left-Handed Materials and Related Technology, Ministry of Science and Technology (MOST), Taiwan, 2009.

Membership

- IEEE Signal Processing Society member

Professional Activities

- Reviewer, Signal, Image, and Video Processing (SIVP)
- Reviewer, IEEE Transactions on Antennas and Propagation
- Reviewer, IEEE Sensors Journal